STARS

2014

In-situ synchrotron studies of turbine blade thermal barrier coatings under extreme environments

Kevin Knipe
University of Central Florida

In-Situ Synchrotron Studies of Turbine Blade Thermal Barrier Coatings under Extreme Environments

by

Kevin Knipe
B.S. The Ohio State University, 2007
M.S. University of Central Florida, 2009

A dissertation submitted in partial fulfillment of the requirements
for the degree of Doctor of Philosophy
in the Department of Mechanical and Aerospace Engineering
in the College of Engineering and Computer Science
at the University of Central Florida
Orlando, Florida

Summer Term
2014

Major Professor:
Seetha Raghavan

Abstract

Thermal Barrier Coatings have been used for decades to impose a thermal gradient between the hot combustion gases and the underlying superalloy substrate in engine turbine blades. Yttria Stabilized Zirconia (YSZ) is an industry standard high temperature ceramic for turbine applications. The protective coating is adhered to the substrate using a nickel based alloy bond coat. Through exposure to high temperature, a Thermally Grown Oxide (TGO) layer develops at the bond coat-YSZ interface. Large residual stresses develop in these layers due to thermal expansion mismatch that occurs during cool down from high temperature spraying and cyclic operating conditions. Despite their standard use, much is to be determined as to how these residual stresses are linked to the various failure modes. This study developed techniques to monitor the strain and stress in these internal layers during thermal gradient and mechanical conditions representing operating conditions. The thermal gradient is applied across the coating thickness of the tubular samples from infrared heating of the outer coating and forced air internal cooling of the substrate. While thermal and mechanical loading conditions are applied, 2-dimensional diffraction measurements are taken using the high-energy Synchrotron X-Rays and analyzed to provide high-resolution depth-resolved strain. This study will include fatigue comparisons through use of samples, which are both as-coated as well as aged to various stages in a TBC lifespan. Studies reveal that variations in thermal gradients and mechanical loads create corresponding trends in depth resolved strains with the largest effects displayed at or near the bond coat/TBC interface. Single cycles as well as experiments targeting thermal gradient and mechanical effects were conducted to

capture these trends. Inelastic behavior such as creep was observed and quantified for the different layers at high temperatures. From these studies more accurate lifespan predictions, material behaviors, and causes of failure modes can be determined. The work further develops measurement and analysis techniques for diffraction measurements in internal layers on a coated tubular sample which can be used by various industries to analyze similar geometries with different applications.

I would like to dedicate this work to my family who have supported me through every

step of my academic career

Acknowledgments

First, I would like to thank my advisor, Dr. Seetha Raghavan. Over the years, she has provided the guidance and mentoring necessary for me to complete this work. She strives to create opportunities for her students with her main goal being the success and growth of her students. She has not only served as my academic advisor but has mentored me in ways which will translate to many aspects of my future.

I express my sincere gratitude to Dr. Bartsch from the German Aerospace Center for contributing her vast knowledge and experience with Thermal Barrier Coatings. She showed much hospitality in allowing me to join her group and learn from her for a summer in Germany.

I would also like to thank Dr. Almer and Dr. Okasinski, along with their colleagues, from the 1-ID beamline at Argonne National Laboratory. Without them contributing to the x-ray diffraction experimentation and teaching me the analysis, the success of this work would not be possible.

I would like to thank everyone who contributed to acquiring the data at Argonne. Janine Wischek knowledge of fatigue experimentation was very valuable in setting up and running this portion of the experiment. Albert Manero, Carla Meid, Stephen Sofronsky, Claudine Lacdao, Matt Smith, as well as Janine all worked through the long hours, around the clock, to help take the measurements during the allotted time at Argonne.

Lastly, and most importantly, I would like to thank my parents. They have supported me in every way throughout my long and trying academic career. I was only able to

accomplish what I have because of their support and life lessons which they have provided me.

TABLE OF CONTENTS

ix

LIST OF FIGURES

LIST OF TABLES

CHAPTER 1
INTRODUCTION

1.1   Thermal Barrier Coatings

Thermal barrier coatings (TBC) [54] have have provided game changing technology in the aerospace and power generation industries for application on high temperature components of turbines since the 1950s, and became widely used in the 1980s after the development of what is now an industry standard with Yttria Stabilized Zirconia (YSZ) [80]. Over the years, increases in both power generation and propulsive efficiency have been largely linked to the development of high temperature blade materials such as nickel based superalloys and durable ceramics. The development of high temperature superalloys with enhanced strength at high temperature over conventional alloys has steadily improved engine capability. This is especially important for components such as high pressure turbine blades and vanes which are some of the most loaded components in a turbine engine. Significant contributions towards advances in achieving higher turbine inlet temperatures have come from TBCs, pushing the operating temperatures well above the limits of the metallic substrates they protect [69, 50, 11].

TBCs have qualities of both low thermal conductivity required to impose a large temperature gradient between the combustion gases and the underlying substrate, as well as the capability to withstand exposure to extreme temperatures. This facilitates both higher turbine inlet temperatures and a reduction in the load-bearing superalloy temperatures, and provides higher thermal efficiencies and reduced creep, oxidation and thermal fatigue effects in the substrate. TBCs are generally comprised of three layers.

These consist of a ceramic top coat which provides the low thermal conductivity, a metallic bond coat which adheres the top coat to the substrate as well as provides oxidation protection for the substrate, and the thermally grown oxide (TGO) which develops at the interface between the bond coat and the top coat due to oxidation of the bond coat.

Thermal barrier coatings were first used successfully in the 1970's for turbine application and entered use in the industry by the early 1980's [54]. However, they were first tested as an aerospace application in the 1940's and 1950's by the National Advisory Committee for Aeronautics (NACA) and the National Bureau of Standards (NBS) with the application of frit enamels to turbine parts [34, 29]. High temperature ceramic coatings then started to see testing applications in rocket technology. Flame sprayed zirconia-calcia coatings were applied to the thrust chambers of the X-15 manned rocket plane starting in 1960 [38, 19]. One of the findings from this work on the X-15 was that the material mismatch at the interface between the ceramic layer and the metallic substrate was one of the driving causes of failure and was subsequently addressed by grading the ceramic layer to provide better compatibility at the interface and adhesion to the substrate.

One of the most significant breakthroughs of TBCs happened in the 1970's when NASA developed the modern day standard of an yttria stabilized zirconia (YSZ) top coat attached to the substrate with a NiCrAlY bond coat [80]. This new coating design consisted of three main advantages [54]. The first was that it used Yttria (Y_2O_3) to stabilize the zirconia (Y_2O_3). Second, the NiCrAlY bond coat had very good oxidation resistant properties. And the last, the coating was a two layer system with no additional

layers needed for grading the thermal expansion mismatch. In its initial testing, 12 to 20% yttria was used to stabilize the YSZ. Further research determined that better performance could be achieved by lowering the Yttria content to 6 to 8% [81]. This is the same standard which is used for YSZ coatings today.

In the aerospace industry, electron beam physical vapor deposition (EB-PVD) is the common application process due to their longer life and their statistically superior reliability [9]. This process uses an electron beam to evaporate the oxide from an ingot and then deposit it onto a heated substrate [18]. One of the main advantages of the EB-PVD coating is the ability to control the application process and resulting micro-structure and composition. For the case of TBCs, this provides the large benefit of reduced surface roughness and the creation of a columnar structure [69]. The reduced surface roughness at the interface is especially important for the TGO by reducing undulations of a stressed brittle oxide [59]. The columnar structure in the YSZ is significant because it makes the ceramic layer very strain tolerant which is beneficial for these high temperature materials that are subjected to cycling. In order to exploit the benefits that TBCs provide, the mechanics that drive the failure of these coatings under the extreme environmental conditions that they operate in must be investigated.

1.2   Mechanics and Failure Mechanisms of Thermal Barrier Coatings

With the extreme temperature changes between coating application, shutdown periods and operating temperatures, these ceramic coatings can be susceptible to failure modes

such as spallation and delamination after cycling. This is due to the large residual stresses which are present in each of the layers of the coating. The large residual stresses present at the bond coat/TBC interface play a part in failure where the brittle TGO layer exists and is known to exhibit compressive residual stresses greater than 3-4 GPa [49, 68, 79, 82]. The residual stresses in the various layers are largely caused by the thermal expansion mismatch between the metallic and ceramic layers of the coating as well as TGO growth stresses created during high temperature exposure. These growth stresses are added compressive stress to the already highly stressed TGO which result from oxidation induced growth within the TGO thickness. It was first noted by R. Miller that the TGO was likely the largest factor in coating life determination [56]. Since then, many studies have shown that damage initiation for many failure modes occur at or near this bond coat/TGO/TBC interface [30, 95, 13, 22, 24, 71, 14, 49, 88, 82, 88, 33, 53, 97, 96, 41, 42]. This highlights the need for monitoring of strains in the TGO and the area surrounding the interface under conditions which represent operating conditions. Due to the difficulty in monitoring strain and stress during operating conditions, experiments largely consist of ex-situ investigations after cycling. Therefore, relating stress and causes for failure rely heavily on simulations which would need to be validated under the extreme environments that these materials operate in.

There are several resulting failure modes which have been found to be common in TBC coatings. One of the most significant failure mechanisms is associated with imperfections in the TGO. Due to visco-plastic deformation of the bond coat and the TGO being under large compressive in-plane stresses from thermal expansion misfit and TGO growth, the

oxide layer tends to want to displace out-of-plane [25, 78]. This is generally referred to as rumpling or ratcheting and increases throughout cycling [57, 37]. The undulations in the TGO created by this, which are still under high stress, develop very local tensile out-of-plane stresses which promote failure [43]. As the YSZ is not compliant enough to adhere to the local out-of-plane movement, cracking can then occur in the YSZ thickness near the irregularity [77]. This then results in a process of crack nucleation, propagation and coalescence [71, 87, 31, 98]. There have been many studies investigating the coalescence behavior after crack nucleation. Due to a wide array of factors, including geometry and thermo-mechanical loading, crack propagation can occur in various directions such as laterally through the bond coat, parallel to either the TGO-bond coat interface or the TGO-YSZ interface, and into the YSZ [91, 92, 10, 77, 78].

Final failure is often a result of buckling [25, 14, 77]. The YSZ has the stiffness to resist small scale buckling and therefore failure usually occurs through large scale buckling [25]. Surface preparation of the bond coat has been shown to be an effective tool in resisting this type of failure. It has been seen that after polishing the bond coat, failure was primarily caused by buckling, while the unpolished bond coat with small ridges created oxide imperfections where the fracture path traveled transversely through the TGO into the bond coat creating voids [92]. The crack driving forces for mechanisms such as this require knowledge of how the stresses evolve at elevated temperature and under mechanical loads. In-situ measurements of these could provide invaluable information which could be used to create TBC models for these investigations. This includes how

the stresses change through the thickness as well as inelastic behavior such as creep or plasticity which exists due to the high temperatures.

There are also several modes of failure which are associated with chemical processes. One of which is the creation of spinels due to either the Al depletion in the bond coat or the Ni diffusion through the TGO. Studies have found spinel formation due to this factor which has led to degradation [82, 74, 77]. This creates a failure zone corresponding to the spinel location either at the bond coat-TGO interface or the TGO-YSZ interface. Sintering is another common form of failure which causes increases in the thermal conductivity in the YSZ, increasing the temperature of the TGO and bond coat as well as increasing the total elastic energy in the YSZ, further promoting cracking [82]. These forms of failure among other associated with the chemical process have a strong dependence on the thermal loading. This suggests that testing under thermal gradient conditions which are experienced in turbine engines is a very important factor when conducting TBC studies.

There are many mechanisms which contribute to the various failure modes. Some of these include but are not limited to TGO growth, interfacial roughness [4], creep in the system, complex loading [59], and thermal expansion mismatch of each layer of the TBC system [4, 65]. Creep has a large effect on the durability of the coatings. This is the process of a material undergoing transient deformation under constant stress. The significance of creep in regard to system failure is usually associated with the bond coat and TGO. It has been shown that creep has a large effect on the stress distribution in TBCs [2]. The importance of creep in the TGO is that the oxide's resistance to rumpling and buckling is largely dependent upon it as the incentive for outward displacement due

to compressive stress is permitted by relaxation in the TGO. Creep properties in the TGO have shown varying results in literature as well as a large dependence on grain size [26, 66]. It has been shown through simulations that the TGO can exhibit significant stress relaxation at 1100 ℃ with grain sizes as low as 1 μm [70]. Creep in the bond coat is also considered to be a large factor in the rumpling of TGOs [5]. It has also been suggested through simulations that creep strongly affects cooling stresses and that fast creep in the bond coat, as well as the YSZ, result in lower stresses in the YSZ [4]. A study which tested three different NiCrAlY alloys between 800 and 1000 ℃, found that they relaxed very rapidly above 900 ℃ and showed significant dependence on the alloy composition [12]. Experiments have also shown that when a bond coat does not display a creep response, delamination at the TGO-bond coat interface occurs and causes buckling instability [78, 92]. It is extremely critical for simulations attempting to understand the causes of failure to accurately represent the extent of creep in these layers.

With the role that the compressive stress in the TGO plays in failure, understanding the extent that creep is experienced in both the bond coat and the TGO is vital to predicting failure. Due to limited methods, monitoring the creep strain in a YSZ/bond coat system applied to a substrate is primarily limited to simulations. These rely on creep laws which are generally derived from testing of stand-alone materials [60]. Thus far, experimental methods have limited the ability to measure creep in the TGO and bond coat layers in a TBC system which contains the ceramic coating and substrate and generally consist of stand-alone materials. Synchrotron measurements have shown promise as a capable method in experiments on bond coat specimens [94]. Measurements, which

will be shown here, provide a means to determine the extent at which loading conditions cause creep during cycling as well as to capturing the creep response quantitatively. This will be displayed for fully functional TBC coatings consisting of the full layers with no material removal.

TGO growth is another large contributing factor for cause of failure. First and foremost, TGO growth contributes to the in-plane stresses which are critical to failure. The out-of-plane stresses become larger during cycling through TGO growth as in-plane TGO stress increases [25, 16]. It has also been seen that the TGO will grow to a critical thickness and then spall off [67]. Growth can also contribute to stress concentration factors due to heterogeneous growth composition or phase transformations. During initial oxidation, the alumina that forms can be of the θ-Al_2O_3 phase before transforming to α-Al_2O_3 [39, 45]. This transformation can retain its original morphology and therefore create stress concentrations in the TGO. There have been a limited number of studies which have used synchrotron x-rays to monitor TGO growth of stand-alone bond coats [94]. However, these studies do not provide the information to fully understand the evolution during oxidation or thermal cycling and still leave a large need for in-situ studies [17].

To obtain the full picture of the stress/strain behavior, knowledge of immediate short term temperature and mechanical load variation response as well as long term changes must be determined. While the strain and material properties of the as-coated specimens provide valuable insight into the links between loading conditions and failure mechanisms, it is essential to study these strain effects at various stages of a coating lifetime. Along with the evolving stresses from TGO growth and rumpling, the phase composition and

microstructure of each layer is known to change significantly over the life of a TBC. These effects change the internal strains and how they respond to various loading conditions. Therefore, high temperature stresses at different stages of a TBC are required to understand how failure mechanisms can propagate.

In order to understand what dictates switching between various failure modes, it needs to be understood how stresses leading to damage are affected by variations in operational conditions. The stress distribution through the thickness of TBCs is largely reliant upon the thermal and mechanical load distribution. The bond coat, which is largely susceptible to creep, experiences temperature and stresses that are dependent upon these conditions. Further, the applied stress and temperature at the TGO location are two key factors in the incentive of the oxide to displace outward through rumpling or buckling. The temperature of the TGO, which is dependent upon the thermal gradient, affects the growth stress as well as the creep response. In combination with this, the in-plane applied mechanical load due to bending and centrifugal forces also affects both the rumpling inducing compressive stress. Therefore, much effort has been placed on studying temperature gradient and mechanical load effects.

In addition to thermal gradients, another necessary factor for real life conditions is mechanical loading. With the importance of creep on the ratcheting effect, mechanical loads which result from turbine centrifugal forces also are an essential inclusion. Experiments have shown that increased mechanical loads shift failure modes from delamination of the YSZ to failure in the bond coat [91]. Therefore, it is important for TBC testing methods to have both thermal gradients and mechanical loads simultaneously.

9

Due to the complexity and variation of TBCs under operating conditions, a full understanding of damage progression and failure prediction relies greatly on modeling techniques, such as finite element analysis to simulate crack promoting stresses. However, these models require validation from measurements of depth-resolved stresses and strains under high temperature conditions to accurately be used to predict failure. The different components of TBCs have microstructure and materials properties which vary largely through thickness and with temperature and cycling. Therefore, TBC models often must use over simplifications. For instance, YSZ layers in TBC coatings contain a complex structure which is inhomogeneous and anelastic [47]. Therefore, measurements of the real-life stress/strain behavior under high temperature conditions are required to validate modeling attempts at high temperature conditions. It is also important monitor the stress/strain behavior under dynamic loading. Investigations into the relationship between failure and thermo-mechanical loading conditions has shown that failure often occurs during cool down [55]. It has also been shown that variations in cool down rates are an important factor in failure [26]. Having measurements of the strain distribution during cool down would give insight into these mechanics as well as validate models attempting to do so.

The ability of a TBC to last an extended lifetime is dictated by its resistance to crack nucleation and propagation along with the complex stress distribution which exists throughout the multi-layer coatings. Due to variation in operating conditions and stress and thermal distribution throughout the turbine blade geometry, a large variety of failure mechanisms are seen in TBCs. While, the resistance to crack nucleation and

propagation is determined by a number of factors such as phase transformation in the YSZ, composition of the bond coat at the YSZ interface, composition of the oxide formation on the bond coat, and sintering of the YSZ, the focus highlighted here will be on the thermal and mechanical loading and their effect on stress/strain behavior which can drive damage nucleation and propagation. While there has been a substantial and successful effort into understanding common failure mechanism under different operating conditions, much is still needed in the ability predict failure of operational coatings [17]. Further understanding of the complex mechanics related with these multi-layered coatings is required to link design criteria and operating conditions with common failure mechanisms. To accomplish this, the relationship between different thermal and mechanical loads and the resulting internal stress/strain response needs to be determined. Due to the differences in application goals for performance criteria, the designed TBCs are required to withstand a variety of different operating conditions. Depending on the design goals, coatings must be designed where trade-offs are seen between reduced air cooling, higher operating temperatures or longer component life. Therefore, the applications for these coatings can create very different stress distributions, which in effect trigger different failure mechanisms. Design for optimization in different applications requires a link between the different design variables and their resulting high temperature stress history in each of the layers. This must be done before the relationship between design and various well known failure modes can be fully understood.

1.3 Motivation

Extensive research to understand the complexities of TBC failure, along with the motivation of modern day engine applications to further push the operating limits and reliance on the coatings, has led to efforts in developing more realistic testing techniques to better understand how the materials behave under various conditions. There are two areas associated with achieving relationships between loading conditions and stress/strain which will help move this research area forward. First, loading conditions that are representative of operational environments must be applied to the coatings. This includes subjecting the coating to a temperature drop across the thickness while simultaneously applying a mechanical load. Second, high-resolution in-situ measurements, tracking quantitative mechanical behavior must be taken under aforementioned conditions.

1.3.1 Recreating the Operational Environment

As the oxidation life of a coating is exponentially dependent on the YSZ-bond coat interface temperature [32], the thermal distribution is critical to failure. Since the primary function of these coatings are to create a temperature difference between the blade substrate and the hot combustion gases, thermal gradients are a very necessary inclusion for experimental testing. The importance of thermal gradients has been shown in various studies as alternative failure modes from that of isothermal tests have been seen. Experiments with thermal gradient fatiguing of flat button samples have shown that under certain cooling rates of the YSZ, surface cracks known as mud-cracks can develop sug-

gesting tensile stresses on the surface [48]. In the presence of sufficient thermal gradients, it has also been suggested through simulation that failure modes such as crack initiation and propagation can develop in the TBC parallel to the interface [40, 99].

Efforts to understand thermal gradient effects have led to various methods for subjecting this temperature drop across the coating. Induction heated graphite susceptors have been used to heat the YSZ while the substrate was cooled by a cooling block to create a thermal gradient for testing the effects on sintering [90]. Flame rig heating has been shown to be an effective method of inducing a temperature drop across the coating. With this method, the YSZ top coat of flat wafer specimens is heated by flame while the back side substrate surface is air cooled [21, 48, 62]. NASA Glenn Research Center developed another option of using CO_2 lasers to induce the heat flux to the TBC surface opposite the air cooled substrate on flat specimens [32, 100].

While methods such as flame heating and CO_2 lasers, have proved to be very effective in implementing surface conditions and temperature drops across the coating representative of engine conditions, it can be difficult to implement mechanical loading to the thermal tests. Recent methods are being developed to subject specimens to thermal gradient mechanical fatigue (TGMF) loading. One such method which has been developed used a heating susceptor to heat the coated side of the flat sample while using compressed air on the backside of flat specimens under mechanical loads [44]. Here, an extensiometer was used to measure the substrate strain throughout cycling to study creep effects. Damage was monitored after cycling and it was found that multiple fragmentation occurred where cracks of small spacing propagated from the YSZ layer into the bond coat, and

13

created voids beneath the TGO layer [44]. Another method which has been found to be very effective for applying thermal gradients across the ceramic coating has been seen with the use of infrared lamps and internal cooling of tubular samples [1, 7]. The use of tubular specimens with external heating allows for easy control of thermal gradient with coolant flowrate controllers. Another advantage of tubular specimens over flat specimens is the symmetric loading which does not include small bending stresses associated with sample asymmetry. This type of setup has been used with tubular sample geometries in ex-situ studies to monitor damage effects after TGMF loading where it was shown that the development of cracks beneath the top coat can contributing to the spallation process [6].

There are also obstacles associated with monitoring of the temperature distribution. Optical pyrometers are an option but pose difficulties in dealing with emitted radiation from the sample surface along with the ability of the temperature measurement to reach well below the surface [23]. One method to overcome this is to develop long-wavelength pyrometers which operates at wavelengths higher than TBC surface radiation (greater than 10 μm) [51]. Doping of the YSZ with materials which have temperature dependent luminescence lifetime decay has also been shown as a non-contact option to measure the temperature at the interface for thermal gradients [32, 27]. This however, requires changing the composition of the YSZ which is being studied. Additional work has been done to study the effects of axial, radial and circumferential thermal gradients [52]. The difficulty associated with maintaining a thermal gradient in cylindrical samples that

14

effectively simulates the operational conditions has been studied for TGMF testing using controlled coolant flow [7].

1.3.2 *In-Situ* Depth-Resolved X-Ray Diffraction

While there needs to be a deep understanding of failure mechanisms, further progress depends critically on the development of in-situ monitoring in the different layers under TGMF conditions [93]. Efforts to develop loading conditions which are more representative of operational environments, such as thermal gradient and mechanical loads, have increased in recent years. However, these efforts have generally been ex-situ investigations of failure propagation after cycling. Significant strides in understanding the causes of different failure modes can be made by the acquisition of high temperature in-situ data in the multiple layers through novel measurement techniques. In conventional testing, information such as micro-structural properties and stress/strain distribution are obtained in an ex-situ approach between cycles or at various stages of the life span. The material properties and strain distribution at high temperature are largely unknown in terms of physical measurements.

Various optical methods have shown some promise as a method for in-situ stress/strain measurements. Photoluminescence piezospectroscopy (PLPS) is a non-destructive optical method which can be used to monitor the TGO stress in EB-PVD coatings. In this method, a laser beam can penetrate through the YSZ layer and excite Cr^{3+} ions in the TGO to measure the hydrostatic stress [15]. PLPS has been used to study thermal cycling

and its effects on TGO rumpling. It was shown destructively and with PLPS that as temperature increased, the rumpling rate increased while the TGO stress and the cyclic life decreased. While these optical methods have their uses, there are limitations in terms of penetration depth. PLPS and Raman Spectroscopy require sensitive emission peaks to provide measurements of mechanical behavior and has been limited to monitoring of the TGO and some YSZ features. Collection time for these methods is another limitation for monitoring in-situ stresses. With the dynamic response to loading curves, mapping a cross-section can require a full scan be done in under a minute. Therefore, these methods are not a viable solution to measuring depth resolved in-situ stress/strains through each of the layers. With failure modes often occurring near the highly stressed region of the bond coat/TGO/YSZ interfaces, the ability to monitor the depth resolved stress/strain gradient at and near this location during in-situ loading would provide invaluable information in the effort to understanding the link between loading conditions and the triggers of different failure modes.

X-ray diffraction (XRD) has proved to be an extremely powerful tool for in-situ measurements. With measurement of diffraction angles as a function of lattice spacing, this is an effective measurement for residual strain, phase composition, texturing, and lattice parameters. Another benefit of XRD is that it provides valuable information on directional strains, where optical methods such spectroscopy provide hydrostatic surface stress information. With the importance of the different strain components in TBCs, directional strain measurements can provide a wealth of information. However, conventional laboratory XRD systems are generally limited to penetration depths of several

micrometers through a material such as zirconia. With the high-energies provided by a synchrotron, measurements can penetrate multiple millimeters of heavy materials. In the higher energy range, between 50 and 100 keV, through transmission measurements can be conducted at a very fast rate.

With the development of new technology, high resolution testing with synchrotron XRD has become an in-situ measurement technique with enormous potentially for significant findings. High energy x-rays have been used to characterize strain in various ex-situ studies of cycled TBC samples providing important validation of quantitative strains from theoretical models [86]. Synchrotron XRD has also been used to take in-situ depth-resolved measurements in the bond coat of samples under isothermal loading for use of determining the out-of-plane component which contributes to spallation [83]. Similar methods were later used to measure the stresses in the YSZ during isothermal loading [84]. More unique in-situ studies, on phase changes during oxide formation, have revealed new information on significant tensile stresses in the oxide accompanying the associated volume reduction [94, 64]. More recently, synchrotron XRD strain measurements on TBCs under thermal-mechanical loading conditions have shown the dependence on applied axial loads of the strain transition into the tensile region at high temperature in the TGO of as-coated specimens [20].

1.4 Objectives

The vast complexity of the interactions between each of the layers and how they evolve under operating conditions and over time have thus far made it impossible to derive lifetime models which can effectively be implemented in industry. With the increased demands and reliance on TBCs for future applications in turbine engines, in-situ monitoring of these layers while subjected to environments as close as possible to operating conditions is required [93, 17]. Up until now, internal mapping of stress and strain under thermal gradient and mechanical loading has yet to be accomplished. The work presented here will provide innovative methods and results which address this issue. The main goal of this research is to acquire previously unseen data relating the stress/strain dependence to in-situ loading conditions. In addition, the research will investigate the evolution of stress/strain and material properties over a fatigued lifespan. This involves the need to develop experimental setups that consist of applying thermal gradient and mechanical loading conditions while maintaining access for in-situ XRD acquisition. Additionally, techniques must be developed for analyzing internal measurements under complex loading conditions of cylindrical samples. To meet these goals, the objectives are as follows:

1) The primary objective of this research is to obtain and study the relationships of the internal stress/strain dependence on thermal gradient and mechanical loading conditions in the various TBC layers. By developing the ability to monitor these strains at high temperature, insight into how the through depth strains evolve during in-cycle conditions will allow for the direct validation of coating models predicting this behavior under thermal operating environments. With the improvement of coating models for various

conditions, failure prediction can be significantly enhanced to achieve the maximum life of a TBC coating. Substantiating the link between in-situ measured strains under operational conditions and locations of different failure modes, will further the application field of TBCs. Strains within the depth of the layers are vital to the improvement of material models to predict the behavior that leads to failure and in turn improve the coating application design process. With failure modes often occurring near the highly stressed region of the bond coat/TGO/YSZ interface, the ability to monitor the depth resolved stress/strain gradient at and near this location during in-situ loading would provide invaluable information in the effort to understanding the link between loading conditions and the triggers of different failure modes. The initial testing of as-coated samples has successfully measured depth resolved strain measurements to display the relation of the strain gradient near the interface to the variation of both thermal gradient and mechanically applied loads.

Results from these studies for as-coated/early-cycled specimens are presented in Chapter 4. To fully achieve the goal of developing these relationships with the intention on furthering understanding the bigger picture of TBC lifespans, fatigue effects are also critical. To account for fatigue effects samples are pre-aged to various stages of a TBC lifespan. Similar testing was conducted after aging and results are compared to early-cycled specimens. This will provide trends for how in-cycle behavior as well as sensitivity to gradients and mechanical loads evolve over a lifespan. In addition, creep tests were conducted for aged specimens to provide creep models of functioning TBC coatings. Results for aged specimens are presented in Chapter 5.

2) The second objective is to replicate engine environments while acquiring in-situ XRD measurements. This study presented here combines both the expertise in developing realistic testing conditions and in obtaining in-situ synchrotron measurements to achieve such an advanced testing capability for TBCs. The primary experimental challenges lie in creating a controlled thermal gradient while maintain access to XRD measurements, achieving high-resolution through-transmission XRD measurements on the hollow cylindrical sample geometry and data processing for a tri-axial state of stress. The added complexity of the multi-layered material system and the thermal gradient instrumentation with the furnace surrounding the sample is addressed in this work. Here we show the ability to monitor the various internal layers in the coatings while applying a thermal gradient, through the development of novel XRD measurement techniques in both through thickness and grazing of the sample. This will show the capability to acquire measurements of distinguishable phases through the depth of each layer at multiple locations on the geometry.

The approach of controlling the thermal gradients to achieve a high heat flux is presented through methods in focused radiation heating on the external surface in addition to cooling the substrate internally. Temperature monitoring of the system is used to establish techniques to control variable thermal gradients across the coating thickness. The outcomes unveil an advanced in-situ test method for high temperature coatings research with extensive capabilities in monitoring time-correlated response of these materials under harsh and extreme environments. The potential for capturing otherwise unknown material behavior under operational environments is a much-needed contribu-

tion towards significant progress in testing of these materials to achieve the next steps in durability enhancement. Methods for developing thermo-mechanical loading and control will be discussed in Chapter 2.

XRD data has been successfully taken for phases in each layer at multiple locations on the sample which can be used account for all three components of the strain tensor. 2D strain measurements have been obtained using the grazing method tangential to the coating layers throughout loading conditions. The additional test measurements of transmission directly through the center of the sample providing axial and circumferential (both in-plane) strains have suggested that the tri-axial state of stress in the bond coat for cylindrical coatings contains a hydrostatic component not obtainable under current 2D deviatoric strain measurement techniques. This states that the equi-biaxial in-plane strain assumptions usually applied to thin coatings is not applicable to these types of cylindrical coating geometries. This work has developed techniques for exploiting the anisotropy of the cubic bond coat phases for 3-D stress calculations. It is suggested that by equating the stress calculated from multiple lattice planes of the micro-strains in the anisotropic grains, this full strain tensor can be obtained. Furthermore, comparison of the cubic lattice constant for multiple plane can be used to directly measure the deviatoric component without the need for assumptions of unknown strain components. Techniques for acquiring XRD measurements are discussed in Chapter 3.

Through completion of these objectives, in-situ results relating depth resolved strains under variable thermal gradient and mechanical loads will be presented for the first time. These results will provide behavioral relationships to better understand the extremely

complex cause and effect scenarios which link design variables to ultimate failure. With the necessary role which material and system models play in the attempt to bridge this gap between design variables and failure, results such as these will play a vital role in model creation and validation. The experimental techniques developed here, unveil an advanced in-situ test method for high temperature coatings research with extensive capabilities in monitoring time-correlated response of materials under harsh and extreme environments. With development of emerging materials for turbine applications, this gap in understanding between design and failure becomes even larger and the need for such testing becomes much more important. These methods will prove to be valuable not only for currently established TBCs but also for new advanced turbine coatings and the many other high temperature coating applications.

CHAPTER 2
DEVELOPMENT OF THERMAL GRADIENT AND MECHANICAL

LOADING

Through collaboration with the German Aerospace Center (DLR) in Cologne, Germany, preparation was undertaken to develop a setup which included design of a sample/thermal loading environment which would best represent the conditions of a coating under operation while maintaining access to synchrotron XRD measurements. Working with DLR in Germany, the expertise of the research team at UCF on synchrotron XRD measurements [20] was combined with the expertise of DLR on sample preparation and thermal gradient and mechanical fatigue experimentation [7]. The experience obtained from working with DLR and studying the heating application and thermal monitoring and control was necessary to the development of a test rig which could be implemented in a synchrotron beam line.

TBCs operate in an extremely harsh environment. They are exposed to high temperature gases exceeding 1100 ℃, steep temperature gradients, fast temperature transients and additional mechanical stresses due to centrifugal loads [93]. Recreating all of these conditions are an important part of producing stress profiles in coatings which represent real-world operation. Since each of these conditions have coupled effects on stress profiles contributing to damage, it is necessary to study TBCs under a combination of all load effects. However, creating such an environment in a laboratory setting presents several challenges. This becomes significantly more complex when the design criteria requires maintaining access for XRD measurements as well as ease of setup under limited access time in a user facility such as a synchrotron.

Figure 2.1: Tubular TGMF test specimen

To best apply uniform thermal gradients across a coating thickness, samples were designed with a tubular shape to allow internal cooling of the substrate and external heating of the coating. This also allows for a temperature gradient to be applied through the thickness of each layer with no influence from an exposed coating cross section seen in flat samples. This in-plane temperature consistency of cylindrical specimens is very beneficial to strain measurements as opposed to flat specimens which may present either heating of the exposed cross-section or an in-plane gradient near the edges hindering strain results. The dog-bone shaped sample shown in Figure 2.1 contained a cylindrical measurement length of roughly 50 mm. The hollow Inconel 100 sample had an inner diameter of 4 mm and an outer diameter of 8 mm. This geometry is considered similar to that of a leading edge of a turbine blade [8]. The EB-PVD TBC on the sample consisted of 7-8 wt% Yttria-Stabilized Zirconia (YSZ) ceramic topcoat with a thickness

24

of 211 +/- 4 μm and a NiCoCrAlY metallic bond coat with a thickness of 118 +/- 4 μm. The EV-PVD applied bond coat contained a wt% composition of 20Co, 21Cr, 12Al, 0.15Y, and a balance of Ni.
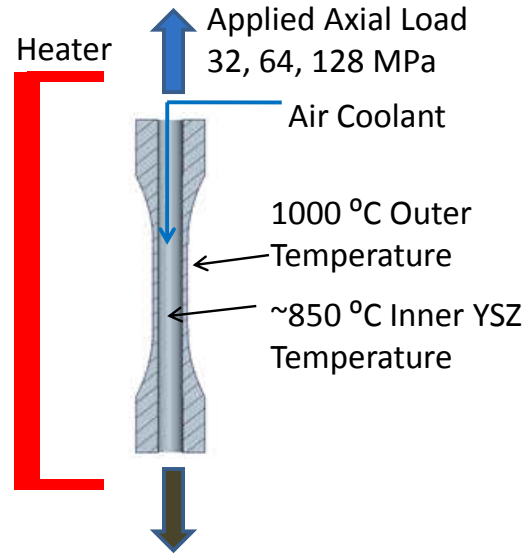
Figure 2.2: Loading of TBC coated tubular specimen

2.1 Specimen Loading

The goal for these experiments was to apply loads to a specimen as shown in Figure 2.2. Achieving this requires application of severe conditions to both the high and low temperature sides of the coating to reach the desired temperature drop across the coating as well as applying a large tensile load to the specimen under these extreme temperatures. The primary challenges associated with controlling the thermal gradient with a tubular sample are attaining the necessary thermal loading conditions for the desired gradient and accurately monitoring of the temperature conditions. The schematic for

the experimental setup is presented in Figure 2.3. Heating of a cylindrical surface allows the implementation of an enclosure heater, minimizing heat loss as well as, creating circumferentially consistent temperature values required for accurate representation of operating conditions.
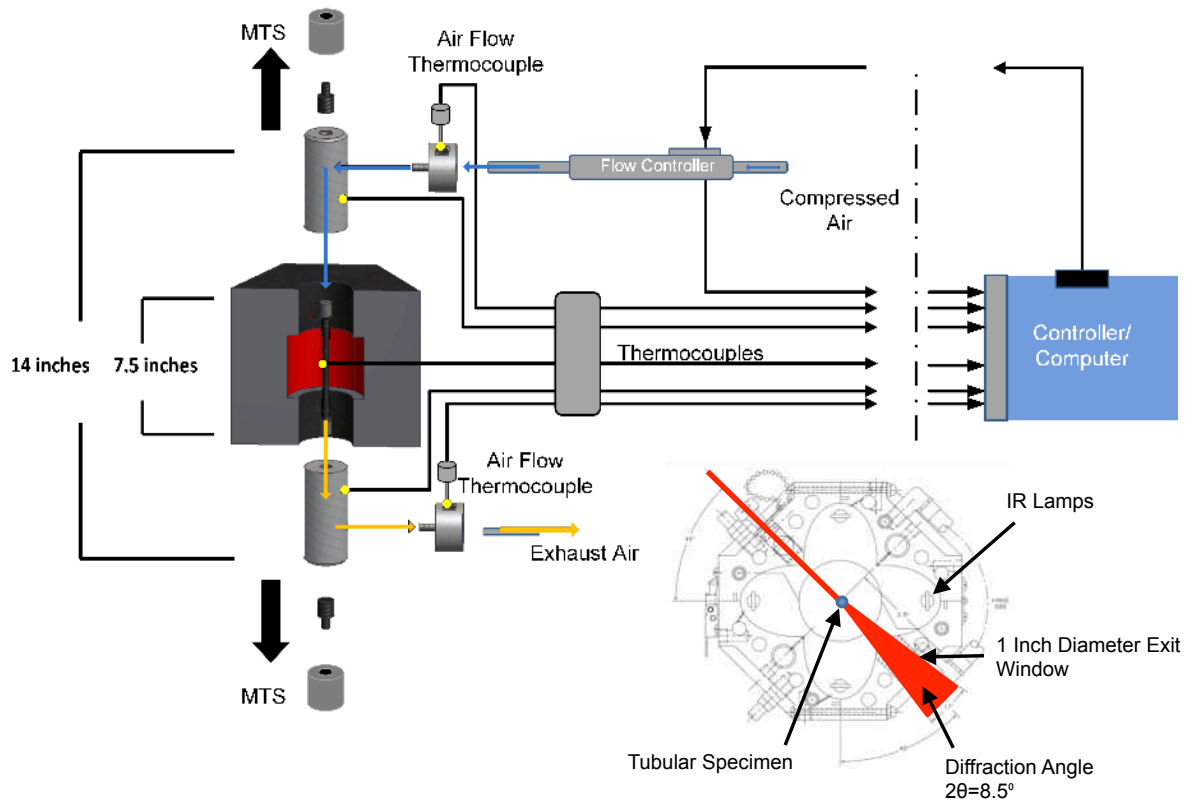
Figure 2.3: Thermal gradient and mechanical load apparatus schematic [75]

2.1.1 Heater

To provide conditions realistic of the environment found surrounding a turbine blade, an infrared radiation chamber heater was employed. This made use of 2000 Watt cylindrical Ushio halogen lamps with a heated length of 3 inches. The specimen was encircled by

four lamps, totalling 8000 Watts, in an arrangement shown by the heater top view in Figure 2.4. Radiation from each lamp was focused to a center line with elliptical mirrors to provide optimal flux for a cylindrical specimen. This provides sufficient heating to sustain 1000 °C and above surface temperatures on the sample while maintaining the energy draws from cooling required to achieve large thermal gradients. The heater housing was sufficiently water cooled while the bulbs were air cooled to increase their longevity. To maintain access for beam diffraction, circular inlet and exit windows were created through the center of the front and back heater walls. High energy synchrotron x-rays allow the ability to use relatively small exit windows due to the small Bragg angle. The 1 inch diameter exit window shown in Figure 2.3 provided a 2 diffraction angle of 8.5°.
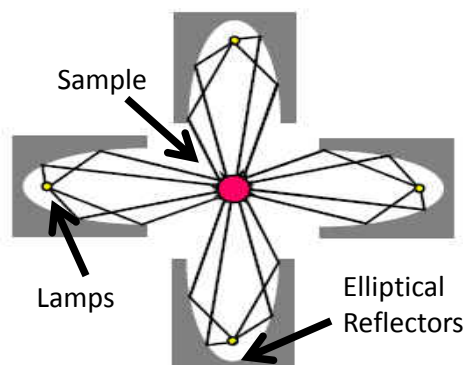
Figure 2.4: Heater top-view schematic

2.1.2 Thermal gradient

As illustrated in Figure 2.3, the thermal gradient was controlled using a flow controller which is capable of regulating the compressed air flow from 0 to 100 standard liters

per minute (SLPM). This air coolant was forced internally through the sample grips and through the inner channel of the sample. This provided forced air cooling of the inner substrate wall of the tubular sample as well as additional cooling of the grips. As shown in Figure 2.5, a 0.35 mm diameter S type thermocouple was created with an exposed junction which can be used in a hoop configuration pulled around the specimen, providing a quick thermally responsive feedback for heater control. Inlet and exhaust air temperature data was collected by using two inline type K thermocouples giving measurements of total energy gains of the flow between the ports on both grips. Surface temperature measurements of the grips were taken just outside the heater, opposite the coolant port, and these served as indicators of total system steady-state as well as changes in heat loss across the grip material. The energy gain of the coolant flow along with the energy change across the sample and grip thicknesses could be used with the addition of simulations to validate thermal gradient calculations.

Figure 2.5: Sample heating with surface thermocouple measurement

2.1.3 Mechanical Integration
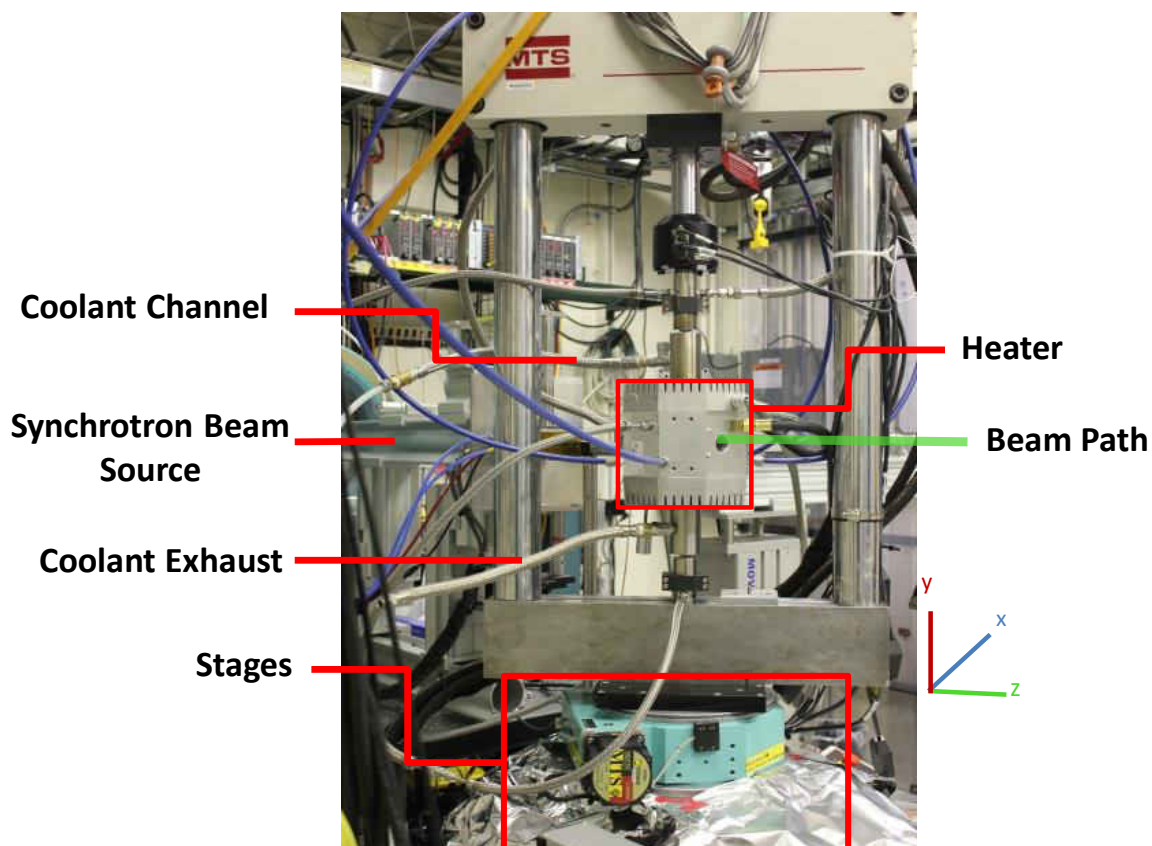
Figure 2.6: Experimental setup at Argonne National Laboratory

The heating system was integrated into a load frame setup at the 1-ID beamline at Argonne National Laboratory as shown in Figure 2.6. A servo-hydraulic MTS load frame located at the beamline was used to apply the tensile mechanical loads to the specimen. With MTS loads exceeding 5 kN and maximum sample temperatures reaching 1000 °C and above, Inconel 718 threaded grips were used to fasten the sample to the MTS under these extreme conditions. The heater and MTS load frame were mounted in a configuration to allow four degrees of freedom for relative movement between the

heater and sample. The heater was grounded and fixed to a location based on the stationary beam and heater exit window. The MTS load frame was mounted through stages providing three translational degrees of freedom and an axial rotation degree of freedom. To move the measurement location on the sample, the load frame along with the sample were translated laterally relative to the beam. These translational stages are accurate and repeatable to nearly 1 μm.

2.2   Thermal Results
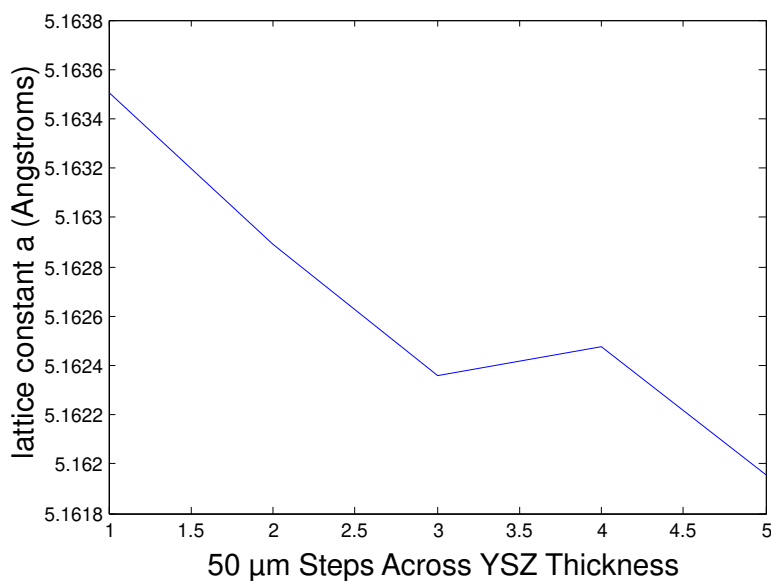
Figure 2.7: Measurement of YSZ lattice constant (a) over the thickness for thermal gradient estimation

With the use of XRD d-spacing measurements through the thickness of the YSZ layer during flowrate increases, the thermal across the YSZ can be estimated. By comparing

the d-spacing of the (200) and (002) planes, the tetragonal lattice parameters (a, c) of the YSZ can be measured. These parameters are then related to temperature to determine the temperature drop across the YSZ. This uses the thermal expansion coefficients measured in Chapter 3, along with the lattice spacing change across the thickness, to estimate this temperature drop. Figure 2.7 displays an example of this for a flowrate of 70 SLPM (70% of maximum). This displays a lattice change of 0.0015 Angstroms. Using the thermal expansion coefficient, the estimated temperature drop is 134 °C over the 240 μm thickness of the YSZ under 70% thermal gradient.
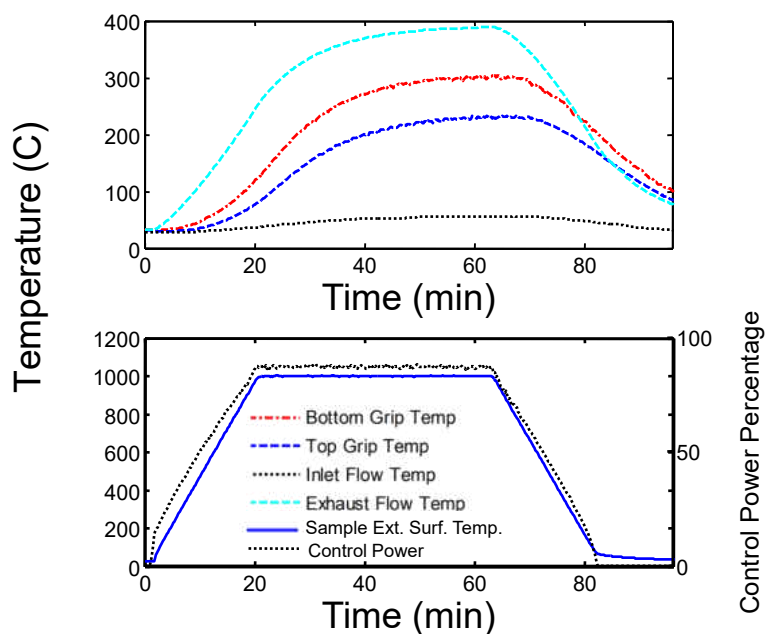
Figure 2.8: Thermal measurement for a cycle with internal cooling [75]

Figure 2.8 provides the temperature measurements of a thermal cycle. The sample surface was heated up at a rate of 50 °C per minute from ambient to 1000 °C and held at high temperature for 40 minutes after which it was ramped back down to ambient

31

temperature. The flow rate was held constant at 75 SLPM throughout the cycle. It is notable that there is a lag between the bottom (exhaust) grip temperature and the exhaust flow temperature. There is also a slight rise in inlet air temperature readings, as the housing around the probe has some heat conducted to it.
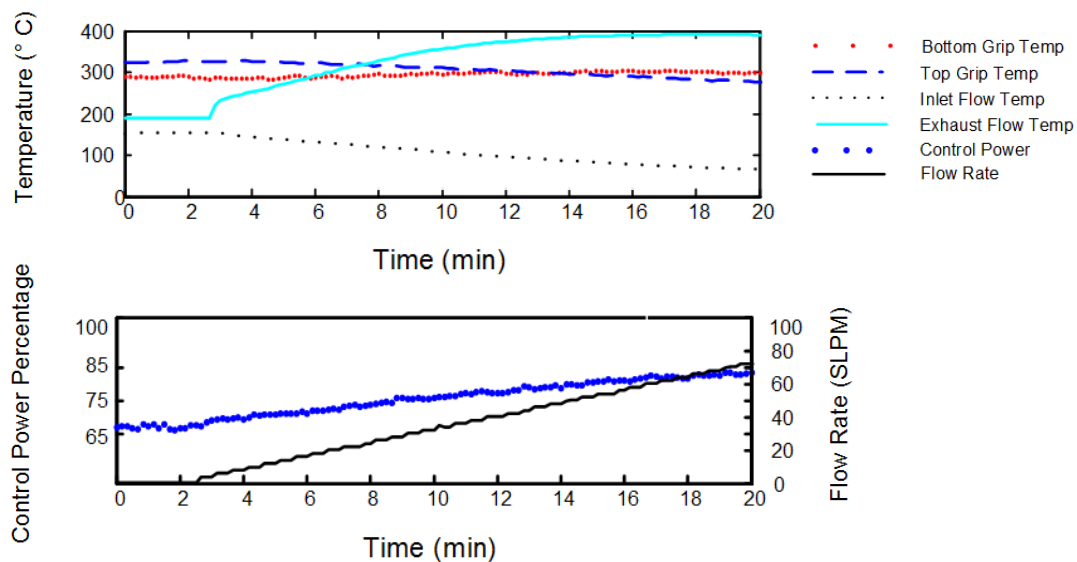
Figure 2.9: Thermal measurements for a linear increase in flow rate [75]

To test the temperature response to variation in flow-rate, a ramp increase in coolant flow rate was applied to the system at high temperature. The entire system was initially allowed time to reach steady-state with an external sample surface temperature of 1000 °C. The internal airflow was then increased linearly at a rate of 0.25 SLPM per minute from 0 to 75 SLPM. This rate was chosen in an attempt to mitigate transient behavior of the gradient across the midsection thickness of the coated specimen while minimizing the time for increased heat loss of the sample grips. The effects of this can be observed in Figure 2.9 where increases in the flow rate produce a smooth curve in the exit coolant temperature but near constant grip temperatures during the variation period. The exit

coolant temperature reaches a maximum of 395 ℃ at 60 SLPM with the inlet temperature taking longer to tend towards steady state. This reflects the ability of the inlet ambient air temperature to overcome the unwanted heating effect of the grip on this thermocouple. The surface grip temperatures show relatively small changes giving the desired limiting of the energy variations in the grip material.

2.3 Summary

Experiments have been successful in applying the desired thermal and mechanical conditions to a TBC specimen. The thermal loading setup was successful in applying these thermal gradients with a high temperature of 1000 ℃. These measurements display the ability to apply a large enough heat flux to maintain surface temperatures in the range of realistic operating conditions while sustaining large energy draws at the inner substrate. While applying coolant levels corresponding to the largest energy draws, surface temperatures were maintained at and above 1000 ℃, displaying sufficient heating at maximum thermal gradient. The temperature trends shown in these studies present, qualitatively, the ability to create large thermal gradients through the measured energy drawn from the system by the coolant temperature increase. Loading conditions from this innovative setup have been applied while maintaining the ability to measure in-situ XRD.
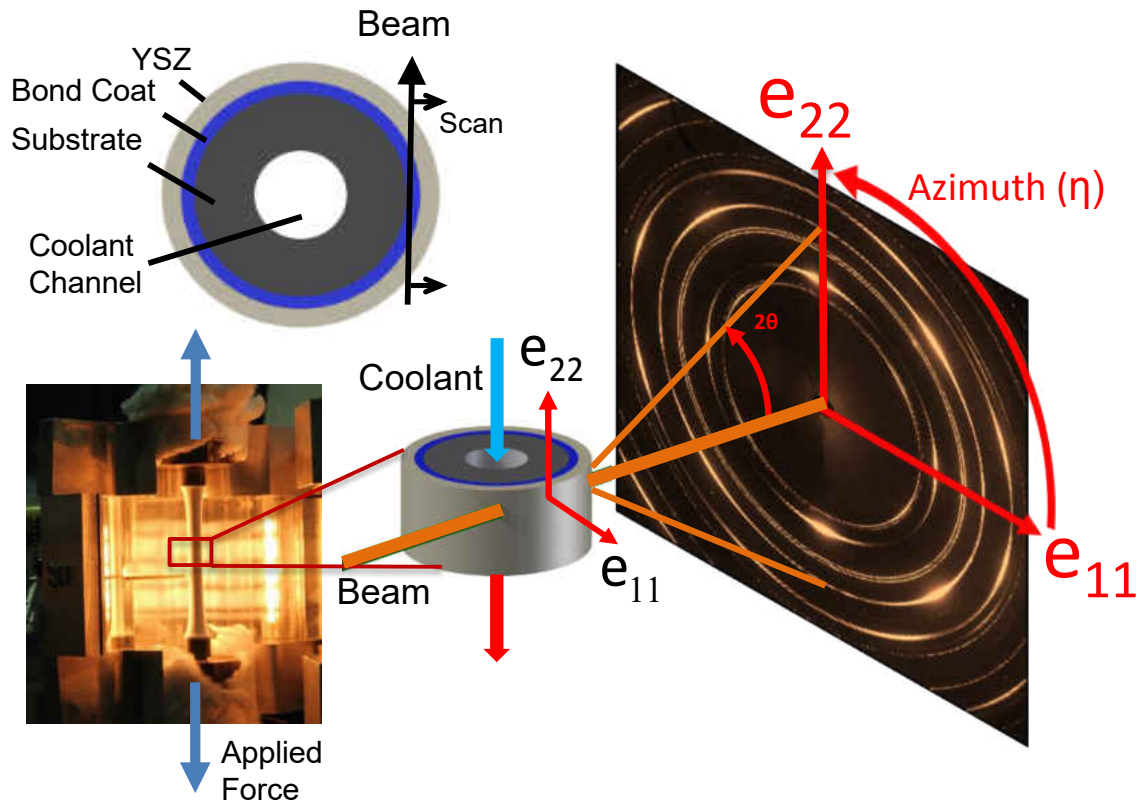
Figure 3.1: Synchrotron XRD measurement transmitting through the sample tangential to the layers yielding 2-D diffraction with radial (e_{11}) and axial (e_{22}) strains

All X-ray diffraction experiments were conducted at the Advanced Photon Source (APS) at Argonne National Laboratory in Chicago, Illinois. The thermal and mechanical loading, described in Chapter 2, was assembled and tested during the during the allowed beam time and was designed to allow access for the measurements described. With high-energy synchrotron x-rays and a 2D detector, high resolution through transmission

measurements were taken as shown in Figure 3.1. This required overcoming obstacles for both acquisition of internally depth resolved strain tensor measurements in cylindrical coatings as well as conducting in-situ measurements during thermal loading. Testing was done to achieve diffraction measurements at various locations on the cylindrical geometry. Stress and strain analysis techniques were created to acquire the tensors from the internal volumes of the specimen layers. Methods were also developed for taking spatially resolved measurements within a thermally expanding specimen.

3.1 X-Ray Diffraction

X-ray diffraction is the process of passing an x-ray beam through a crystalline structure for the purpose of measuring the inter-atomic distances of the crystalline material. This follows Bragg's law, which explains that when x-ray wavelengths are similar to that of the atomic spacing, reflections will occur at a specified angle, 2θ, to the incident ray and are related to the atomic spacing. Crystalline materials have a periodic atomic arrangement which can be defined by the stacking of different unit cells, where this unit cell describes the basic arrangement of the atoms. These unit cells are defined by lattice parameters consisting of three edge lengths (a, b, and c) and three axis angles (α, β, and γ). With the stacking of these periodic unit cells, the crystalline structure can be described by different three dimensional repeating planes with a particular spacing described as d. The orientation of these repeated planes are represented by Miller indices (hkl) which are normal vector relative to the unit cell coordinate axis. Bragg's law, shown

in Equation 3.1, relates the x-ray wavelength (λ) to the atomic plane spacing (d) through the diffraction angle (2θ), where n is an integer. Therefore, measuring the diffraction angle under constant x-ray energy from a monochromatic source can be used to directly measure lattice spacing. This works as a powerful tool for measuring residual strain and stress, grain orientation, grain size, material composition, and lattice constants. This is especially useful for residual strain and stress. When a stress is applied to a lattice structure, the resulting change in d-spacing creates the measurable variation in diffraction angle as shown in Figure 3.2. With a known stress free 2θ, residual lattice strains which result from processes such as cool-down during manufacturing can be determined.

$$n\lambda = 2d\sin(\theta) \tag{3.1}$$

Polycrystalline materials with varying grain orientation produce diffraction reflections at 360° about the beam axis creating what are known as Debye-Scherrer cones. The different lattice planes of various d-spacing create concentric circles when measured with an area detector. This effect is displayed in Figure 3.3. 2-D panel detectors have a great advantage over conventional point or 1-D detectors with the ability to measure the entire diffraction ring produced by this conical diffraction. Having measured the entire diffraction ring, information such as grain size and preferred grain orientation (texturing) can easily be determined. 2-D diffraction also allows measurements of many lattice planes simultaneously, providing relative intensity information which can be used for phase identification. For residual strain analysis, the radial displacement around a diffraction ring can be used to accurately fit a 2-D strain curve.

36
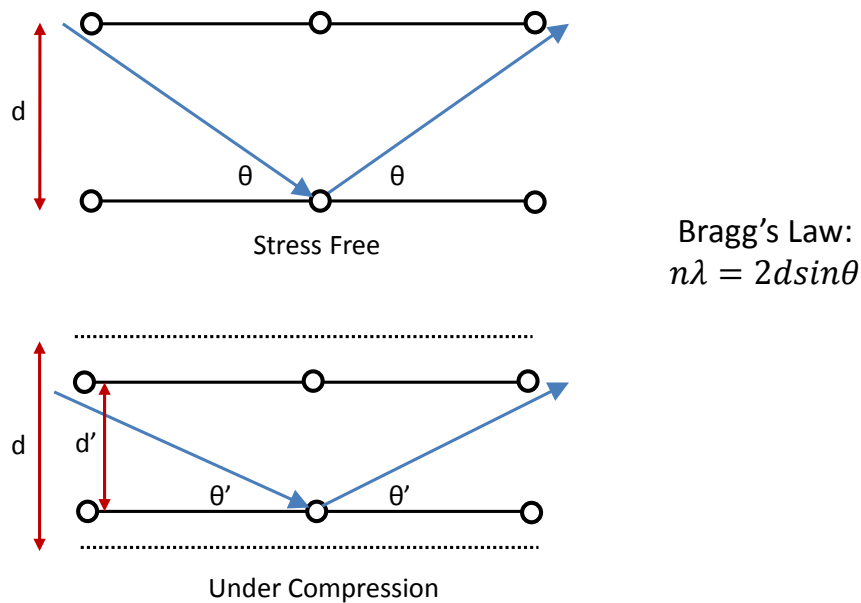
Figure 3.2: Lattice strain effect on diffraction angle

3.2   Advanced Photon Source

The APS is a Department of Energy funded synchrotron facility which provides the brightest x-rays in the western hemisphere. Synchrotrons are particle accelerators which can be used to produce very high-energy x-rays. A linear accelerator is used to accelerate the electrons to high-energy levels before they are injected into a storage ring. The storage ring at the APS, which is 1,104 meters in circumference, houses electrons which reach 7 GeV of energy. Around this storage ring are 40 straight section beamlines which contain experimental hutches that can be accessed by "users" for various types of energy related experiments. The experiments conducted here, were done at the 1-ID beamline. The 1-ID beamline is the first beamline on the storage ring after the injector and provides some of the highest brilliance x-rays at the APS with an operating range of 50-100 keV. A liquid

nitrogen cooled monochromator uses two symmetrically cut perfect Si(111) crystals in Laue geometry to tune the energy levels [73]. Immediately after the monochromator are saw-tooth silicon refractive lenses which are used to vertically focus the beam across the entire energy range [72].
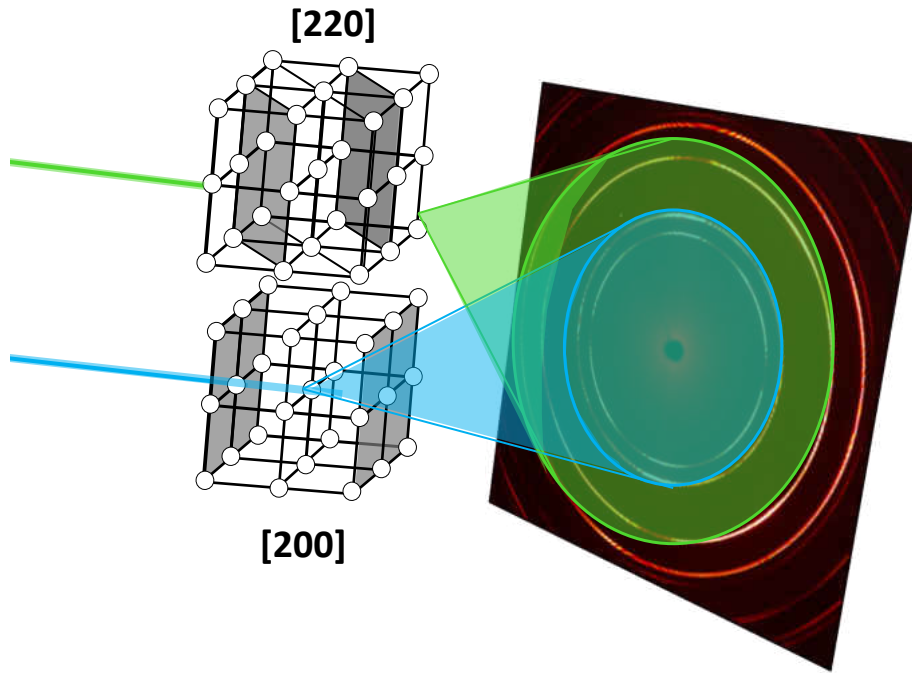
Figure 3.3: XRD measurements with a 2-D detector

High strain resolution measurements were taken using a General Electric Revolution 41-RT area detector. This is a 0.2 mm pixel size, 4100 x 4100 mm, flat square panel detector which can take measurements at 8 images per second. This detector has been proven to provide low background noise measurement and exceptional linearity between incident photon flux and detector response [46]. The spatial resolution, flatness (for minimal distortion), signal-to-noise ratio, and collection speed exhibited by the detec-

tor are critical for dynamic strain measurements. Sample to detector distances for the experiments varied between 1.4 and 1.5 meters.

3.3 Data Collection and Processing

For strain analysis, high precision measurements are required for sample to detector distance, beam center, and detector tilt. Error in any of the dimensions can lead to distortion of the image to be analyzed. A CeO_2 powder sample was used to provide strain free measurements for this calibration. Images were collected at 1 second exposure per frame with either 5 or 10 frames per measurement. To remove residual background measurements, dark files were collected with the beam shutters close before every experiment. Software provided by GE was used to sum the frames, correct bad pixels, and subtract the residual measurements. Throughout the thermal and mechanical loading experiments, the beam scanned through the layers with a window width and step size of 30 μms.

3.4 Material Phase Identification

For the as-coated specimen, the phases are identified in both the x-ray spectrum and raw data. For the identification shown, the beam penetrated directly through the bond coat, giving phases for both bond coat and YSZ due to the curvature of the sample. Displayed in Figure 3.4, is a raw data image highlighting the lattice planes of these phases. Here,

both the high texturing of the YSZ and the fine grained nature of the bond coat can be seen. The texturing of the YSZ due to the columnar structure of the EB-PVD application is quantified in a later section.
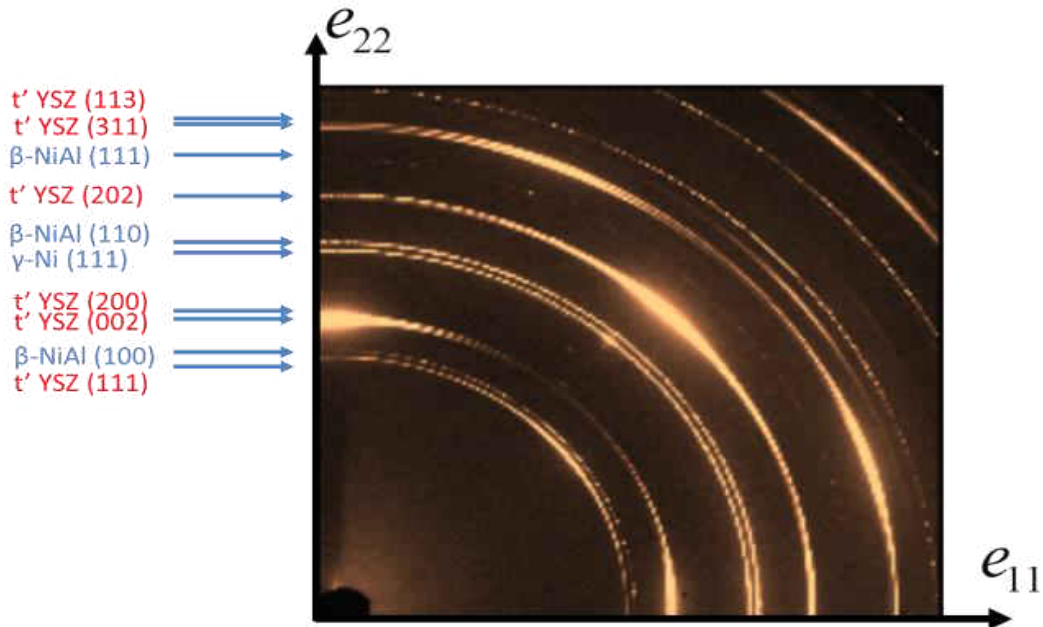
Figure 3.4: As-coated raw data phase identification

In the YSZ, the t′-YSZ is the most prominent phase measured. Two prominent phases are detected in the bond coat. These are the β-NiAl phase and a solid solution γ-Ni phase. For the as-coated specimen, it was required to scan farther into the bond coat to achieve enough volume of the TGO to detect even a minor presence of an XRD pattern. At this location near the bond coat substrate interface, a γ'-Ni_3Al phase was detected which displays an intermittent diffraction pattern representative of larger grain sizes. The largest distinguishable α-Al_2O_3 peak is the (116) peak, which coincides with the γ'-Ni_3Al (210) peak. The phases are also displayed in the x-ray spectrum in Figure 3.5. This

shows the diffraction intensity averaged around the entire ring circumference producing averaged intensity vs. 2θ.
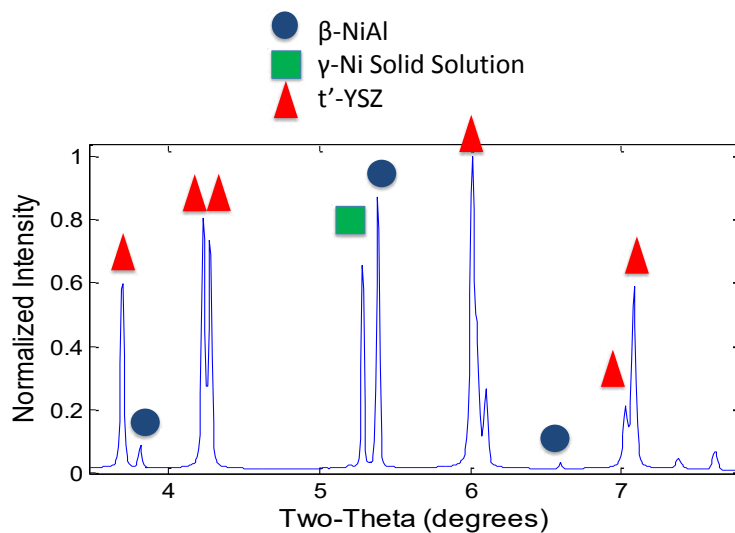
Figure 3.5: As-coated x-ray spectrum phase identification

Due to the minimal diffraction measured from the TGO in the as-coated specimens, specimens were aged to further develop the oxide layer. This provided a thick enough oxide layer to easily obtain diffraction measurements sufficient for strain analysis. Shown in Figure 3.6, is the radial transform of the raw data identifying the α-Al_2O_3 (116) peak at the bond coat/YSZ interface. This image displays the raw data transformed into an azimuth angle vs. radial position image. The strain displayed by the radial deviation can also be seen in this Figure and is discussed in a later section.
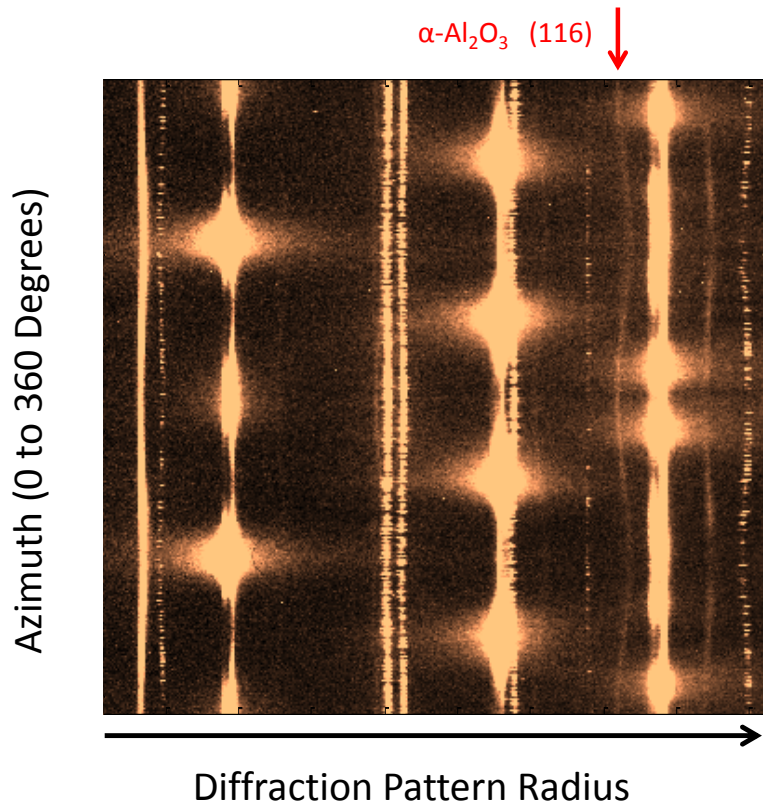
Figure 3.6: Radial transform of α-Al_2O_3 (116) in aged specimen

3.5   Measurement Methods for Cylindrical Coatings

In efforts to achieve the full strain tensor which consists of the radial, circumferential, and axial components, 2 methods were tested on the as-coated specimen. These are shown in Figure 3.7. In Method 1, the x-ray beam grazes the edge of the sample, from which axial and radial components of strain can be measured within the layers of the thermal barrier coating. In Method 2, the x-ray beam is passed through the center of the sample, from which axial and circumferential strain components can be measured. Since these XRD measurements were 2D with a plane normal to the beam direction, multiple locations on the curvature were tested to demonstrate the ability to obtain the full strain tensor.

The effectiveness of these two methods in obtaining strain measurements within the TBC layers was analyzed. In Method 1, 2D XRD measurements were taken tangentially by grazing the beam at various depths to attain diffraction rings for phases in the YSZ, TGO and Bond Coat.
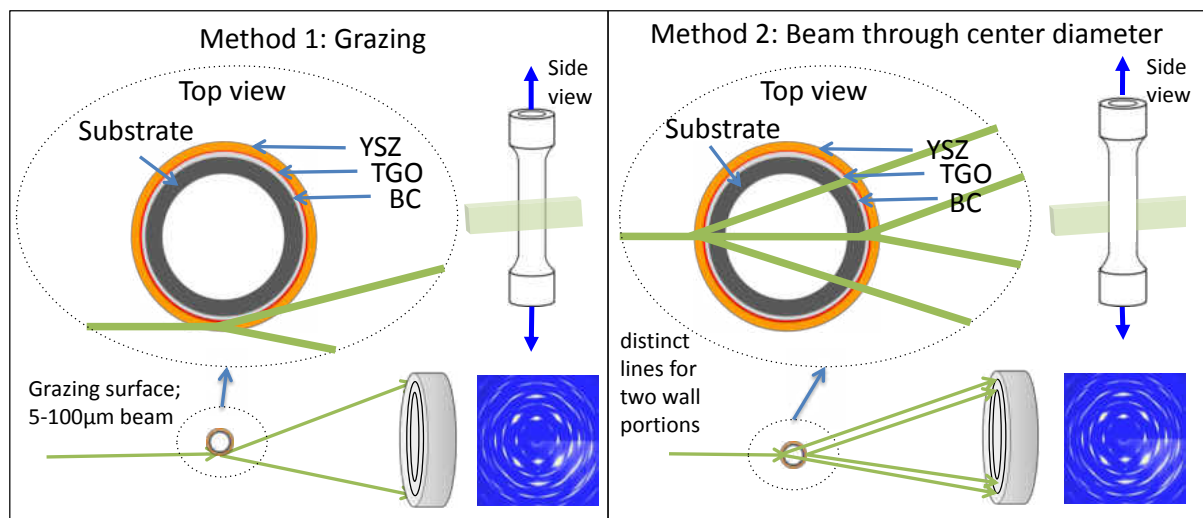
Figure 3.7: Method 1: Grazing surface from 5-100 μm. 2D detector measures axial and radial components of stress. By moving the sample into the beam, information from different layers is collected. Method 2: Direct Transmission along the center line. 2D detector measures wall-thickness-averaged axial and circumferential components. [75]

In Method 1, in which the beam grazed the cylindrical sample, data was collected with a beam size of (30x300) μms (width by height) and a frame count of 10 frames at one frame per second. To determine the geometry effects on the capability of distinguishing different phases, the XRD measurements were taken from the sample center to the YSZ outer radius using a step size of 30 μm under zero loading conditions. This average intensity gives insight into how the diffraction volume as well as the textured lattice plane

reflection intensity varies when the x-rays penetrate different locations on the geometry. Figure 3.8 shows the changes in intensity for the t'-YSZ peak (111) through the entire scan. The YSZ scan displays a steady increase in measured intensity as the window approaches the YSZ inner radius of about 4.11 mm.
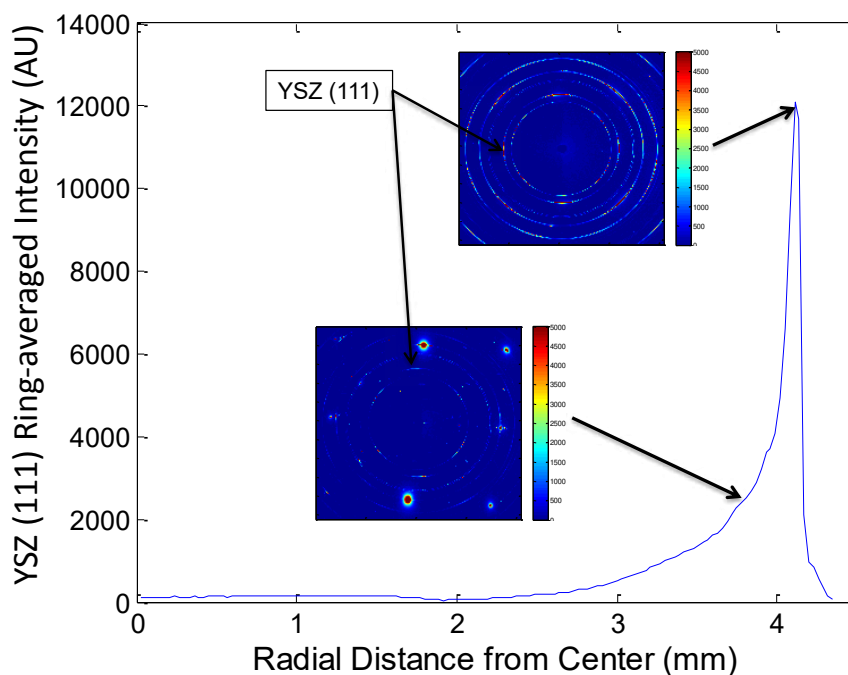
Figure 3.8: Detected YSZ intensity from sample center to sample edge [75]

To display the phases at various depths, the XRD results are shown for Method 1 with grazing locations tangential through the YSZ and just inside the Bond Coat as well as Method 2 with penetrating directly through the center of the specimen. These locations are depicted in Figure 3.9 as A, B and C. The averaged intensity vs. d-spacing is compared at each of these locations with phase identification in Figure 3.10. At location C, when shooting directly through the YSZ layer only, t'-YSZ is the most prominent phase measured. At location B, the beam is grazing the substrate and penetrating through the

bond coat, TGO, and YSZ. Here, the two phases from the bond coat, β-NiAl phase and a solid solution γ-Ni phase, are detected.
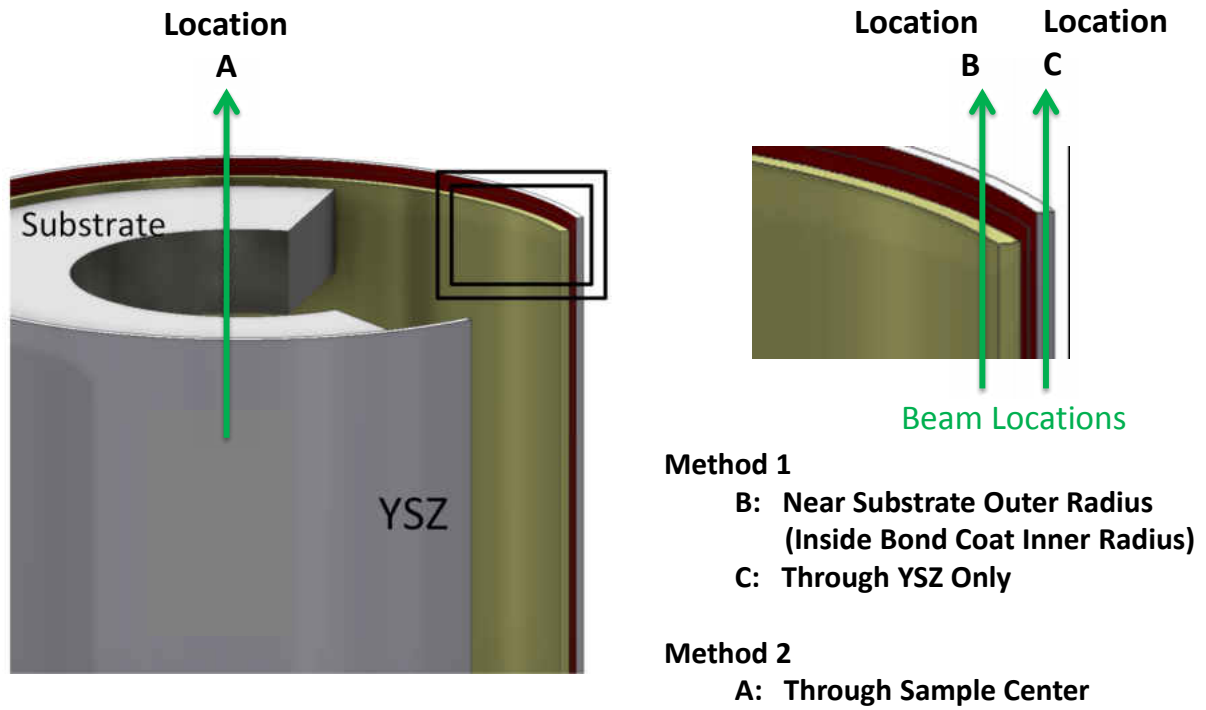
Figure 3.9: XRD acquisition beam locations

The XRD results at location A highlight the need to test parameters such as window size and exposure time when measuring at the sample center. Precise measurement of the radial peak position is required and its deviation from a strain free radial position is then used for accurate strain calculations. The presence of false doublets due to double diffraction from the front and back sides of the sample along with large, highly textured reflections from the Inconel 100 substrate presents complexities when attempting to analyze the 2D axial and circumferential strains at this location (Method 2).
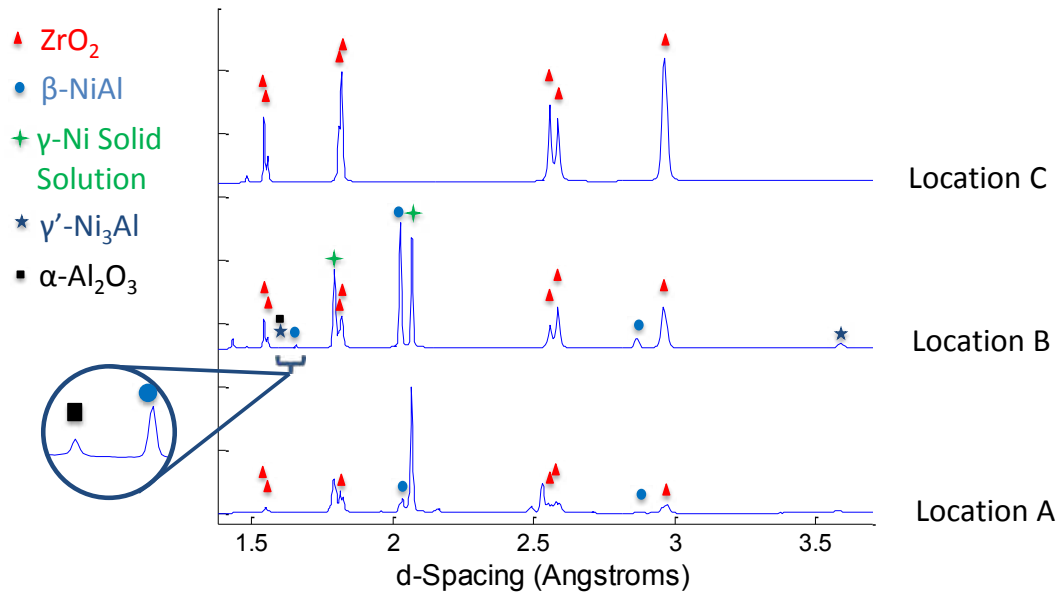
Figure 3.10: XRD results for beam locations [75]

3.6   Texturing

Due to the EB-PVD application process, the YSZ top coat consists of a columnar structure normal to the bond coat surface. This results in texturing with a preferred orientation displayed Figure 3.11. This displays the measured intensity versus ring azimuth angle from 0 to 360° for YSZ (111), YSZ (200), and NiAl (110). The texturing displayed here for the YSZ is measured with an x-ray beam tangential to the cylindrical surface, providing a 2-D measurement plane which is parallel to the YSZ columns. In comparison, the MCrAlY bond coat exhibits randomly oriented grains. Texturing such as this is an important factor for strain calculations. Preferred grain orientation has a large effect on anisotropy and also presents much difficulty in fitting strains. For the results here, the (111) plane was used in all strain calculations for the YSZ.
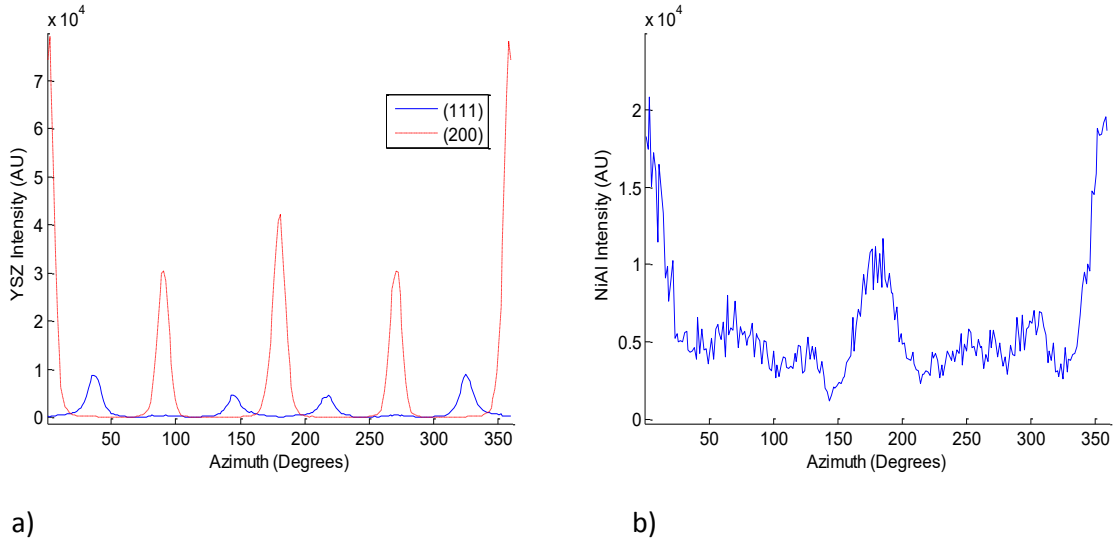
Figure 3.11: Texturing displayed through intensity versus azimuth for (a) YSZ (111) and (200) and (b) NiAl (110)

3.7   Thermal Expansion

The in-situ measurement of lattice spacing can provide valuable information on thermal expansion of each of the phases. Calculation of the lattice spacing as temperature increases were used to measure these thermal expansion coefficients. To account for strain effects, the strain free angle derived in the strain section below is used for these calculations. Shown in Figure 3.12 is the lattice constant (a) for NiAl versus temperature. This resulted in coefficient calculated for NiAl to be 17.69e-6. Shown in Figure 3.13 are the lattice constants (a) and (c) during temperature ramp-up. These were calculated by fitting the d-spacing of the (200) and (002) peaks for the tetragonal t'-YSZ phase. From this curve, thermal expansion coefficients were calculated to be 12.127e-6 and 11.234e-6 for (c) and (a) respectively.

47
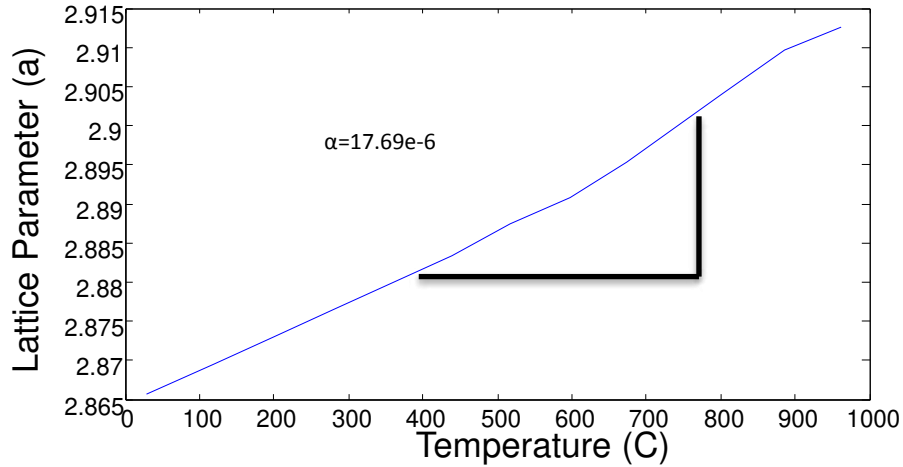
Figure 3.12: NiAl thermal expansion of lattice constant

3.8 Strain Calculation

As the lattice structure is strained, the measured ring patterns become distorted. This is due to the Bragg's Law effect where a lattice strain will produce an inversely related change in 2θ. Therefore, on a particular axis in the measurement plane, a change in 2θ in that direction can be measured as a corresponding radial shift. Hydrostatic strains within the measured volumes will produce a uniform radial shift while deviatoric strains will cause an elliptical distortion. The measured radial deviation of these rings can then be used to calculate 2-D strains. The micro-strains measured within the grains provide the elastic strain response of each phase. This elliptical deviation from a circle with a strain free radius provides the deviatoric micro-strain tensor for that particular lattice plane [61]. To measure the directional strain within the measurement plane, the diffraction ring is binned and integrated azimuthally (η) as shown in Figure 3.14. Pseudo-Voigt profiles

48

were then fit to the intensity versus radius resulting from the bins of the desired peak to determine radial position, peak intensity, and full width half max (FWHM).
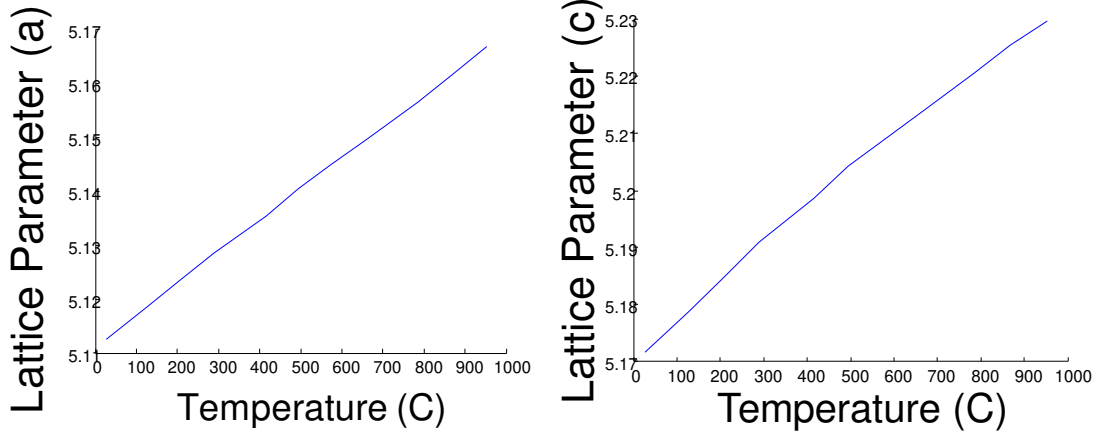
Figure 3.13: YSZ thermal expansion of lattice constants

The radial deviation is calculated by comparing the measured radial position to a strain free radius (R_o). Strain-free radius values (R_o) are determined from a method of measuring a strain-free azimuth angle, which is shown as η^* in Figure 3.15. This method is further described in the work by Almer et al [3]. The reference angle, η^*, is determined by measuring the distortion of the diffraction ring while applied tensile loading is increased. This provides the reference angle of which zero deviatoric strain occurs. This gives a value of R_o at each measurement independent of temperature.

The strain tensor calculations are then conducted using the 2-D fundamental strain equation [36]. For this calculation, the coordinate system must be converted between the sample and detector coordinates. Figure 3.16 displays the rotation axes (ω, ψ, ϕ) and their relationship to the laboratory coordinate system (X_L, Y_L, Z_L) and sample axis (S_1,

S$_2$, S$_3$). For the experiments described here, the variables simplified to ω=90°, ϕ=0°, and ψ=0°.
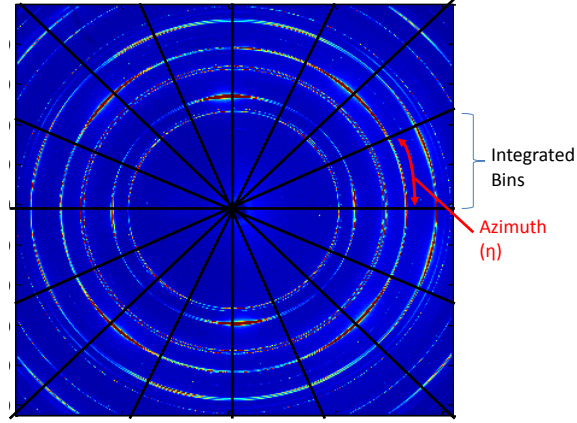
Figure 3.14: Azimuthally integrated bins

The measured radial displacements are input into the fundamental strain equation which is described as:

$$\varepsilon_{\phi\psi} = h_1^2\varepsilon_{11} + 2h_1h_2\varepsilon_{12} + h_2^2\varepsilon_{22} + 2h_1h_3\varepsilon_{13} + 2h_2h_3\varepsilon_{23} + h_3^2\varepsilon_{33} \tag{3.2}$$

where:

$$
\begin{bmatrix} h_1 \\ h_2 \\ h_3 \end{bmatrix} =
\begin{bmatrix}
-\sin\omega\sin\psi\sin\phi & \cos\omega\sin\psi\sin\phi & \\
 & & -\cos\psi\sin\phi \\
-\cos\omega\cos\phi & -\sin\omega\cos\phi & \\
\sin\omega\sin\psi\cos\phi & -\cos\omega\sin\psi\sin\phi & \\
 & & \cos\psi\cos\phi \\
-\cos\omega\sin\phi & -\sin\omega\sin\phi & \\
-\sin\omega\cos\psi & \cos\omega\cos\psi & \sin\psi
\end{bmatrix}
\begin{bmatrix} -\sin\theta \\ -\cos\theta\sin\gamma \\ -\cos\theta\cos\gamma \end{bmatrix}
$$

$$\tag{3.3}$$

50
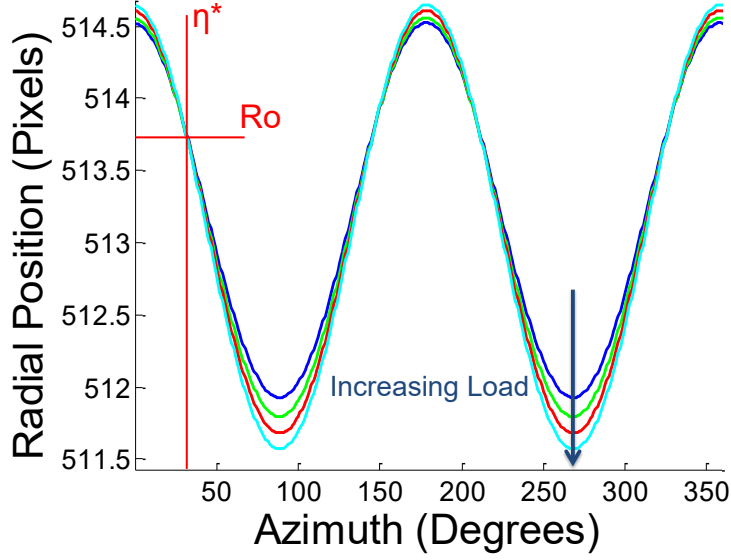
Figure 3.15: Determination of strain free azimuth reference angle (η^*) and strain free radius (Ro)

Shown in Figure 3.17 is an example of a resulting strain fit. Measurements obtained consisted of the radial e_{11} and axial e_{22} components. Therefore, an assumption must be made for circumferential e_{33}. For the purpose of this work, the in-plane equibiaxial assumption was made that $e_{33}=e_{22}$. This experiment benefits largely with the use of high-energy in minimizing the weight of this assumption for strain calculation. The use of high-energy x-rays (65 keV) results in small bragg angles, with 2θ values for the peaks analyzed between 2°and 6°. This means that the measured diffraction vectors are nearly aligned with the e_{11}-e_{22} plane, such that the coefficients in the fundamental strain equation for e_{11} and e_{22} are near unity while the e_{33} coefficient is negligible, with a value between 0.001 and 0.003 for the two values of 2θ. These radial (e_{11}) and axial e_{22} strains are averaged over distances from the interface due to the curvature of the coating. With

51

the radial position being much greater than the coating thickness, the contribution of the circumferential strain component on the measured e_{11} strain is expected to be minimal.
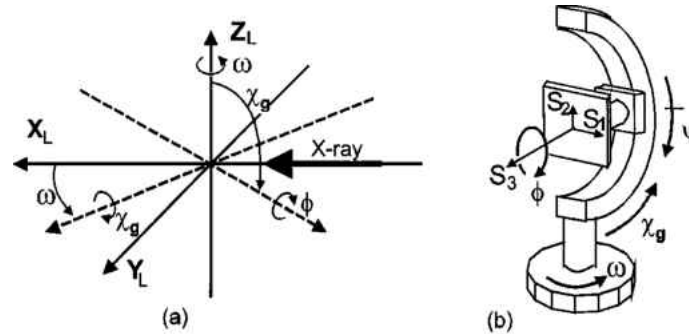
Figure 3.16: Orientation of the a) laboratory coordinate system and b) sample coordinate system [36]
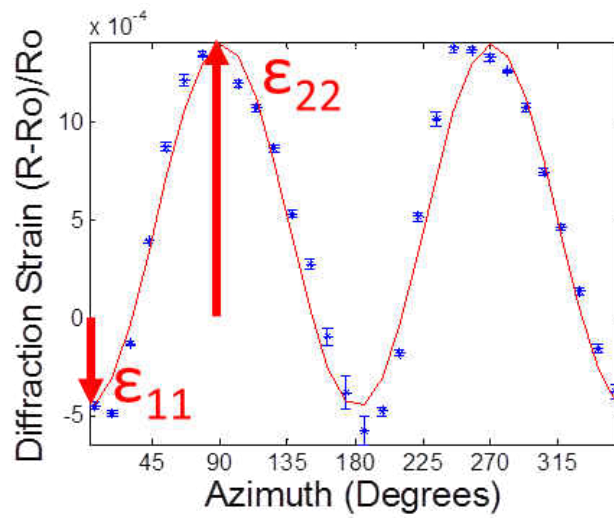
Figure 3.17: Strain fit of radial e_{11} and axial e_{22} components

3.9 Stress Calculation

Methods such as the sine squared stress calculation require tilting of the specimen to obtain diffraction variation as the contribution from the e$_{33}$ strain is increased [35]. This is often not feasible for in-situ tests. Sample loading physically limits the ability to tilt while the desire to obtain the transient response limits the measurement time to where tilting of the specimen is not possible. Therefore, stress calculations were done through converting the 2-D strain measurements using Equation 3.4. Here, the S$_1$ and S$_2$/2 variables are the x-ray elastic constants (XECs). These are constants which are derived from the materials single crystal elastic constants C$_{ijkl}$ and are a function of the (hkl) plane to account for anisotropy. These can be calculated through various methods such as Reuss, Voigt, and Kr$'$oner-Eshelby. The strains measured through this process are averaged over a volume of crystallites. The Reuss method assumes constant stress across the crystallites while the Voigt method assumes constant strain. The Kr$'$oner-Eshelby lies between the limits of the prior two methods and provides elastic moduli which is close to what is seen experimentally [58]. Although the e$_{33}$ component was shown to have a negligible weight on the strain calculation, it does have an effect on the stress calculation. This assumption has proved especially critical due to its distance from the interface where the equibiaxial assumption becomes less valid.

$$\sigma_{11} = \left(\frac{1}{S_2/2} \right) \left(\varepsilon_{11} - \left(\frac{S_1}{S_2/2 + 3S_1} \right) (\varepsilon_{11} + \varepsilon_{22} + \varepsilon_{33}) \right) \qquad (3.4)$$

3.9.1 Comparison of Methods for Cubic Structure

Results for the bond coat have shown evidence of the invalidity of applying the typical equibiaxial assumption used for flat coatings. This deviation from equal strains for axial and circumferential is displayed in Figure 3.18. This displays curves fit to the radial displacement of the diffraction rings for locations transmitting through center and tangential to the bond coat.
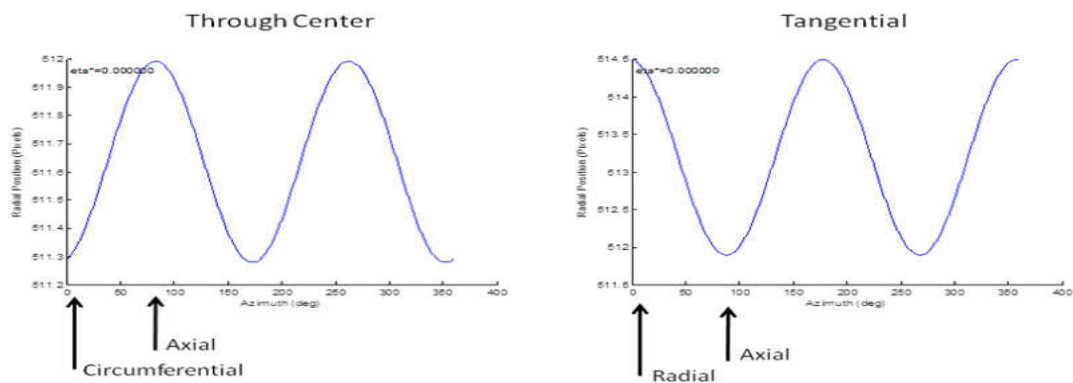
Figure 3.18: Comparison of radial displacement fit to diffraction ring radius data for through center and tangential highlighting the deviatoric in-plane strains

Despite both being in-plane for the through center location, the radial curves indicate that the circumferential strain shows a much higher tensile radial position when compared to the longitudinal radial position. These effects can hinder the stress measurements of these types of multi-layered tri-axially stressed coatings. With the tri-axial stressed state of multilayered coatings on cylindrical surfaces, multiple locations on the geometry may not be feasible under dynamic loading conditions. Comparing strain of multiple planes

54

in anisotropic grains, can serve as an accurate method for determining an accurate full 3-D tensor with 2-D measurements.
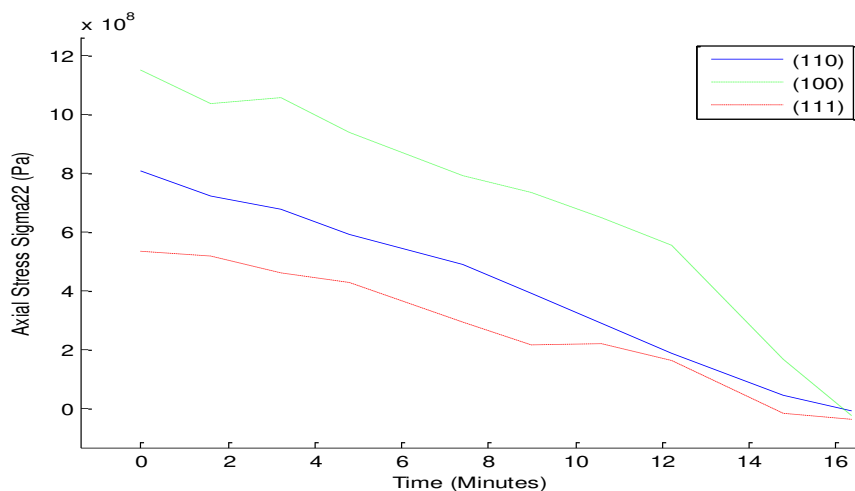
Figure 3.19: Comparison of NiAl stress calculated from different lattice planes during temperature ramp up

To further display the effects from this assumption, stresses are calculated for different lattice plane within the NiAl during temperature ramp-up and displayed in Figure 3.19. These stress calculations using the measured strains of three lattice planes in the NiAl has shown large disparity between each other. While micro-strains are expected to deviate between lattice planes, the calculated stress is expected to be equal using the hkl dependent elastic properties. Therefore, using the measured strains of multiple planes and equating their stresses, can give information on the magnitude of error of the error in the e_{33} assumption as well as the presence of a hydrostatic strain shift of the 2-D measurement. The development of a technique to account for these type of erroneous assumptions, would be extremely valuable to the synchrotron XRD strain community

as the situation of a tri-axial stress present in internal volumes is quite common. An innovative analysis technique for accounting for this effect is developed here. The benefit of micro-strain measurements taking with XRD is that the anisotropy of the grains large in the difference between the different phase planes.
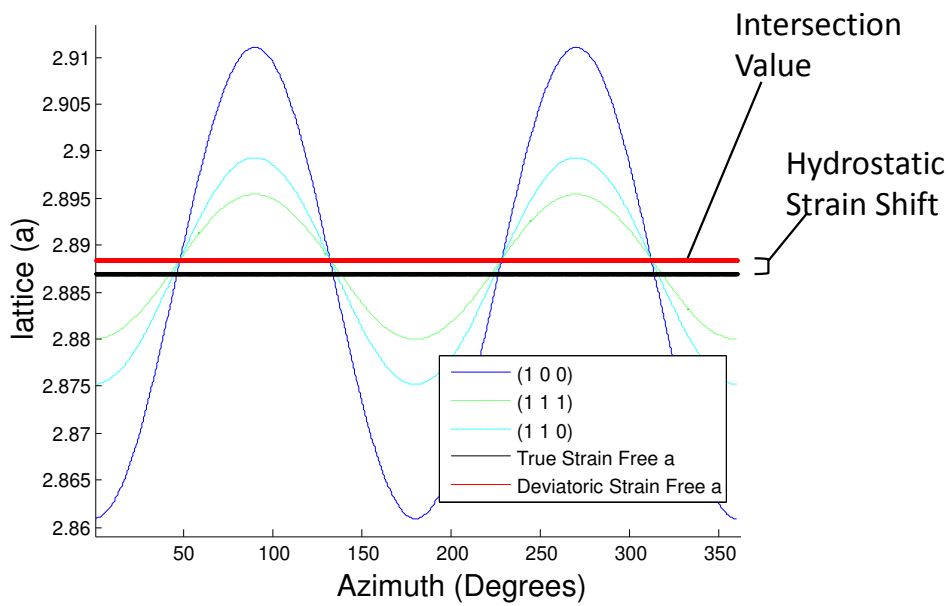
Figure 3.20: Simulated comparison of lattice constant (a) calculated from different cubic lattice planes for determining intersection point

To test the ability of anisotropy in the Nial to provide information on the tri-axial state of stress, models were created to simulate the diffraction under a defined stressed state. With these simulations, a stress and strain state can be defined and known before inputting the simulated diffraction rings into the same analysis used for the experimental process. This provides a measure of error between the actual and measured state of strain and stress. From these simulations, a method was developed to directly measure the

deviatoric strain and stress of cubic materials without the need for unknown assumptions. It was determined that comparing the cubic lattice constant (a) for multiple lattice planes of an anisotropic material provides the deviatoric strain free azimuth angle. This is displayed in Figure 3.20 for simulation results. Under loading conditions which are largely deviatoric, this approximation proves to be very accurate.
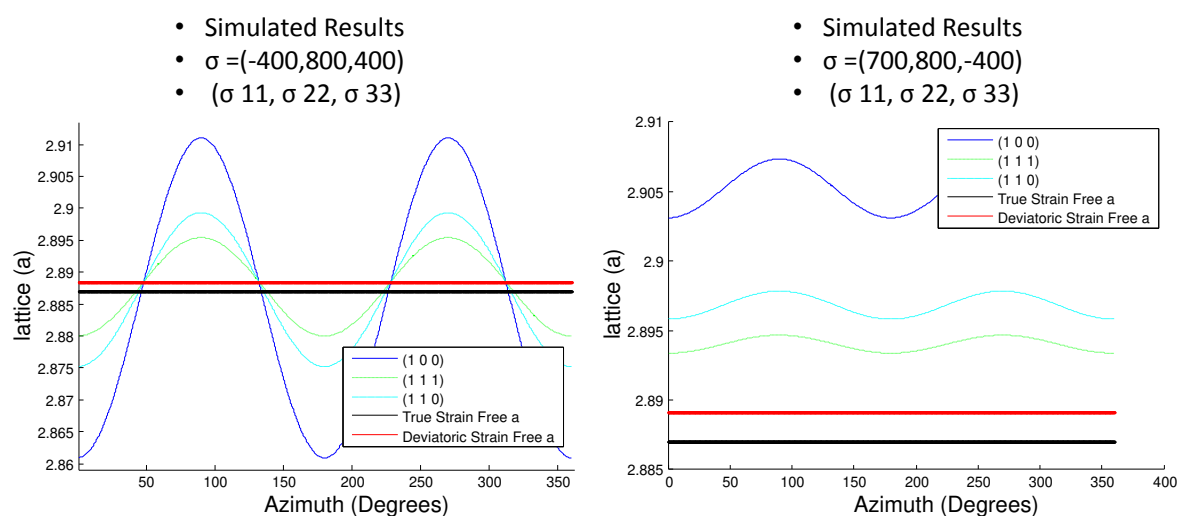
Figure 3.21: Simulation of lattice constant comparison under different loading conditions

As the stress conditions become increasingly hydrostatic, these curves can separate to a point where no intersection occurs. This is displayed in Figure 3.21. To account for this, the lattice constant is plotted versus $\sin^2$(azimuth). This provides linear trend where the slopes can be used to calculate the intersection. This is displayed in Figure 3.22.

This deviatoric strain free value can then be used to calculate the e_{33} component through comparison of the 2-D strain values. By constraining the σ_{22} (or σ_{11}) and σ_{33} to be equal to their corresponding values for multiple planes, the e_{33} can be directly solved

for. This value is then input into the stress equation for a single plane to obtain the deviatoric stress. Through simulations, this method has proved its ability to directly measure the deviatoric component of the stress and strain tensor. This method can be an extremely valuable tool for determining the stresses in internal materials where the stress tensor is largely deviatoric. With the increased work with synchrotron x-rays where internal measurements are feasible, this method provides the ability to take these measurements without the need for assumptions for the unknown strain (e_{33}). The implementation of this method for an experimental measurement is shown in Figure 3.23.
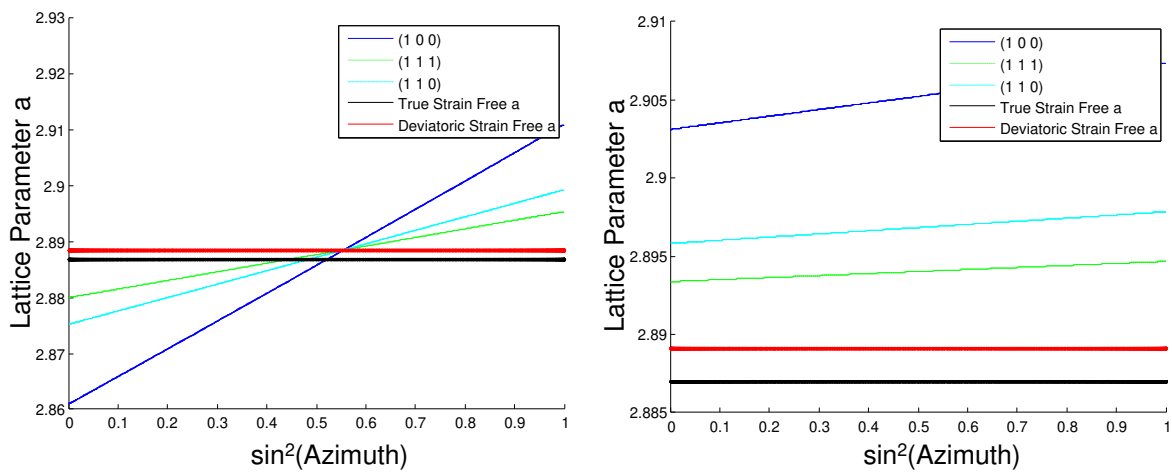
Figure 3.22: Simulation of lattice constant comparison with lattice constant plotted versus $\sin^2(\text{azimuth})$
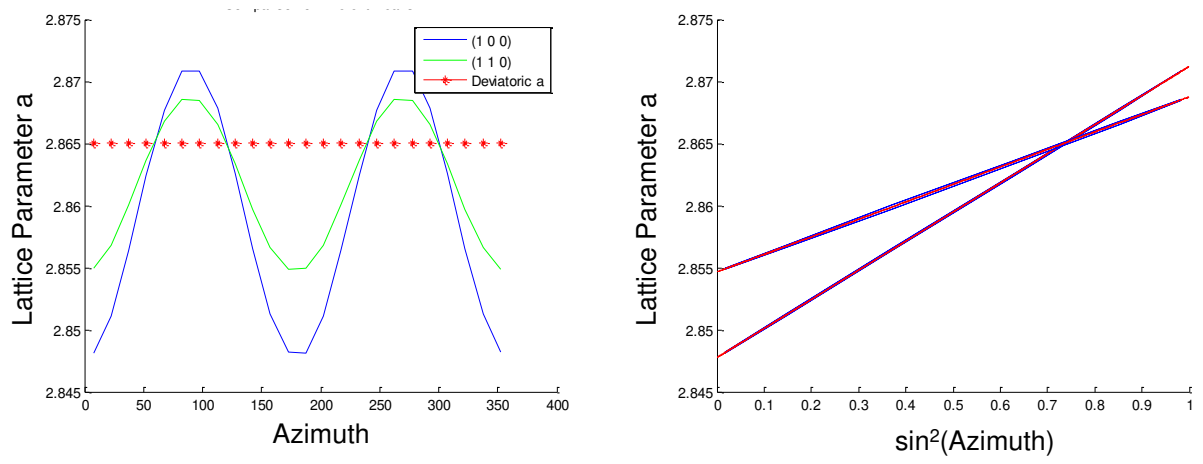
Figure 3.23: Experimentally implemented comparison of lattice constant for NiAl deviatoric strain measurement

CHAPTER 4
IN-SITU MECHANICAL RESPONSE OF EARLY CYCLE SPECIMENS

To initially investigate the mechanical behavior of TBCs, testing was conducted on As-Coated specimens. A combination of cycles and other experiments were conducted on two samples and, therefore, the samples are better classified as "early-cycle" specimens. The results presented here consist of bond coat and top coat results only due to the difficulty in obtaining enough diffraction volume in the TGO of the early-cycled specimens for the purpose of displaying trends during loading variation. To study the strain behavior early cycled specimens under loading conditions relevant for gas turbine blades in aircraft engines, three types of experiments were conducted: (i) single flight cycles, (ii) tensile tests at various temperatures up to 1,000°C, and (iii) thermal gradient tests at high temperature. These novel measurements have revealed previously unseen in-situ strain response of the TBC that can contribute towards enhancing coating lifespans.

Shown in Figure 4.1 are the measurement locations which were used for the experiments. Throughout all experiments the beam scanned through the coating layers with a window and step size of 30 μm. For the experiments on the early-cycled specimens, measurements were taken with a beam energy of 65 keV, resulting in full diffraction rings to a d-spacing as low as 1.29 Angstroms. Diffraction rings are recorded for each lattice plane in the multiple coating layers using an 85 second scan with 10 discretized steps through the coating thickness. The results presented here will show either how a single location near the interface or a through thickness scan changes during transient loads as shown in Figure 4.1. This will show results for both the axial (in-plane) e_{22} and radial (out-of-plane) e_{11} strains.

60
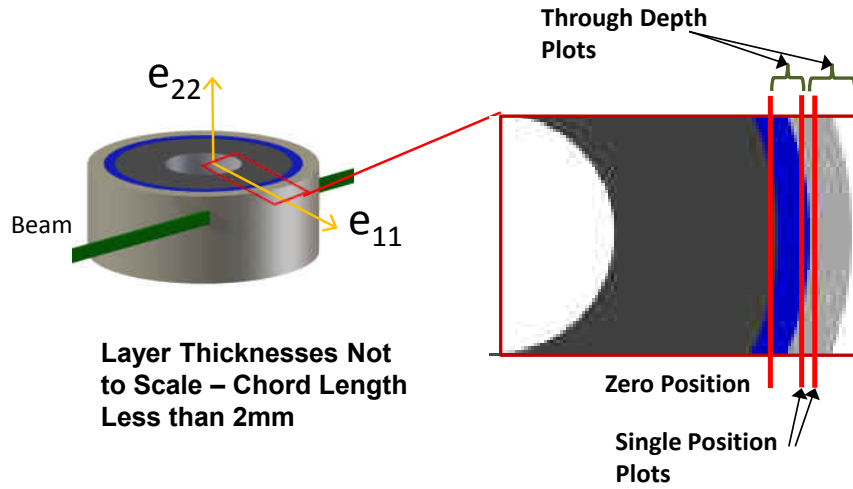
Figure 4.1: Coating locations for scanning and single point measurements

4.1 Single Flight Cycle Strain Evolution

For single flight cycle tests, the outer surface temperature was ramped up through duration of 20 minutes to 1,000°C and held for 40 minutes before ramping down to room temperature while maintaining a constant mass flow of cooling air and a mechanical load. TBC models, which are used to predict the fatigue effects that cause different failure modes, rely on the accuracy of the internal stresses and strains during high temperature cycling calculated by the model. To validate such models, in-situ data is required to show how the depth resolved strain changes under these in-cycle loading conditions. This experiment provides previously unseen strain information for a complete TBC coating under thermal gradient and mechanical conditions representative of an operational cycle. For the single flight cycle measurement, the outer surface is exposed to a temperature

profile with ramp up and then held at high temperature while the internal cooling and applied mechanical load are held constant.

Cycles were conducted for the different combinations of 16, 32, 64, and 128 MPa loads and 30, 50, and 75% coolant mass flow rates. The cycle shown in Figures 4.2 and 4.3 was conducted at 75 SLPM (75%), and 64 MPa nominal tensile stress. The residual strain at room temperature, especially in the YSZ, has shown a large dependence on number of previous cycles for early cycling. Therefore, only one cycle is displayed here. Roughly three 80 minute cycles were completed prior to the cycle presented here.
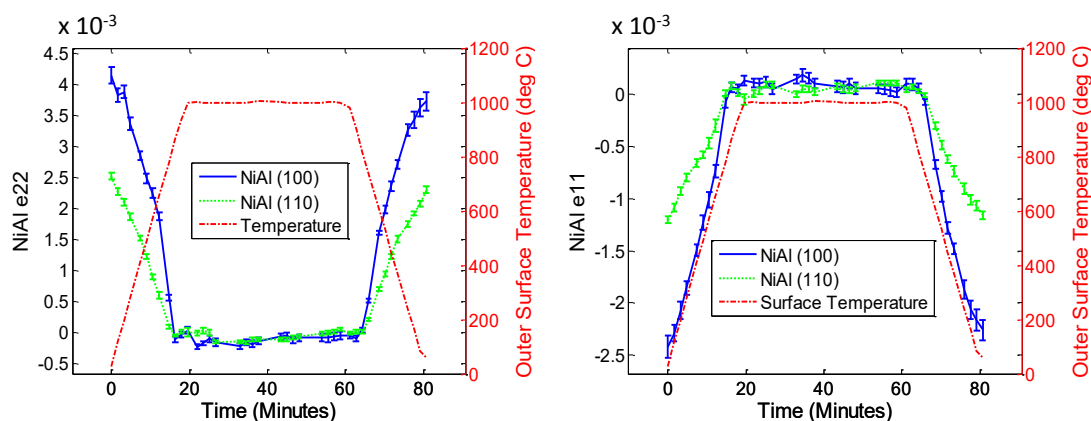
Figure 4.2: Bond Coat Beta-NiAl Single Cycle Strain for in-plane (e_{22}) and out-of-plane (e_{11})

The strain of a single location is shown for both the bond coat and YSZ throughout a single flight cycle. These locations are near the bond coat/top coat interface as shown in Figure 4.1. The strain results for NiAl for a single location throughout the cycle is

shown in Figure 4.2 and include lattice planes of both (100) and (110). Throughout the temperature increase from room temperature to 1,000°C, the strain ratio of the (100) to (110) planes varies between 1.6 to 2.2. This highlights the anisotropy of the NiAl phase. It also validates the strain values as the elastic modulus ratio of the two planes is very close to the inverse of the strain ratio. Room temperature elastic moduli for the (100) and (110) were calculated to be 97 and 188 GPa, respectively, from experimentally determined elastic compliance constants [76]. Due to the fine grained nature of the bond coat, anisotropy is only seen in microstrain.
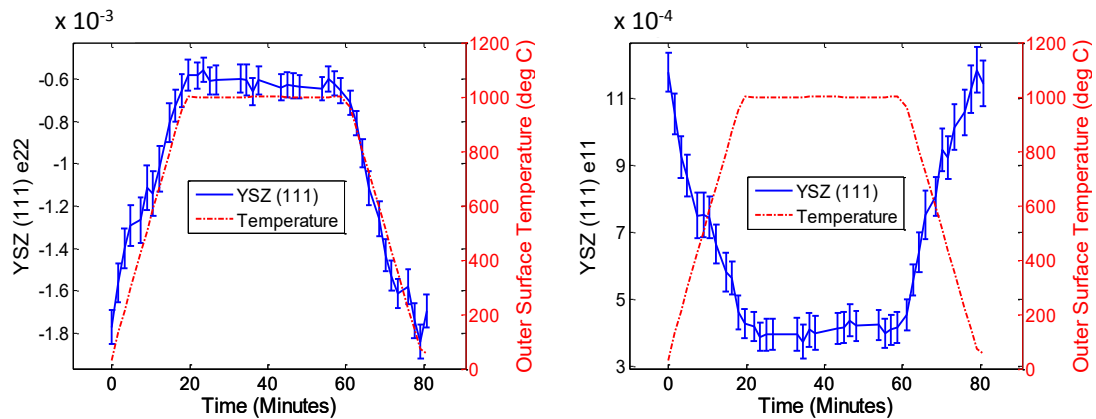
Figure 4.3: tYSZ Single Cycle Strain for in-plane (e_{22}) and out-of-plane (e_{11})

At room temperature, the bond coat shows a very large tensile residual strain in the in-plane (e_{22}) direction. As it is ramped up to high temperature, it then relaxes to zero strain. The bond coat NiAl has displayed a changing e_{22} strain per temperature rate for above and below 600°C. The (100) plane strain rate was -3.95E-6 (mm per mm)

per °C between 25°C to 600°C while increasing in magnitude to -4.95E-6 (mm per mm) per °C, between 600°C to 1,000°C. As can be seen by the strain slope above 600°C, the strain linearly increases to zero strain at 800°C. At this point, no further changes in strain can be seen with increased temperature. The shift to near zero strain at high temperature is expected due to the TBC's manufacturing temperature of 1,000°C. As no phase changes can be seen, this is likely due to the initiation of creep relaxation in the bond coat. A ductile to brittle transition has been associated with the activation of grain boundary creep at similar temperatures around 600 °C [63]. During temperature shifts from application and operating temperatures to room temperature, the TBC system develops large residual stresses as the layers contract at different rates. Figure 4.3 displays the YSZ (111) strain near the interface throughout a cycle. The YSZ exhibits compressive in-plane (e_{22}) strains at room temperature displaying that the YSZ has a smaller thermal expansion coefficient relative to the bond coat and substrate. It also displays a similar shift to near zero at high temperature with some remaining compressive e_{22} residual strain.

Figure 4.4 displays the through thickness strains for NiAl (110) and YSZ (111) for various temperatures during ramp up to 1000 °C. Here, the outer radius of the bond coat displays the greatest shift when moving to high temperature. This is likely due to the large difference in thermal properties between the bond coat and TGO. More prominently than the bond coat, the YSZ also shows that the largest shift during temperature ramp-up along with the largest high temperature residual strains occur at the interface. This observation can be attributed to the specific microstructure of EB-PVD YSZ coatings

which display a gradient in porosity, corresponding to a gradient in elastic modulus, from low porosity near the interface to increasing porosity towards the surface. These in-cycle results highlight the importance of strains near the interface during cyclic conditions. Strain gradients across the layers provide valuable information on the loading state as well as the material's behavior.
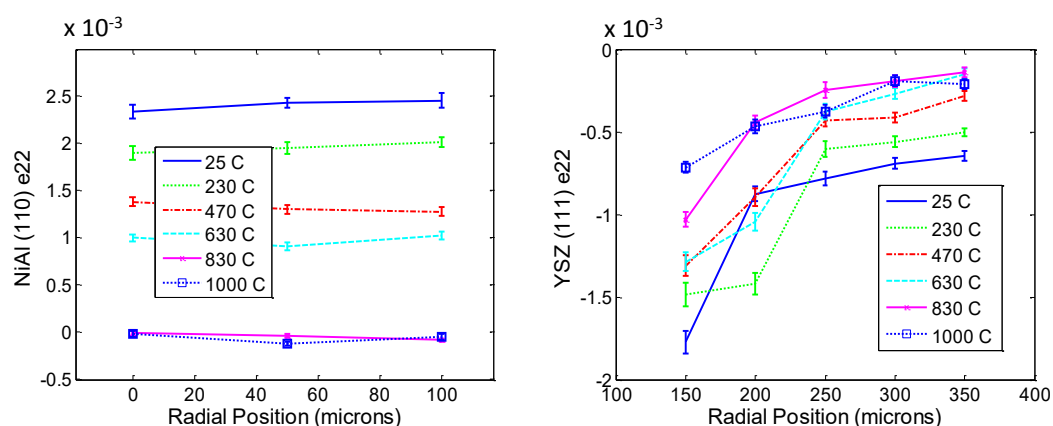
Figure 4.4: Through thickness in-plane (e_{22}) strain for β-NiAl and t-YSZ during cycle ramp up

4.2 Strain Response to Tensile Tests at Temperature

The strain response to mechanical loading was tested through repeated stepwise mechanical load increases at five different homogeneous temperatures (no superposed thermal gradient) from room temperature up to 1,000 °C. Mechanical loading of the coating plays

a role in the triggering of some failure modes. It is therefore important to understand how the strains vary with applied load. The effects of mechanical loading at various temperatures are shown using the loading conditions shown in Figure 4.5. Locations in both the bond coat and YSZ, near the interface, were monitored as the applied load was ramped up with loads of 16, 32, 48, and 64 MPa at each temperature.
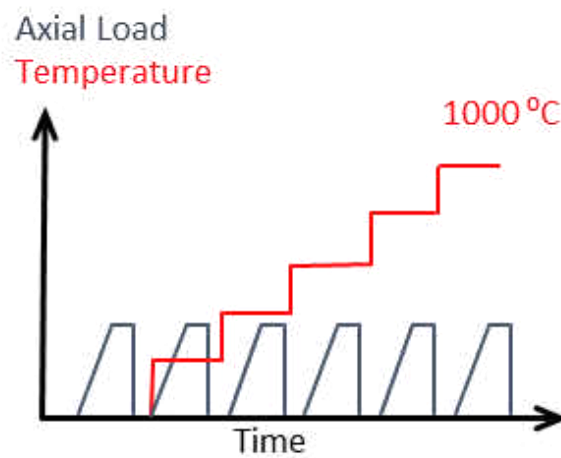
Figure 4.5: Loading conditions displaying tensile tests conducted at various temperatures

Displayed in Figure 4.6 are the changes in e_{22} strain versus changes in applied nominal stresses for bond coat and YSZ. This displays that the NiAl in the bond coat gradually bears less of the applied load as temperature increases. This is demonstrated by the decreasing slope of the strain to applied stress with increasing temperatures. At 800 °C and 1000 °C, the slope of strain of the bond coat to nominally applied load, is near zero and also exhibits zero strain shift between temperatures. As the micro-strains averaged over the grains only displays elastic strain, this highlights the existence of inelastic behavior

(plasticity and creep) in the bond coat at and above 800°C. The lack of micro-strain present internally within the NiAl grains at elevated temperature with increased loads suggests the possibility of sliding of the grain boundaries between the NiAl and Ni phases which could affect the structural integrity of the bond coat over cycling. The strains presented for the YSZ layer show much less susceptibility to inelastic behavior. This ceramic layer maintains a constant slope for temperatures up to 800 °C. At 800 °C, the YSZ layer displays the same slope up to 48 MPa nominal load. With the increase to 64 MPa, no strain response can be seen. This suggests that the YSZ exhibits an inelastic response at 800 °C above this load. At 1000 °C, the strain response appears to be primarily inelastic.
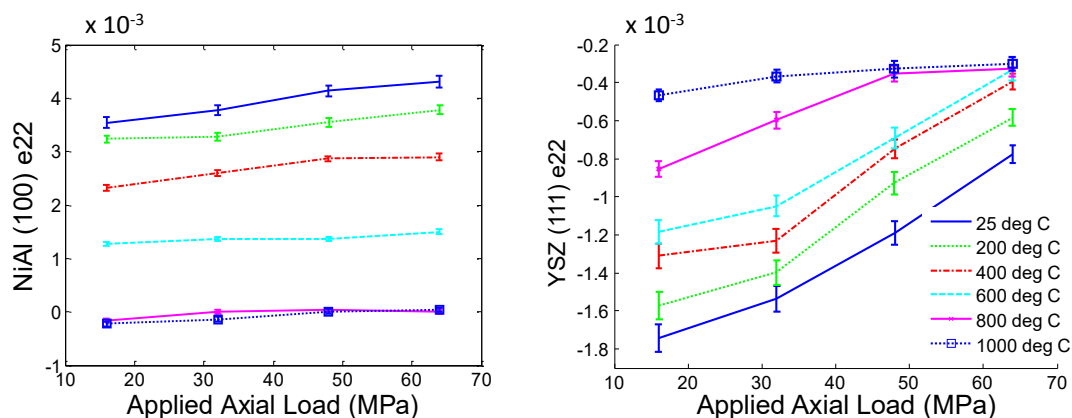
Figure 4.6: In-plane (e_{22}) strain during mechanical testing for β-NiAl and t-YSZ during temperature increase

4.3   Strain Effects from Thermal Gradients

A large factor for dictating the various failure modes is thought to be the magnitude of the applied thermal gradient across the coating layers. Therefore, it is important to isolate the effects of thermal gradient on the corresponding strain gradients across the layers. To isolate the strain effects due to thermal gradient, the sample was uniformly heated to a high temperature of 1,000°C. The inner surface of the substrate was then cooled slowly while the surface temperature was held constant as displayed in Figure 4.7.

Strains were measured through the thickness as the thermal gradient was increased from zero to 100% corresponding to an approximate temperature drop across the YSZ layer of 150 °C. At high temperature, the bond coat displayed no variation in strain due to thermal gradient. This is likely due to the dominant creep response experienced at this temperature. However, the gradient has an effect on the YSZ strains, which is substantial near the interface with the bond coat.

Figure 4.8 shows that with increasing thermal gradient, the YSZ demonstrates minimal change in strain from the outer surface into the middle of the layer, while the inner region of the YSZ displays a significantly increasing compressive strain and thus higher strain gradient. The YSZ displays a significantly increase in strain at the interface with a 45% compressive. The strain at a single location near the interface is shown in Figure 4.9. This further highlights the effect that increased gradient has on the compressive stress in early cycled YSZ coatings.
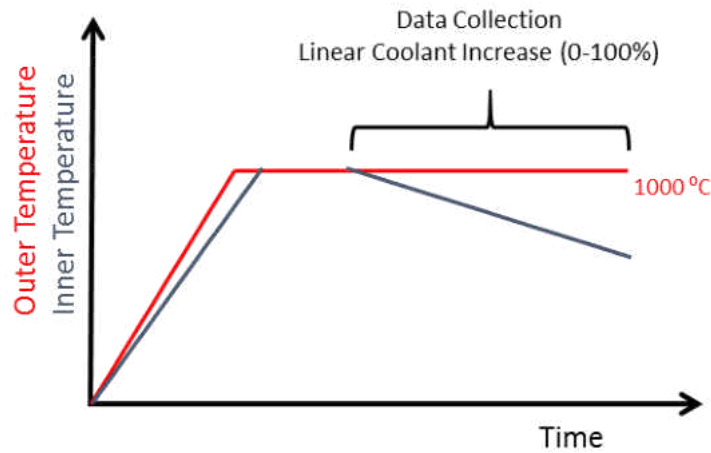
Figure 4.7: Thermal loading of the sample with linear increase in the imposed thermal gradient

The observed strain response on the variation of thermal gradient by means of variation of cooling air mass flow can be attributed to a combination of several effects, related to the microstructure and the specimen geometry. The EB-PVD coating has a higher density at and near the interface than towards the surface with a high gradient in porosity near the interface up to about 100 μm distance to the interface. With increasing distance from the interface the porosity does not change much. Consequently, the thermal conductivity and the elastic modulus of the coating decrease with distance from the interface, resulting in opposite effects on the strain. The effect of an increase in thermal conductivity is a decrease of a thermal gradient in the case of a constant heat flux. A decrease in thermal gradient would result in a decrease of strain gradient if the elastic properties were homogeneous. Since in the case of columnar EB-PVD YSZ coatings the

69

macro-scale elastic modulus displays a gradient which increases towards the interface, strain and strain gradients in the YSZ phase would increase towards the interface if the thermal gradient would be constant. The tubular specimen geometry results in an increase of heat flux from the outer surface to the cooled inner surface which would result in an increasing thermal gradient towards the interface if the thermal conductivity would be homogeneous. In addition to the microstructural effects, the reduction in temperature near the interface can also reduce the level of unmeasured inelastic strain present. A combination of the listed effects could create or contribute to the trends in changing strain gradient across the thickness as is displayed here.
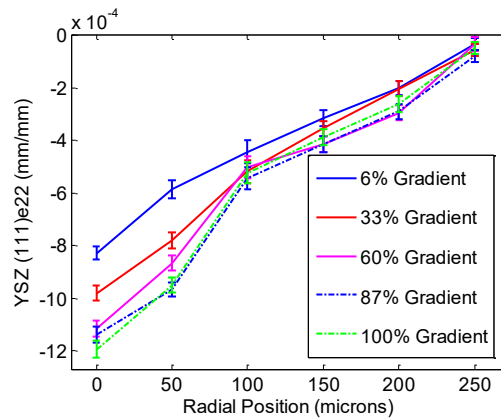
Figure 4.8: t-YSZ (111) e_{22} strain displayed through the YSZ thickness at various thermal gradients
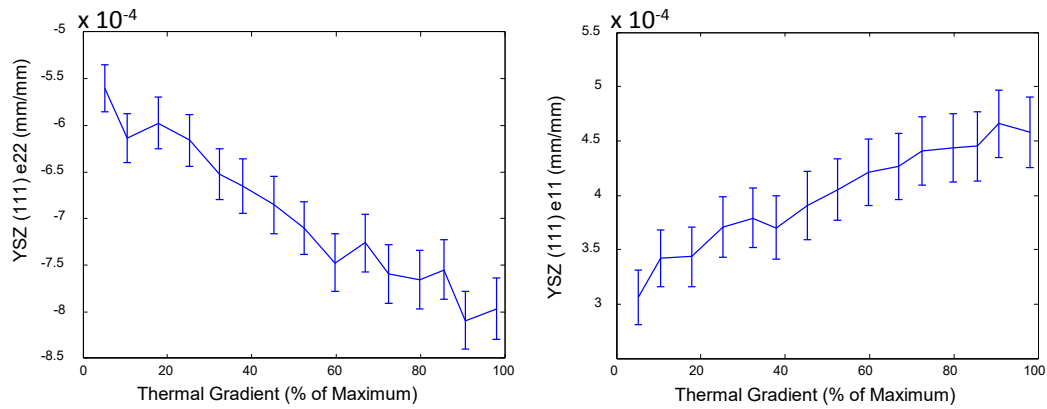
Figure 4.9: t-YSZ (111) e_{22} strain near the interface versus change in thermal gradient

4.4   Summary

These results display the mechanical response determined at variations in thermal and mechanical loading conditions for early-cycled specimens. The relation between increases in thermal gradient and increase in stress gradient was determined in the YSZ inner region, strengthening some assumptions that a link can be made between increases in thermal gradient and alternative failure modes. The bond coat has shown the presence of inelastic behavior such as creep, which the magnitude of such behavior is often assumed during cyclic simulations. This has led to the further investigation of creep and is shown in Chapter 5 for aged specimens. The combination of early-cycled results and those of aged specimens in Chapter 5 provide the evolution of material behavior which can be used to create and validate TBC models which previously relied heavily on several assumptions similar transient responses.

71

CHAPTER 5
IN-SITU MECHANICAL RESPONSE OF AGED SPECIMENS

While the data taken from as-coated or early cycled specimens can provide a wealth of information, to fully close the loop between design criteria and eventual failure modes, studies must be done of the fatigue effects on the mechanical behavior. The phase composition and microstructure of each layer is known to change significantly over the life of a TBC. This, along with the large contributions from the TGO growth, changes the internal strains and how they respond to various loading conditions. To account for fatigue, samples were pre-aged to various stages of a lifespan which were used for experiments similar to the early cycled results presented in Chapter 4. These specimens serve to represent multiple stages of the coating lifespan and provide the information necessary to understand how the strain and stress profile evolves over thermal gradient and mechanical cycling.

Along with results from the bond coat and YSZ, the aged specimens provided valuable results on the TGO as well. The TGO layer in the as-coated specimens, with an estimated TGO thickness of 0.5 μm, proved difficult to acquire enough diffraction volume for strain measurements. These specimens, which were thermally aged, developed a TGO layer in each specimen to various thicknesses and corresponding residual growth stresses. With the increased thickness of the TGO in the aged samples, the diffraction volumes are sufficient enough to be measured despite their cylindrical geometry. TGO stresses and strains were measured throughout all testing, providing in-situ behavior of this layer which is considered critical in causing failure.

Similar experiments to the ones conducted on the as-coated specimens, described in Chapter 4, were conducted on the aged specimens. The similar testing consisted of single cycles of varying parameters, thermal gradient variation at high temperature, and tensile testing at various temperatures. The testing of the aged specimens at Argonne was done at a later time than the experiments on the early-cycled specimens. Therefore, improvements to the testing and experiment plan were made over the earlier testing. Most importantly, testing was done targeting the creep behavior of TBCs. This experiment was able to capture the transient response under constant loading at high temperature. This provided highly sought after creep measurements of the TGO, bond coat and YSZ within a fully coated specimen with no layer or material removal. The aged specimens also exhibited no noticeable changes in strain between the various cycles, allowing for the comparison of different loading conditions on in-cycle stresses. This cyclic comparison provides previously unseen in-cycle behavior which directly shows how both thermal gradient and mechanical loading can cause or limit different strain behavior such as creep.

5.1   Specimen Preparation

To simulate the TBC life duration at high temperature, specimens were pre-oxidized prior to testing. Specimens were aged to 154, 264, and 304 hours through isothermal aging at 1000 °C. The aging process was thermally cyclic as the specimens were removed from furnace every 24 hours and allowed to cool down to room temperature. Caps welded to

the ends of the tubular specimen restricted access of atmospheric air to the bare inner substrate, avoiding oxidation of the substrate. The 154 and 264 hour specimens were the same used in the early-cycled experiments while the 304 hour specimen was obtained from a newly coated batch of specimens.

5.2 XRD Measurement Parameters for Aged Specimen
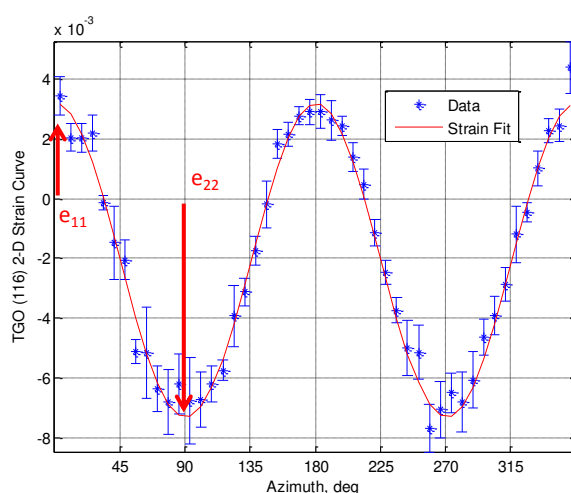
Figure 5.1: TGO α-Al$_2$O$_3$ (116) strain fit at room temperature

In assuring the achievement of TGO XRD measurements, the beam energy was increased from the prior 65 keV energy levels to 76 keVs. This not only provided easier penetration through the material but also lower 2θ angles. The lower diffraction angles with a decreased sample to detector distance to 1.4 meters permitted the measurements of a much larger amount of outer rings with only a negligible loss in radial position resolution for the inner rings. This allows the full ring measurements of lattice planes which

were previously unmeasured at d-spacing between 0.9 and 1.4 Å. Each measurement was taken at 1 second per frame with 5 frames. Window size was set at 30 μm width by 300 μm height. Scans were conducted from the YSZ surface into the sample with 14 steps of 30 μm. Including intensity scans for sample movements due to thermal expansion, time between first measurements of a scan was 4.5 minutes. Measurement devices used in the prior experiments were kept similar.
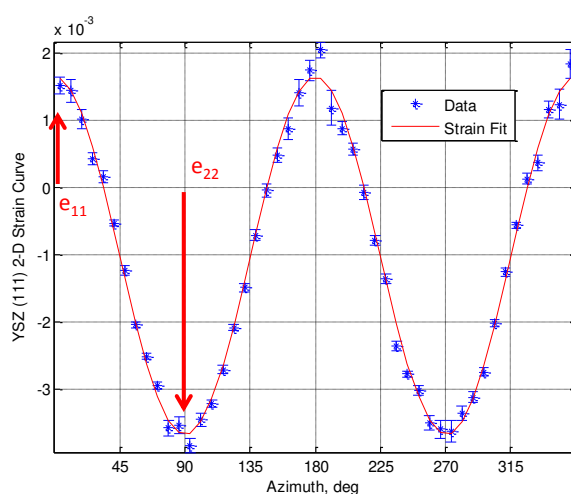
Figure 5.2: Top Coat t′-YSZ (111) strain fit at room temperature

For strain measurements, the γ-Ni (111) and β-NiAl (110) planes were used for the bond coat. The (111) plane was used for the t'-YSZ phase and the (116) plane was used for α-Al$_2$O$_3$ TGO. The strain fits for these planes are shown in Figures 5.1 through 5.4. These plots display the strain around the azimuth angle determined from the radial deviation of the diffraction ring. The TGO in the specimen which was aged to 304 hours was very well developed and gave good fits despite it very low relative intensity to that of the YSZ which the beam has to penetrate through. The α-Al$_2$O$_3$ (116) peak serves

as best peak for strain fitting. This peak provides the greatest intensity while not being overlapped by a neighboring bond coat or YSZ peak.
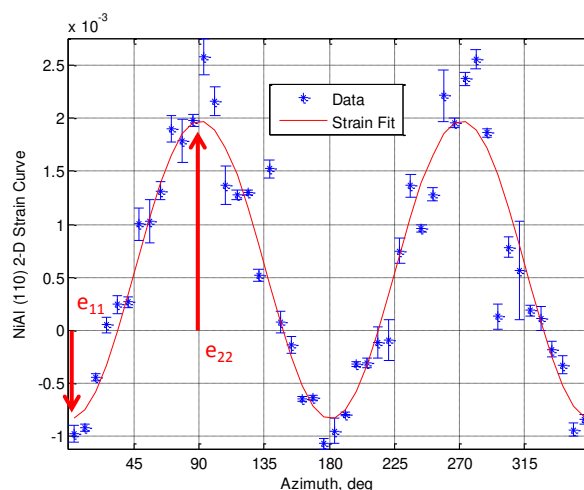
Figure 5.3: Bond coat β-NiAl (110) strain fit at room temperature

The t'-YSZ applied by EB-PVD, is known to be highly textured. This affects the ability to fit accurate 2-D strain curves. The t'-YSZ (111) plane displays minimal texturing and is therefore used for the strain analysis. The strain fit for this plane is shown in Figures 5.2. The bond coat for the specimen aged for 304 hours was found to have larger grain size and hence had increased spotting in the diffraction rings, making strain fits more difficult.

The β-NiAl (100) plane is the softest direction and was preferred for its larger radial shifts. The spotted diffraction rings proved difficult for achieving good strain fits for the (111) plane. The NiAl (110) plane provided the benefit of neighboring the most prominent γ-Ni peak. Fitting the two peaks simultaneously for both γ-Ni (111) and β-NiAl (110) created sufficient fits to develop trends throughout cycling.
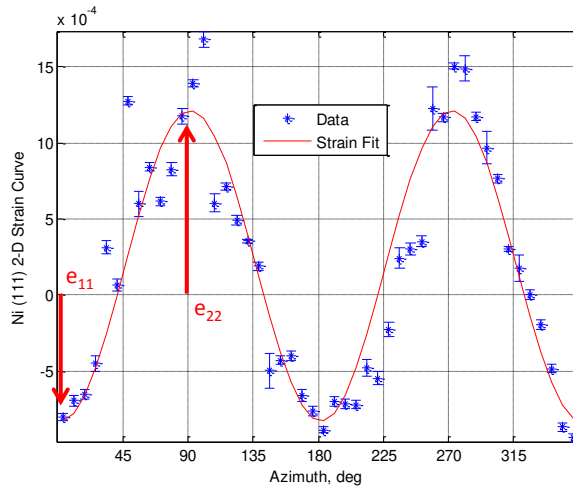
Figure 5.4: Bond coat γ-Ni (111) strain fit at room temperature

5.3 Single Flight Cycles for Specimen Aged for 304 Hours

Since the specimen aged for 304 hours gave very accurate strain fits and contained the most developed TGO layer, it is used to further investigate the cycle conditions and their effects on stress. For this specimen, data was collected during the various stages of a single cycle for 9 individual cycles which consisted of combinations of 32, 64, and 128 MPa nominally applied loads and 30, 50, and 75% of maximum thermal gradients. Similar to before, flowrate and applied mechanical loads were kept constant throughout the cycle. From the initial experiment run with the early-cycled specimens, it was determined that 20 minute holds at high temperature was sufficient for strains to settle. Therefore, the hold period at high temperature was reduced from the 40 minutes used with early-cycled specimens to 20 minutes for time saving purposes. Ramp-up and ramp-down periods were consistent with early-cycle experiments at a 20 minute duration while high temperatures

77

of 1000 °C were also kept consistent. Figures 5.5 through 5.7 display the strains measured in each layer at the interface throughout a cycle with conditions of 64 MPa mechanically applied load and 75% thermal gradient. These strains, among the other cycles, are then converted to stress in the subsequent discussion.

Figure 5.5: TGO strain measurements for single cycle with 64 MPa mechanical load and 75% of maximum thermal gradient

Figure 5.5 displays the TGO α-Al$_2$O$_3$ in-plane (e_{22}) and out-of-plane (e_{22}) strains throughout a cycle. This displays a very large compressive strain with a magnitude of about -7e-3. As the temperature is increased to 1000 °C, the strain reduces to near zero as stress relaxation corresponds to the aging of the specimen at the same temperature. The t'-YSZ strain is displayed in Figure 5.6. The YSZ displays a compressive strain at room temperature at the interface which is nearly half of the strain in the TGO. This is consistent in strain direction of early-cycled specimens with a magnitude which is significantly larger. EB-PVD coatings are known to be fairly compliant. This means that they can endure a larger macro-strain without exhibiting large stresses. However, lattice strains within the grains measured from XRD translate directly to stress. Both of the

78

prominent bond coat phases are displayed in Figure 5.7. It can be seen that there is some loss in accuracy for bond coat measurements of the aged specimen at high temperature.

Figure 5.6: YSZ strain measurements for single cycle with 64 MPa mechanical load and 75% of maximum thermal gradient

To display the effects which both thermal gradient and mechanical loads have on high temperature stresses, cycles are compared where one of the loading conditions is held constant. Shown in Figures 5.8 - 5.10 are single cycle results comparing the effects from varying flowrate representing the different thermal gradients. Each plot compares single cycles with a common applied mechanical load and variations in thermal gradient. These display the in-plane stresses σ_{22} for the TGO, YSZ, and bond coat NiAl which were calculated from (116), (111), and (110) planes respectively. The consistency which occurs with the room temperature stress for common mechanical loads shown in each of the plots, indicates both minimal effects from cycling, which were conducted in no specific order, and accuracy in the measurements. With the early-cycled specimens (under 15 cycles) described in Chapter 4, large strain evolution was seen due to cycling, making determination of loading effects infeasible.

79
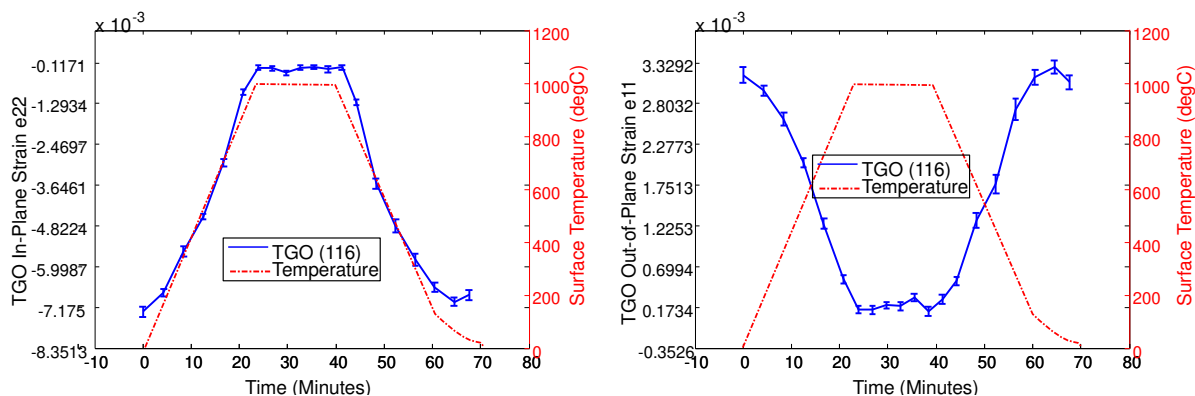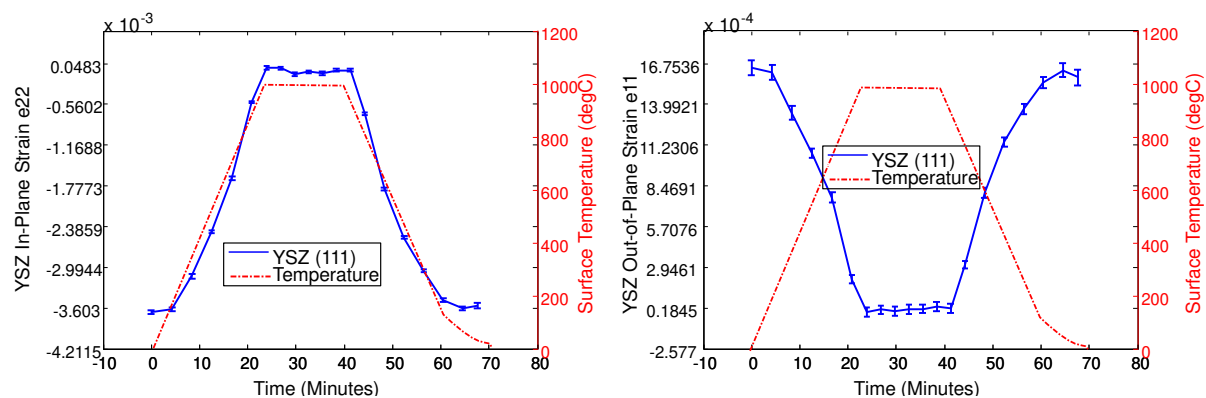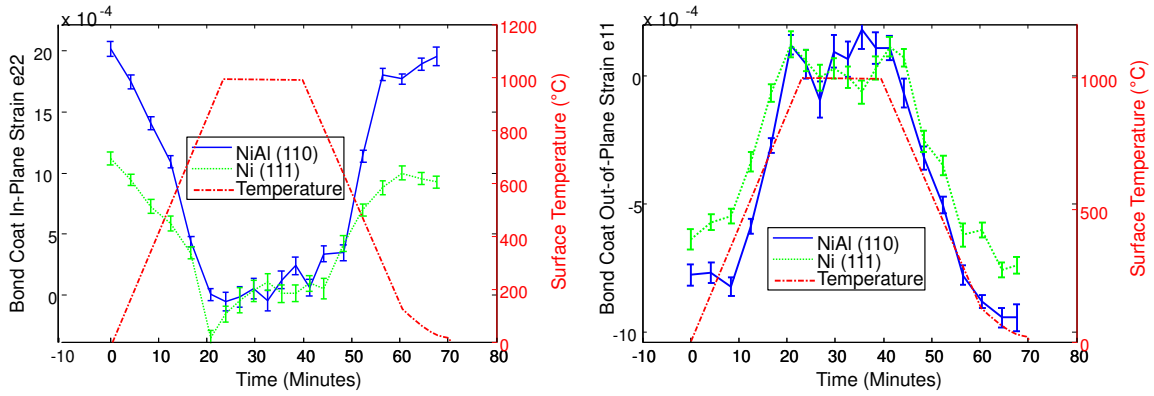
Figure 5.7: Bond coat strain measurements for single cycle with 64 MPa mechanical load and 75% of maximum thermal gradient

The thermal gradient effects during cycling for the TGO are displayed in Figure 5.8. From left to right, the plots show thermal gradient comparisons under 32, 64, and 128 MPa loads. In general, the TGO displays a very large compressive residual stress at room temperature in the range of 3-4 GPa. Of particular importance, the TGO shows the ability to exhibit tensile stresses at high temperature with a direct dependence on both thermal gradients and mechanical loads. This presents quantitative evidence that applied tensile loads from rotating blades can move the TGO stress into the tensile region at high temperature and agrees with results observed in prior in-situ TMF studies with no thermal gradient [20]. This insight is especially valuable in terms of damage as tensile stresses promote crack initiation in this critical layer. This has been shown in ex-situ TMF studies that the presence of tensile loads the TBC life was limited by cracking into the bond coat [91]. The simulations from this study suggested that these applied mechanical loads could cause tensile stresses in the TGO which could lead to this form of failure. Countering this effect, it is seen that with increased thermal gradient, a significant

80

compressive change occurs. This shows the ability of thermal gradients to bring the TGO stress back into the compressive region even at high applied loads. At higher loads and lower thermal gradients, the TGO displays a transient relaxation response from a tensile stress which is likely due to creep in the TGO itself. With the increased thermal gradient, this effect is then limited. This is due primarily to the reduced stress in the TGO from the thermal expansion effects and temperature reduction and is also likely assisted by the reduced creep at lower temperatures. Nearly every cycle measured, follows some trend based on variation in mechanical load or thermal gradient. However, one anomaly does occur with the 128 MPa load and 30% flowrate. It would be expected for this cycle to exhibit a larger tensile stress at high temperature to follow the trends which occur in the rest of the cycles.
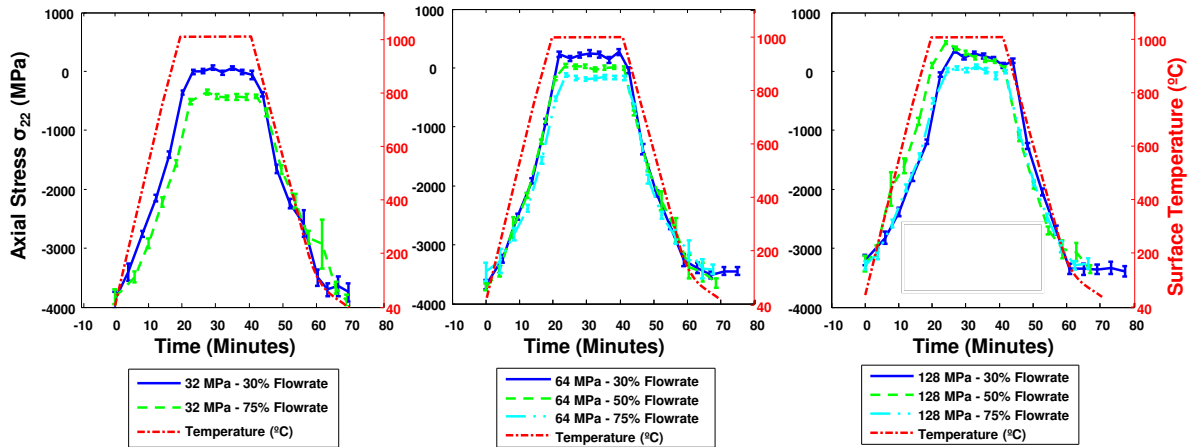
Figure 5.8: Cycle comparison of thermal gradient during various mechanical loads for TGO in specimen aged for 304 hours

The thermal gradient effects during cycling for the YSZ are displayed in Figure 5.9. As this is displaying the YSZ stress at the interface, trends are seen that are similar to

the TGO. At room temperature, the YSZ displays a compressive stress near 1 GPa. As is shown in the strain results, the strain in the YSZ at the interface is half the TGO strain. Therefore, despite the strain tolerance of EB-PVD YSZ coatings, there still exists a fairly large compressive stress at the interface. This can be explained by the higher density near the interface, which exists in these columnar structured coatings. As the temperature is increased to 1000 °C, the YSZ stress follows the same trend of moving towards zero. It also displays a similar dependence on loading conditions for the ability to transition into the tensile region. The YSZ also displays a similar relaxation from tensile stresses under high loads.
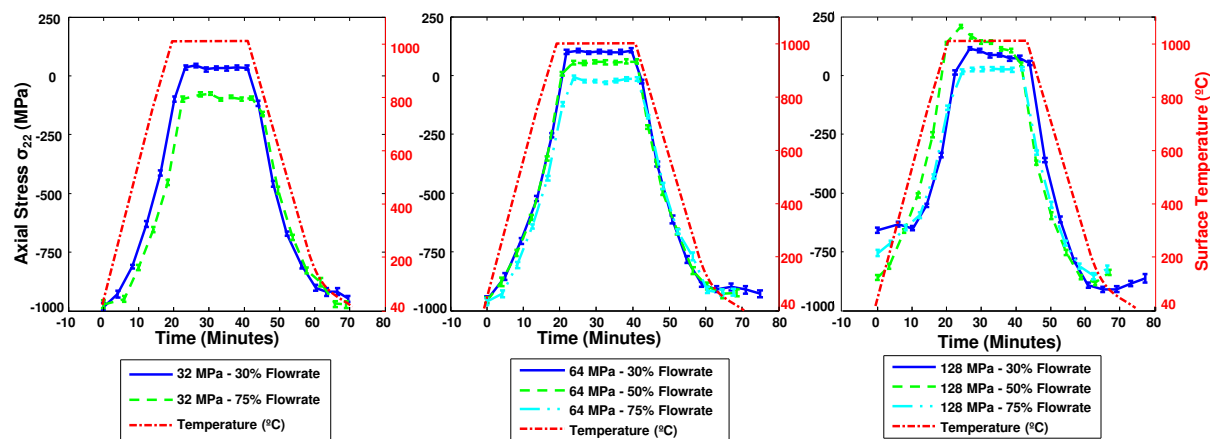
Figure 5.9: Cycle comparison of thermal gradient during various mechanical loads for YSZ in specimen aged for 304 hours

Displayed in Figure 5.10 is the thermal gradient comparison for the bond coat NiAl phase. In contrast to the early-cycled specimens, the grain size increased significantly. Therefore, the diffraction rings were fairly spotted. This resulted in a decreased accuracy in fitting strain and stress. It can be concluded from this that the bond coat still maintains

82

a very high tensile stress at room temperature at around 600 MPa. The accuracy of these measurements are especially degraded when it relaxes to zero at high temperature. However, there appears to be a trend under high mechanical load at 1000 °C. The bond coat displays a transient stress response as it becomes increasingly tensile. This appears to be more prominent under higher thermal gradients. This could be explained by the lower temperatures occurring in the bond coat, resulting in a greater elastic response.
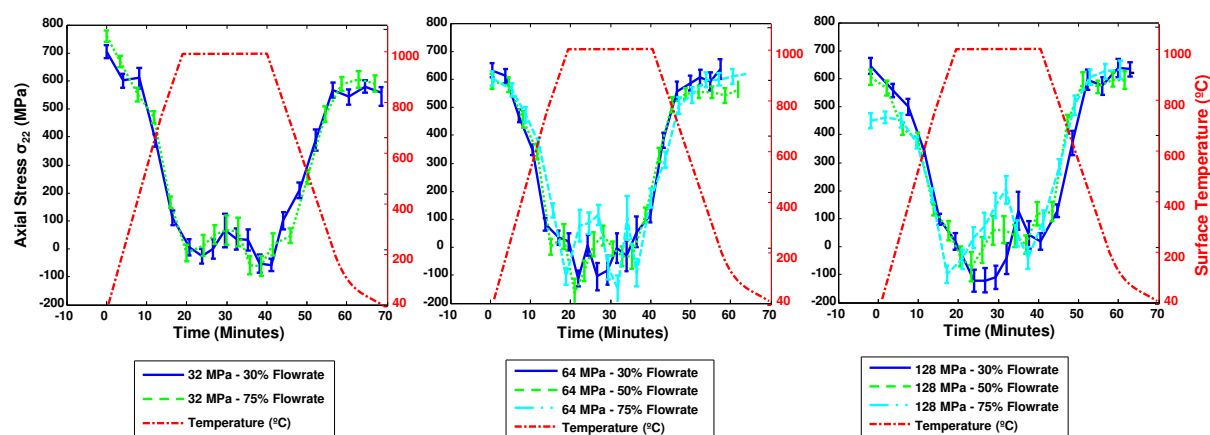
Figure 5.10: Cycle comparison of thermal gradient during various mechanical loads for bond coat NiAl in specimen aged for 304 hours

Similar to the thermal gradient comparison, the same cycles are compared for different mechanical loads while under selected thermal gradients. This highlights the extent of the effect that mechanical loads have on high temperature stresses in comparison to the thermal gradient effects. Shown in Figure 5.11 are the effect of mechanical loads on the TGO stresses. This displays that a larger response to mechanical loads generally occurs with higher thermal gradients. From the 75% flowrate plot, corresponding to high thermal gradient, it can be seen that the increase from 32 to 128 MPa creates a tensile

83

shift of roughly 500 MPa in the TGO. This suggests the TGO consists of a primarily elastic response under higher thermal gradients. The lower temperature, along with the compressive state maintained throughout all three mechanical loads, is consistent with this reasoning. This quantified stress relaxation in the TGO is within range of results from simulations on similar specimens under thermal gradients [6]. These simulations suggest that under an applied axial stress of 100 MPa, stress relief in the TGO can be seen of about 390 MPa. Shown in Figure 5.12, is the mechanical load effect on cycling for the YSZ. Similar to that of the TGO, the YSZ displays its largest response to applied load under the 75% flowrate. This shows that the increase from 32 to 128 MPa creates a tensile shift of 250 MPa in the YSZ.
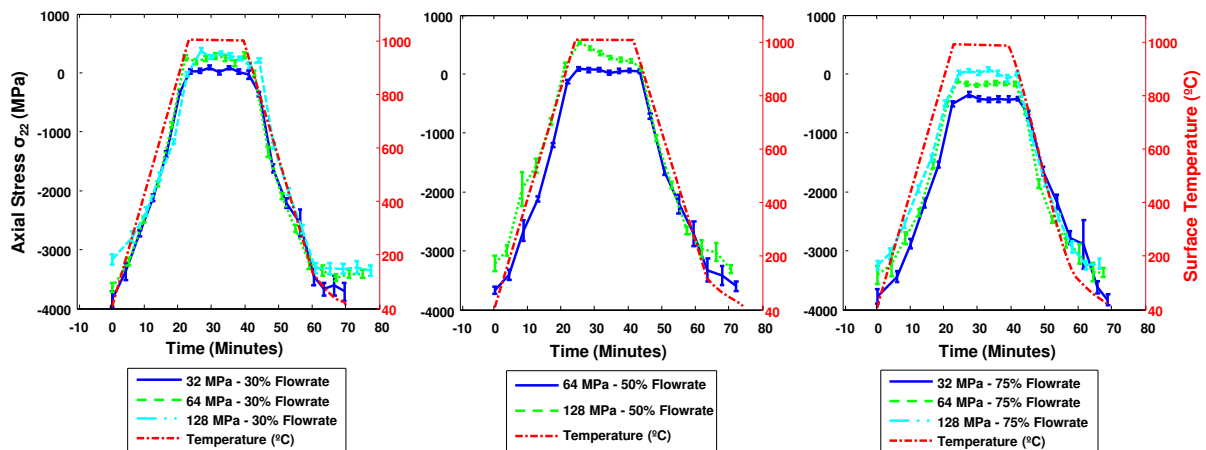
Figure 5.11: Cycle comparison of mechanical load during various thermal gradients for TGO in specimen aged for 304 hours

84
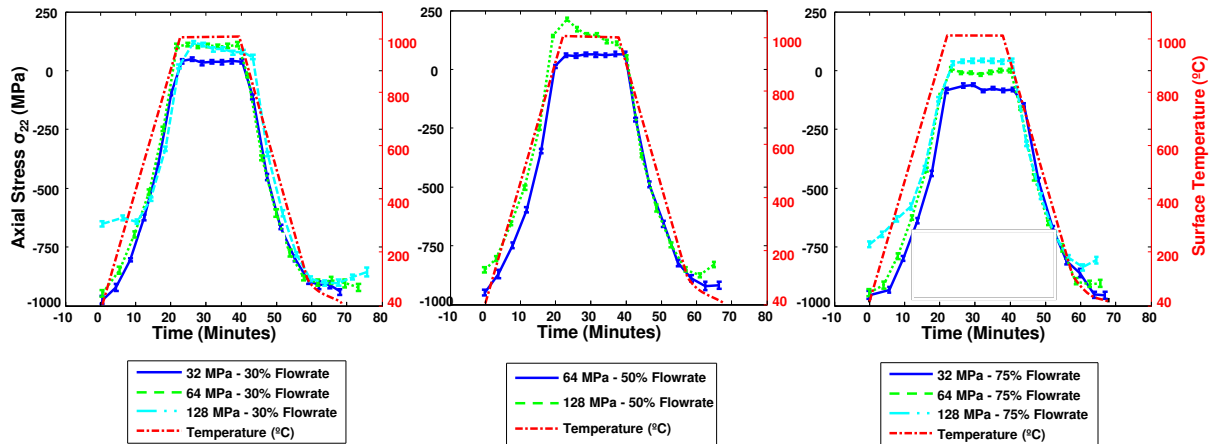
Figure 5.12: Cycle comparison of mechanical load during various thermal gradients for YSZ in specimen aged for 304 hours

5.4 Strain Effects from Thermal Gradients Variation in Specimen Aged for 304 Hours

Experiment tests, isolating the effects of thermal gradient variation, were conducted under similar conditions described in Chapter 4. Here, the entire specimen was ramped up to 1000 °C and allowed to settle to steady state. Then the flow rate was increased slowly from 0 to 100% as the internal strains were monitored throughout the duration. As with the early-cycled specimens, the bond coat displayed no variation with applied thermal gradient due to the creep response at this temperature. The aged specimen displays a very large variation during increases in thermal gradient.

Displayed in Figure 5.13 is the TGO stress versus thermal gradient. This shows a 700 MPa compressive shift as the thermal gradient reaches 100%. This further highlights the ability of the thermal gradient to keep the TGO in compression at high temperature. As

this thermal gradient reaches higher values, the stress reaches compressive values which may contribute to buckling due to creep at high temperature. Another point of interest here is the stress which occurs under zero thermal gradient. This value represents the growth stress that developed during the aging process at the same temperature. It can be seen here, as well as in cycling results, that the TGO exhibits near zero stress under zero thermal gradients and mechanical loads. Surprisingly, this suggests that any stresses developed due to TGO growth during aging may have been relieved due to buckling. Figure 5.14 displays the YSZ stress versus variation in thermal gradient. This displays a smaller compressive shift with a value of about 190 MPa in compression at 100% thermal gradient.
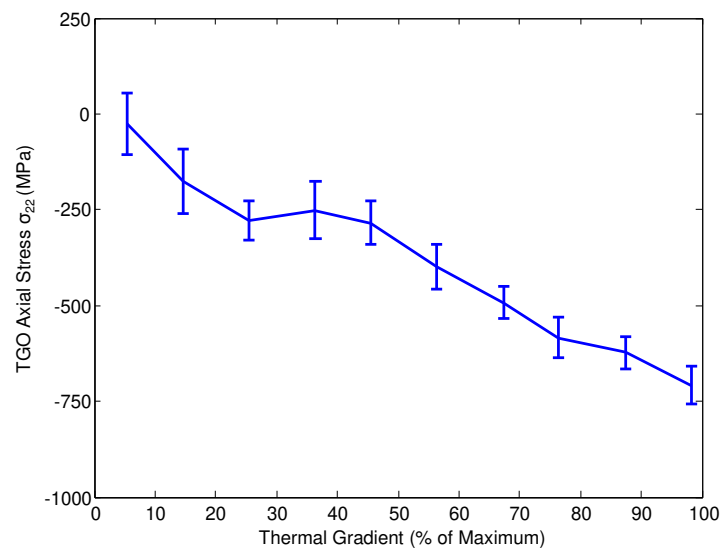
Figure 5.13: TGO axial stress response to variation in thermal gradient in specimen aged for 304 hours
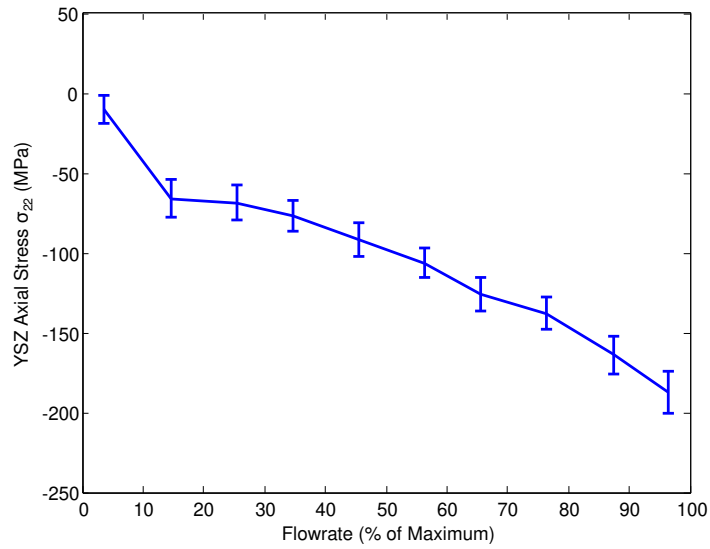
Figure 5.14: YSZ axial stress response to variation in thermal gradient in specimen aged for304 hours

5.5 Strain Response to Tensile Tests at Temperature with Specimen Aged for 304 Hours

Tensile test were done at various temperatures as described for the early-cycle specimen in Chapter 4 where the applied tensile stress was ramped up under constant temperatures while the strains are monitored. This was consistent with the early cycled specimen with temperatures of room temperature, 200, 400, 600, 800 and 1000 ℃. However, the applied mechanical loads were increased in magnitude to vary between 0, 48, 64, 96, and 128 MPa. Displayed in Figure 5.15 are the strain results for the TGO (116). Here, the applied nominal stress in the axial direction is on the y-axis and the resulting strain response is on the x-axis.
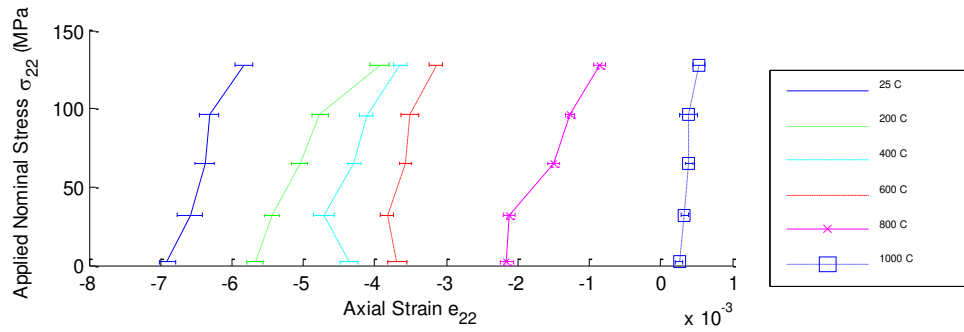
Figure 5.15: Tensile tests for TGO in specimen aged for 304 hours
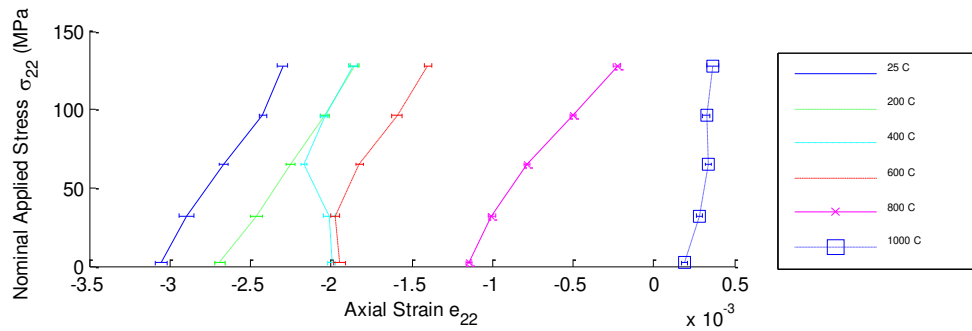
Figure 5.16: Tensile tests for YSZ in specimen aged for 304 hours

Each strain curve was obtained from experiments at a different temperature where the temperature increases from left to right due to the relaxing compressive stress. The slope appears to generally increase between room temperature and 800 °C. This seems to be especially true for the curve specifically at 800 °C. At this temperature, it is expected that the substrate will have a lower elastic modulus than it did at room temperature. Therefore, the total displacement of the sample will increase. This results in a higher strain in the TGO. The slope at 1000 °C then suddenly increases, displaying that the

TGO has nearly zero elastic response to the applied mechanical load. Since the sample displacement will not decrease during a shift to 1000 ℃ and will most certainly increase, it can be concluded that the total strain response of the TGO is higher at this temperature. As XRD only measures the elastic strain, these results show that inelastic behavior dominates the TGO response at 1000 ℃.
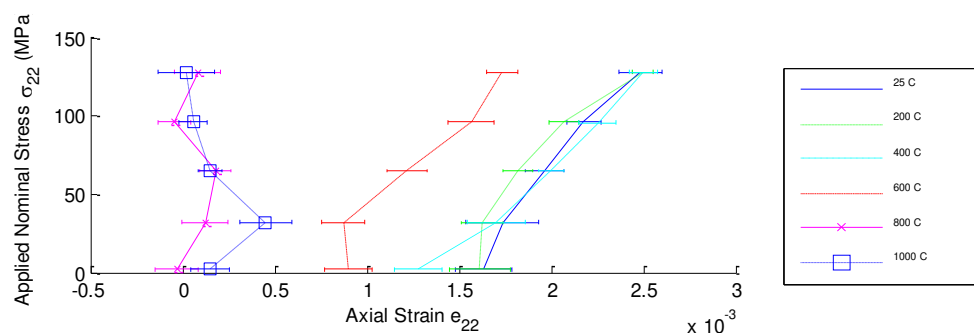
Figure 5.17: Tensile tests for bond coat NiAl in specimen aged for 304 hours

Figure 5.16 displays that the YSZ response maintains a constant slope during low to mid-range temperatures with a slight increase at 800 ℃. There is an exception at 400 ℃ where the data does not follow that trend. This response shows that the YSZ had a lower residual strain as the load was decreased from the previous temperature of 200 ℃. After increasing the applied load, it then converges to the common slope. As was seen with the TGO, the YSZ also displays near zero elastic strain response to applied load at 1000 ℃.

The bond coat NiAl response to mechanical loads is displayed in Figure 5.16. Here, the strain responses move from right to left with increasing temperature as the residual

89

room temperature strain is tensile in the bond coat. The bond coat displays a constant slope up to only 600 °C. At 800 °C and above, the response tends to be purely inelastic. As explained for the early cycled specimen, a ductile to brittle transition has been associated with grain boundary creep at temperatures as low as 600 °C [63]. This is consistent with results displayed for the early cycled specimen and also highlights the need for monitoring of bond coat creep.

5.6   Creep Results for Specimen Aged for 304 Hours

Creep studies are generally done by measuring the transient strain as a constant stress is applied to bulk materials. This makes it difficult to determine creep behavior of coatings due to the problems associated with determining the stress and strain response of the individual layers. XRD provides the ability to take these measurements using the monitoring of elastic strain in the individual phases in the coating layers. As creep creates a transient plastic response, it can be monitored provided that measurements are quick enough to capture the response. These previous tests have highlighted and proved the existence of creep behavior in the layers under certain loading conditions but have not provided quick enough measurements to capture the response in detail due to the time required for scanning through the thickness. During all previous testing, measurements were taken using scans through the thickness of the coating with either 10 or 14 steps.

Experiments were conducted where a single location in the bond coat near the interface was monitored under a nearly instantaneous applied load of 128 MPa. The load was

held constant for a duration of 12 minutes while rapid single location measurements were taken. Actual location cannot be given with complete certainty due to the possibility of inconsistent sample movement during reloading. The measurement location had to be predetermined under a similar load prior to the creep test. Although, the diffraction intensity achieved by the TGO suggests it is very near the interface. This single location measurement, with use of high-energy x-rays, provides the ability to take these measurements at a rate sufficient enough to monitor the transient response in the layers. This was done at temperatures of 800 °C and 1000 °C.
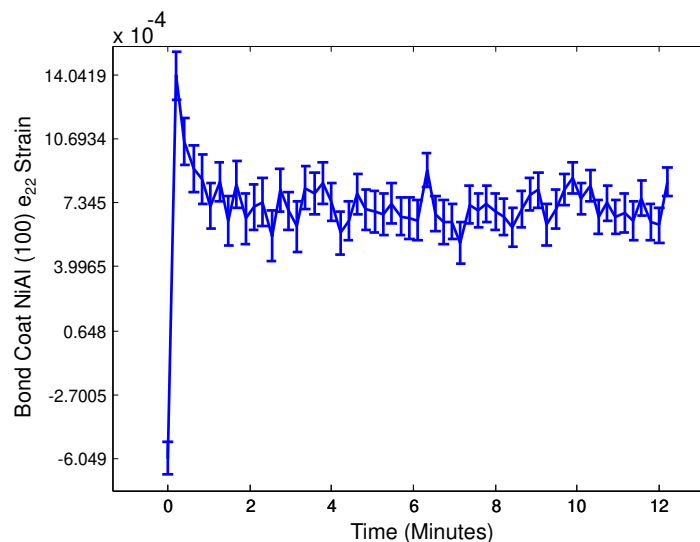
Figure 5.18: Creep response of bond coat to a constant nominally applied stress of 128 MPa

Displayed in Figure 5.18 is the NiAl (100) response to constant load at 800 °C. It can be seen that relaxation to steady state occurs less than 2 minutes, making standard scanning measurements unable to achieve this. The measurement technology and high-energies provided at the synchrotron 1-ID beamline is therefore required to take

measurements at such a speed. At 800 °C, short term relaxation due to creep only exists in the bond coat. This is displayed in Figure 5.19 where the YSZ strain is plotted during the same test. This shows that no transient behavior exists in substrate at these 800 °C as the substrate largely dictates the total displacement of the sample.
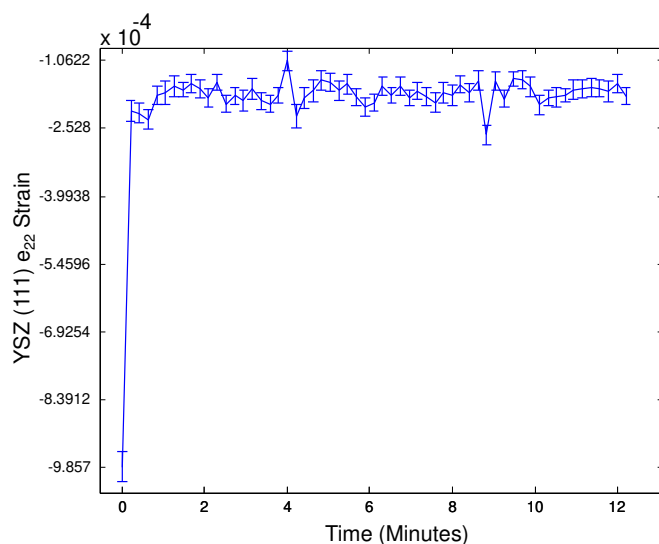
Figure 5.19: YSZ response to a constant nominally applied stress of 128 MPa at 800 °C

During thermal expansion in coatings, the difference between total strain of the specimen and the thermal strain in the particular layer create stress mismatch between the substrate and different coating layers. With coatings such as these, the total strain is largely dominated by the substrate. This can create a situation such as this where the total strain of the sample remains constant and the stress is relieved over time in a layer of the coating. This behavior of stress being relieved under constant total strain (elastic + plastic) is referred to as stress relaxation and is different from actual creep. Creep is the transient conversion of elastic to plastic strain under constant stress while stress relaxation is the transient conversion under constant strain. However, both behaviors

consist of transient plastic strain under the same mechanisms. Therefore, it is common to use the terminology of creep for both. The stress relaxation is modeled by the Norton creep equation:

$$\varepsilon_p = A\sigma^n \exp(-Q/RT) \tag{5.1}$$

where ε_p is the strain rate, A is a grain size dependent material constant, Q is the activation energy for creep, and R is the gas constant. For this experiment, the total strain is assumed constant. Equation 5.2 states the relationship between total, elastic and plastic strain rate. The purely elastic strain rate measured using XRD will equal the negative of the plastic strain rate. This can then be used to implement Norton's equation to model stress relaxation [89]. Ideally, more temperature variations are conducted to accurately determine the activation energies. Due to time constraints, only the two temperatures were conducted. The three constants were then fit to the strain rate versus stress data for the primary regime of creep.

$$\dot{\varepsilon}_t = \dot{\varepsilon}_p + \dot{\varepsilon}_e \tag{5.2}$$

Shown in Figure 5.20 is the NiAl (110) transient elastic strain after loading and the corresponding fit of the creep model. Noise in the data curve can easily be amplified, especially during the derivative calculation for the strain rate, so the data for both strain and stress were filtered twice each using a moving average low pass filter. After smoothing of the data, the resulting curve followed the same trend as the data shown in the plots

minus the sharp variations. At 800 ℃, transient strain over the 12 minute measurement was only observed in the bond coat.
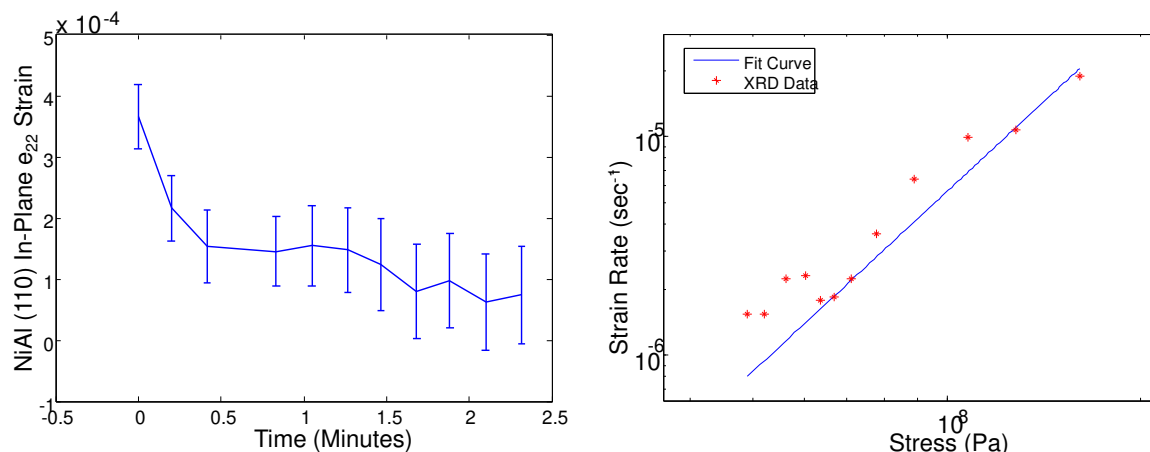
Figure 5.20: Creep measurement for NiAl at 800 ℃: a) raw strain measurements before filtering and b) model fit to strain rate vs. stress

At 1000 ℃, creep was also seen in both the TGO and YSZ. However, at 1000 ℃, the plastic behavior in the bond coat was too prominent to achieve a strain trend for creep measurement. Shown in Figures 5.21 and 5.22 are the creep measurements at 1000 ℃ for the TGO and YSZ respectively.

The creep parameters which were determined from this study are displayed in Table 5.6. The stress exponents (n) for the bond coat, shown here, is in the range of what is seen in other studies [12, 85]. However, the exponent for the TGO is much higher than what has been seen in literature. One study, which was done on oxidized bulk bond coat samples, measured an exponent of 1.7 [28]. Generally, creep parameters for TBCs have been determined from isolating one of the layers. These results differ in that they were obtained from in-situ studies of fully coated specimens with a substrate and YSZ

94

layer with no material removal. Having a YSZ layer is especially important for the TGO creep as the EB-PVD columnar structure can change the microstructure of the oxide. The results from this study provide modeled creep behavior which is largely unknown for these ceramic coatings. As creep is shown to be a significant factor in the stress response, studies such as these are highly valued for the simulation community attempting to develop models predicting failure.
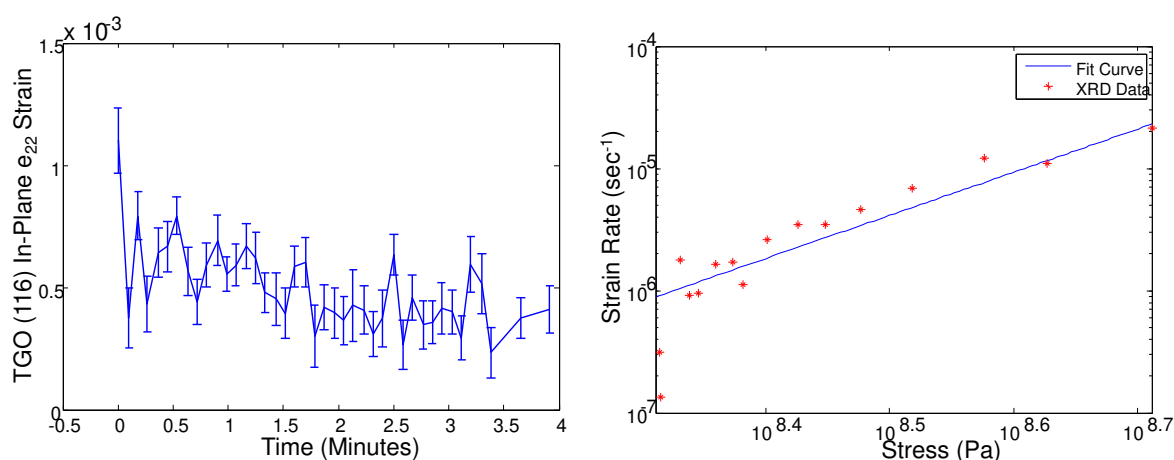
Figure 5.21: Creep measurement for TGO at 1000 °C: a) raw strain measurements before filtering and b) model fit to strain rate vs. stress

Table 5.1: Creep constants for NiAl, TGO and YSZ

|	A (s^{-1}*Pa^{-n})exp(- Q/RT)	n
NiAl (800 °C)	8e-28	2.73
TGO (1000 °C)	4e-36	3.53
YSZ (1000 °C)	1e-28	2.80
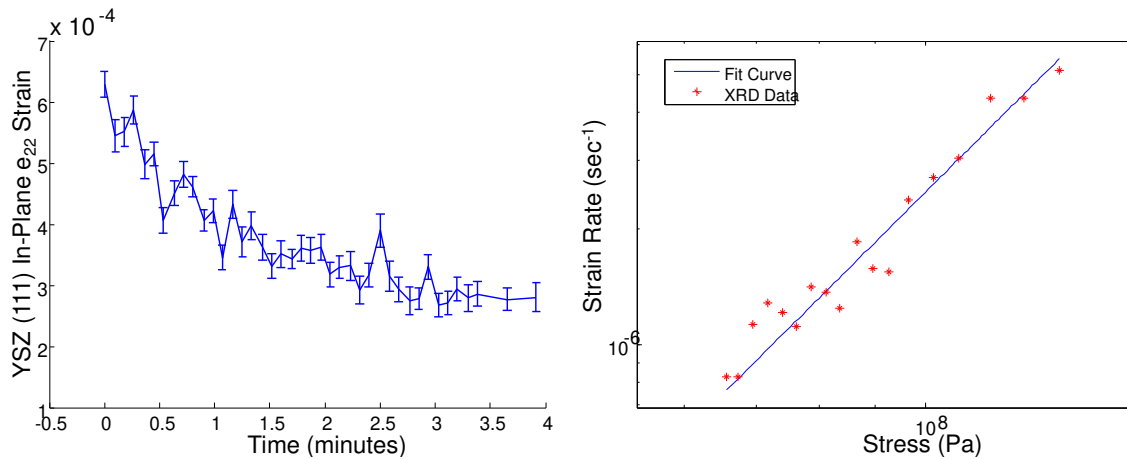
Figure 5.22: Creep measurement for YSZ at 1000 ℃: a) raw strain measurements before filtering and b) model fit to strain rate vs. stress

5.7 Single Flight Cycles for Aged Specimens

The strain calculated for the specimens of different ages are used to display the aging effects of the specimens. This represents how the strain in the various layers varies over the life of a TBC. The microstructure of each layer is known to change significantly over the life of a TBC. These effects, along with contributions from the growth of a TGO layer change the internal strains and how they respond to various loading conditions. Displayed in Figures 5.23 through 5.26 is the comparison of the strains for each specimen during a single cycle. The cycle shown was conducted under 64 MPa mechanical load and 75% thermal gradient. The specimen which was aged for 304 hours was obtained from a different manufactured batch and has a differing history from the other two specimens. The two younger specimens were also cycled during the experiments for the early cycle investigation.

Figures 5.23 and 5.24 display the strain measured from the two bond coat phases. From the comparison of the two younger specimens, it can be seen that the strain reduces significantly over aging. This is interesting as the high temperature strains remain constant. This suggests that creep may play a more prominent role in the aged specimens, allowing the strains to remain relaxed during cool-down periods. Figure 5.25 displays the strains for the TGO. This shows little variation during the cycle. However, strains calculated in the younger specimens do not display high accuracy in the TGO strain fits and may not accurately represent trends. Figure 5.26 displays the YSZ strain. This displays that with aging, the strain shift between room temperature and high temperature reduces over aging.
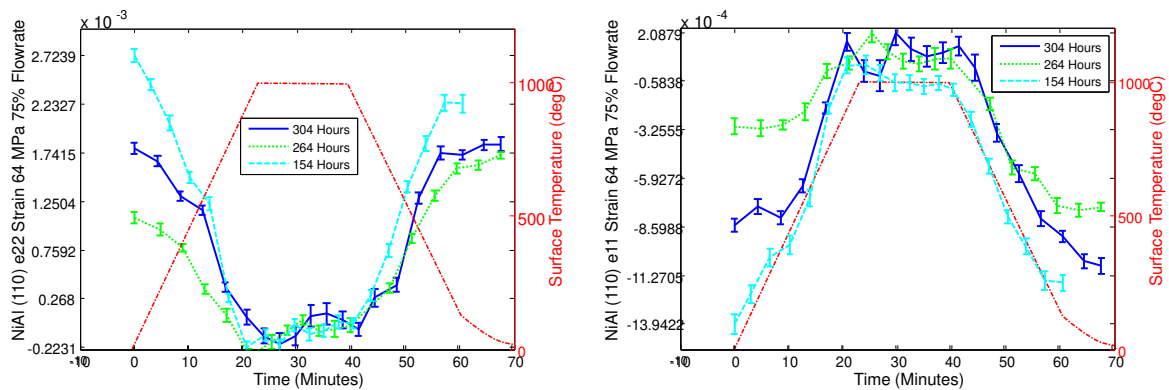
Figure 5.23: Aged comparison of NiAl (110) strain for 64 MPa and 75% flowrate
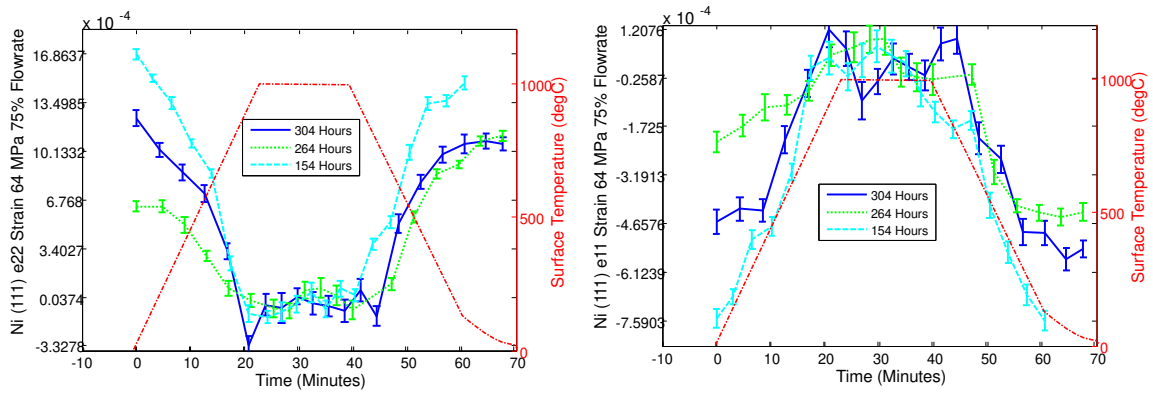
Figure 5.24: Aged comparison of Ni (111) strain for 64 MPa and 75% flowrate
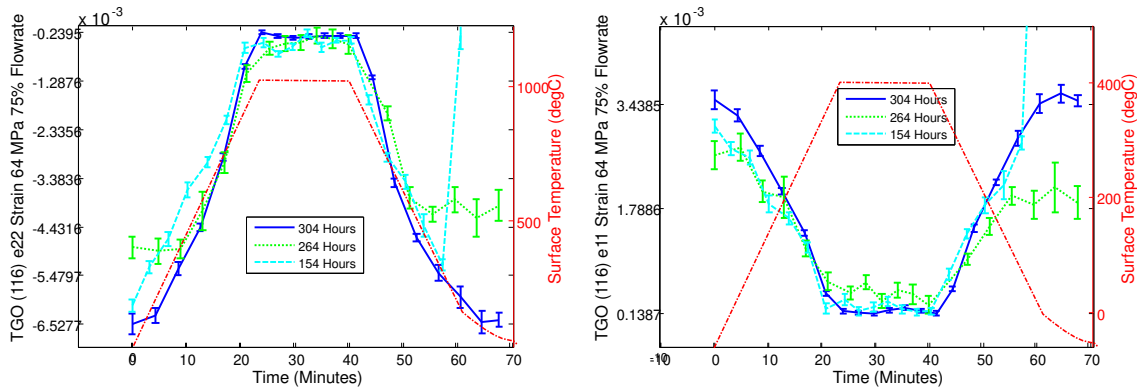
Figure 5.25: Aged comparison of TGO (116) strain for 64 MPa and 75% flowrate
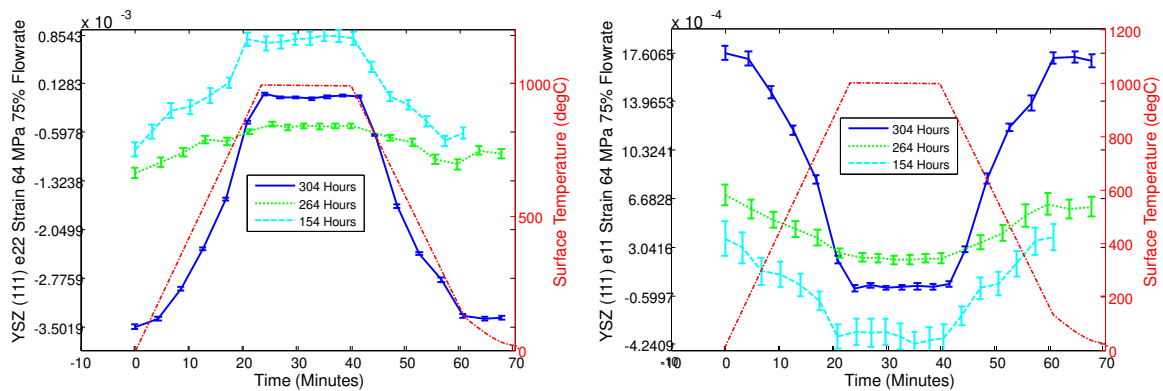
Figure 5.26: Aged comparison of YSZ (111) strain for 64 MPa and 75% flowrate

98

CHAPTER 6
CONCLUSIONS

The results from these experiments provide previously unseen mechanical behavior of TBCs under extreme conditions. Findings from this study will contribute to making significant steps towards extending the life span of TBCs by providing material behavior which can be used to validate models and close the design loop in creating more durable coatings by adjusting the processing parameters as well as through more innovation in enhancing coating materials. Having knowledge of how internal strain and stress through the different layers responds at high temperature under thermal gradient and mechanical loads provides valuable knowledge for developing the link between loading conditions and failure driving stresses. TBCs are known to have large residual stresses, especially at the interface. This work has successfully monitored these stresses and their dependence on variations in thermal gradients and mechanical loads. Specimens were tested in their early cycled stage as well as their pre-aged stages. This worked to simulate the response of TBCs through various stages of a TBC lifespan. Through cycling under varying conditions, it has been shown that mechanical loads at 1000 °C can drive the TGO and YSZ into tension while increases in the subjected thermal gradient was largely effective in moving the two layers back into compression. Experiments varying the thermal gradient have displayed a relation between increases in thermal gradient and increase in stress gradient in the YSZ inner region, strengthening the assumption that a link can be made between thermal gradient and different failure modes. Tensile tests at elevated temperature have shown that the strain response becomes inelastic in each of the layers at higher temperatures. This highlights the extent of creep response in TBCs at

different temperatures. Experiments targeting this transient strain behavior successfully captured and quantified this creep behavior in the bond coat, TGO, and YSZ layers. The stress and strain behavior captured here can be used for developing TBC models for the purpose of predicting failure. These models, which are used for simulating damage causing stresses and crack propagation, rely heavily on high temperature material models which are difficult to validate. These results provide measured material models such as creep as well as validating stresses which are highly sought after in the TBC community.

The work conducted here developed an innovative setup which can monitor in-situ strain and stress through the thickness of multi-layer coatings under thermal gradient and mechanical loads. Subjecting high temperature coatings to environments representative of operating conditions is a very important factor in experiments investigating the mechanical behavior of these coatings. During operation, TBCs are under extreme temperatures with a large temperature drop over the coating with applied mechanical loads due to centrifugal loads. Therefore, applying thermal and mechanical loading is critical to the understanding of material behavior at high temperature. The methods developed here create the ability to apply these conditions while measuring in-situ strains using high-energy XRD. An infrared enclosure heater was used to maintain temperatures at or above 1000 °C while subjecting the inner substrate surface to ambient air cooling. This was successful in creating temperature drops of 150 °C across the 240 μm thick YSZ layer.

The heater was designed with the requirement that diffraction measurements could be obtained during loading. An exit window created in the heater wall allowed access to

XRD measurements. This was made feasible by the very low diffraction angles only seen from high-energy x-rays in the range of 65-86 keV. XRD techniques were developed for monitoring strain and stress in the internal layers of a coated cylindrical specimen. Using a 30 μm window width and step size, measurements scanned into the layers tangentially to the specimen. Phases in each of the layers were successfully distinguished from each other for the purpose of strain analysis. The material in the bond coat displayed a deviation from the in-plane equibiaxial state of stress expected for thin coatings due to the cylindrical nature of the coating and internal position of the bond coat. A method was developed which exploits the anisotropic cubic structure of the NiAl phase in the bond coat. By equating the stresses calculated from multiple lattice planes, the unmeasured strain direction can be directly solved for. By comparing the cubic lattice constant for the different planes, it has been shown that a deviatoric strain free lattice spacing can be measured. By combining the equating of stress and the strain free determination, deviatoric strain measurements can be taken on internal volumes which exhibit a triaxial state of stress. This method can very valuable for synchrotron x-ray diffraction measurements which have the capability to measure internal strains.

The developed experimental techniques can be used to further investigate different TBC coatings. As the requirements of these coatings continues to progress, the need for techniques to monitor strains under extreme conditions become increasingly valuable. Continuing studies using these new measurement techniques, can lead to significant advances in performance and durability of these coatings.

LIST OF REFERENCES

[1] H. Aleksanoglu, A. Scholz, M. Oechsner, C. Berger, M. Rudolphi, M. Schütze, and W. Stamm. Determining a critical strain for APS thermal barrier coatings under service relevant loading conditions. *International Journal of Fatigue*, 2011.

[2] M. Ali, S. Nusier, and G. Newaz. Creep effects on early damage initiation in a TBC system. *Journal of Materials Science*, 39(10):3383–3390, 2004.

[3] J. Almer and S. Stock. Internal strains and stresses measured in cortical bone via high-energy x-ray diffraction. *Journal of Structural Biology*, 152:14–27, 2005.

[4] M. Bäker, J. Rösler, and G. Heinze. A parametric study of the stress state of thermal barrier coatings part II: cooling stresses. *Acta Materialia*, 53(2):469 – 476, 2005.

[5] D. Balint and J. Hutchinson. An analytical model of rumpling in thermal barrier coatings. *Journal of the Mechanics and Physics of Solids*, 53:949–793, 2005.

[6] M. Bartsch, B. Baufeld, S. Dalkilic, L. Chernova, and M. Heinzelmann. Fatigue cracks in a thermal barrier coating system on a superalloy in multiaxial thermo-mechanical testing. *International Journal of Fatigue*, 30:211218, 2008.

[7] M. Bartsch, M. Günter, M. K., and C. Sick. Fatigue testing of ceramic thermal barrier coatings for gas turbine blades. *Advanced Engineering Materials*, 1:127129, 1999.

[8] B. Baufeld, M. Bartsch, S. Dalkili, and M. Heinzelmann. Defect evolution in thermal barrier coating systems under multi-axial thermomechanical loading. *Surface & Coatings Technology*, 200:1282–1286, 2005.

[9] W. Beele, G. Marijnissen, and A. van Lieshout. The evolution of thermal barrier coatings status and upcoming solutions for today's key issues. *Surface and Coatings Technology*, 120121(0):61 – 67, 1999.

[10] H. Bhatnagar, S. Ghosh, and M. E. Walter. A parametric study of damage initiation and propagation in EB-PVD thermal barrier coatings. *Mechanics of Materials*, 42(1):96 – 107, 2010.

[11] S. Bose and J. DeMasi-Marcin. Thermal barrier coating experience in gas turbine engines at pratt & whitney. *Journal of Thermal Spray Technology*, 6(1):99–104, 1997.

[12] W. Brindley and J. Whittenberger. Stress relaxation of low pressure plasma-sprayed NiCrAlY alloys. *Materials Science and Engineering: A*, 163(1):33 – 41, 1993.

[13] E. Busso, H. Evans, Z. Qian, and M. Taylor. Effects of breakaway oxidation on local stresses in thermal barrier coatings. *Acta Materialia*, 58(4):1242 – 1251, 2010.

[14] S. R. Choi, J. W. Hutchinson, and A. Evans. Delamination of multilayer thermal barrier coatings. *Mechanics of materials*, 31(7):431–447, 1999.

[15] R. Christensen, D. Lipkin, and D. Clarke. Nondestructive evaluation of the oxidation stresses through thermal barrier coatings using Cr^{3+} piezospectroscopy. *Applied Physics Letters*, 69:3754–3756, 1996.

[16] D. Clarke. The lateral growth strain accompanying the formation of a thermally grown oxide. *Acta Materialia*, 51(5):1393 – 1407, 2003.

[17] D. R. Clarke, M. Oechsner, and N. P. Padture. Thermal-barrier coatings for more efficient gas-turbine engines. *MRS Bulletin*, 37:891–898, 10 2012.

[18] C. o. E. Committee on Coatings for High-Temperature Structural Materials and N. R. C. Technical Systems. *Coatings for High-Temperature Structural Materials:Trends and Opportunities*. The National Academies Press, 1996.

[19] H. Davies. The design and development of the Thiokol XRL99 rocket engine for the X-15 aircraft. *Journal of the Royal Aeronautical Society*, 67:79–91, 1963.

[20] R. Diaz, M. Jansz, M. Mossaddad, S. Raghavan, J. Okasinski, J. Almer, H. Pelaez-Perez, and P. Imbrie. Role of mechanical loads in inducing in-cycle tensile stress in thermally grown oxide. *Applied Physics Letters*, 100:111906, 2012.

[21] J. M. Drexler, A. Aygun, D. Li, R. Vaßen, T. Steinke, and N. P. Padture. Thermal-gradient testing of thermal barrier coatings under simultaneous attack by molten glassy deposits and its mitigation. *Surface and Coatings Technology*, 204:2683–2688, 2010.

[22] C. Eberl, X. Wang, D. S. Gianola, J. T. D. Nguyen, M. Y. He, A. G. Evans, and K. J. Hemkerz. In situ measurement of the toughness of the interface between a thermal barrier coating and a Ni alloy. *The American Ceramic Society*, 94 [S1]:S120S127, 2011.

[23] J. Eldridge, T. Bencic, S. Allison, and D. Beshears. Depth-penetrating temperature measurements of thermal barrier coatings incorporating thermographic phosphors. *Journal of Thermal Spray Technology*, 13(1):44–50, 2004.

[24] A. Evans, M. He., and J. Hutchinson. Mechanics-based scaling laws for the durability of thermal barrier coatings. *Progress in Materials Science*, 46:249–271, 2001.

[25] A. Evans, D. Mumm, J. Hutchinson, G. Meier, and F. Pettit. Mechanisms controlling the durability of thermal barrier coatings. *Progress in Materials Science*, 46:505–553, 2001.

[26] H. Evans, A. Strawbridge, R. Carolan, and C. Ponton. Creep effects on the spallation of an alumina layer from a NiCrAlY coating. *Materials Science and Engineering: A - Structural Materials, Properties, Microstructure and Processing*, 225(1-2):1 – 8, n.d.

[27] J. P. Feist, A. L. Heyes, and J. R. Nicholls. Phosphor thermometry in an electron beam physical vapour deposition produced thermal barrier coating doped with dysprosium. *Proceedings of the Institution of Mechanical Engineers, Part G: Journal of Aerospace Engineering*, 215(6):333–341, 2001.

[28] J. D. French, J. Zhao, M. P. Harmer, H. M. Chan, and G. A. Miller. Creep of duplex microstructures. *American Ceramic Society*, 77-11:2857–2865, 1994.

[29] F. G. Garrett and C. A. Gyorgak. Adhesive and protective characteristic of ceramic coating A-417 and its effects on engine life of forged refractory-26 (AMS 5760) and cast satellite (AMS 5385) turbine blades. Technical report, National Advisory Committee for Aeronautics, 1953.

[30] M. Gell, J. Eric, V. Krishnakumar, K. McCarron, B. Barber, Y.-H. Sohn, and V. K. Tolpygo. Bond strength, bond stress and spallation mechanisms of thermal barrier coatings. *Surface and Coatings Technology*, 120:53–60, 1999.

[31] M. Gell, K. Vaidyanathan, B. Barber, E. Jordan, and J. Cheng. Mechanism of spallation in platinum aluminide/electron beam physical vapor-deposited thermal barrier coatings. *Metallurgical and Materials Transactions A*, 30(2):427–435, 1999.

[32] M. M. Gentleman, V. Lughi, J. A. Nychka, and D. R. Clarke. Non-contact methods for measuring thermal barrier coating temperatures. *International Journal of Applied Ceramic Technology*, 3:105–112, 2006.

[33] X.-Y. Gong and D. Clarke. On the measurement of strain in coatings formed on a wrinkled elastic substrate. *Oxidation of metals*, 50(5-6):355–376, 1998.

[34] W. Harrison, D. Moore, J. Richmond, and U. S. N. A. C. for Aeronautics. *Review of an Investigation of Ceramic Coatings for Metallic Turbine Parts and Other High-temperature Applications*. Technical note - National Advisory Committee for Aeronautics. National Advisory Committee for Aeronautics, 1947.

[35] V. Hauk. *Structural and Residual Stress Analysis by Nondestructive Methods: Evaluation - Application - Assessment*. Elsevier Science, 1997.

[36] B. He and K. L. Smith. Fundamental equation of strain and stress measurement using 2D detectors. In *Proceedings of the SEM Spring Conference on Experimental Mechanics*, pages 217–220. SEM Society for Experimental Mechanics Inc., 1998.

[37] M. He, A. Evans, and J. Hutchinson. The ratcheting of compressed thermally grown thin films on ductile substrates. *Acta Materialia*, 48(10):2593 – 2601, 2000.

[38] L. N. Hjelm and B. R. Bornhorst. Research-airplane-committee report on conference on the progress of the X-15 project. In *NASA TM X-57072*, pages 227–253. National Aeronautics and Space Administration, 1961.

[39] P. Hou, A. Paulikas, and B. Veal. Growth strains in thermally grown Al_2O_3 scales studied using synchrotron radiation. *Journal of the Minerals, Metals and Materials Society*, 61:51, 2009.

[40] J. Hutchinson and A. Evans. On the delamination of thermal barrier coatings in a thermal gradient. *Surface and Coatings Technology*, 149(2):179–184, 2002.

[41] A. M. Karlsson and A. G. Evans. A numerical model for the cyclic instability of thermally grown oxides in thermal barrier systems. *Acta Materialia*, Volume 49 Issue 10:1793–1804, 2001.

[42] A. M. Karlsson, J. W. Hutchinson, and A. G. Evans. A fundamental model of cyclic instabilities in thermal barrier systems. *Journal of the Mechanics and Physics of Solids*, 50:1565–1589, 2002.

[43] A. M. Karlsson, J. W. Hutchinson, and A. G. Evans. The displacement of the thermally grown oxide in thermal barrier systems upon temperature cycling. *Materials Science and Engineering A*, Volume 351 Issues 1-2:244–257, 2003.

[44] R. Kitazawa, M. Tanaka, Y. Kagawa, and Y. Liu. Damage evolution of TBC system under in-phase thermo-mechanical tests. *Materials Science and Engineering: B*, 173:130134, 2010.

[45] S. Laxman, B. Franke, B. Kempshall, Y. Sohn, L. Giannuzzi, and K. Murphy. Phase transformations of thermally grown oxide on (Ni,Pt)Al bondcoat during electron beam physical vapor deposition and subsequent oxidation. *Surface and Coatings Technology*, 177178(0):121 – 130, 2004. Proceedings of the 30th International Conference on Metallurgical Coatings and Thin Films.

[46] J. H. Lee, C. C. Aydner, J. Almer, J. Bernier, K. W. Chapman, P. J. Chupas, D. Haeffner, K. Kump, P. L. Lee, U. Lienert, A. Miceli, and G. Vera. Synchrotron applications of an amorphous silicon flat-panel detector. *Journal of Synchrotron Radiation*, 15(5):477–488, 2008.

[47] C. G. Levi, J. Y. Yang, B. J. Dalgleish, F. W. Zok, and A. G. Evans. Processing and performance of an all-oxide ceramic composite. *Journal of the American Ceramic Society*, 81(8):2077–2086, 1998.

[48] A. M. Limarga, R. Vaßen, and D. R. Clarke. Stress distributions in plasma-sprayed thermal barrier coatings under thermal cycling in a temperature gradient. *Journal of Applied Mechanics*, 78:011003, 2011.

[49] D. Lipkin and D. Clarke. Measurement of the stress in oxide scales formed by oxidation of alumina-forming alloys. *Oxidation of Metals*, 45(3-4):267–280, 1996.

[50] A. Maricocchi, A. Bartz, and D. Wortman. PVD TBC experience on GE aircraft engines. *Journal of Thermal Spray Technology*, 6(2):193–198, 1997.

[51] J. Markham and K. Kinsella. Thermal radiative properties and temperature measurement from turbine coatings. *International Journal of Thermophysics*, 19(2):537–545, 1998.

[52] V. Maurel, A. Koster, and L. Rémy. An analysis of thermal gradient impact in thermal-mechanical fatigue testing. *Fatigue & Fracture of Engineering Materials & Structures*, 33:473–489, 2010.

[53] C. Mercer, K. Kawagishi, T. Tomimatsu, D. Hovis, and T. Pollock. A comparative investigation of oxide formation on EQ (Equilibrium) and NiCoCrAlY bond coats under stepped thermal cycling. *Surface and Coatings Technology*, 205(8):3066–3072, 2011.

[54] R. Miller. Thermal barrier coatings for aircraft engines: history and directions. *Journal of Thermal Spray Technology*, 6(1):35–42, 1997.

[55] R. A. Miller and C. E. Lowell. Failure mechanisms of thermal barrier coatings exposed to elevated temperatures. *Thin Solid Films*, 95(3):265 – 273, 1982.

[56] R. A. Milller. Oxidation-based model for thermal barrier coating life. *Journal of the American Ceramic Society*, 67(8):517–521, 1984.

[57] D. Mumm, A. Evans, and I. Spitsberg. Characterization of a cyclic displacement instability for a thermally grown oxide in a thermal barrier system. *Acta Materialia*, 49(12):2329 – 2340, 2001.

[58] I. Noyan and J. Cohen. *Residual stress: measurement by diffraction and interpretation.* Materials research and engineering. Springer, 1987.

[59] N. P. Padture, M. Gell, and E. H. Jordan. Thermal barrier coatings for gas-turbine engine applications. *Science*, 296:280–284, 2002.

[60] D. Pan, M. Chen, P. Wright, and K. Hemker. Evolution of a diffusion aluminide bond coat for thermal barrier coatings during thermal cycling. *Acta Materialia*, 51:2205–2217, 2003.

[61] J. Park, U. Lienert, P. Dawson, and M. Miller. Quantifying three-dimensional residual stress distributions using spatially-resolved diffraction measurements and finite element based data reduction. *Experimental Mechanics*, 53(9):1491–1507, 2013.

[62] C. Pilgrim, S. Berthier, J. Feist, R. Wellman, and A. Heyes. Photoluminescence for quantitative non-destructive evaluation of thermal barrier coating erosion. *Surface and Coatings Technology*, 209(0):44 – 51, 2012.

[63] T. Pollock, D. Lipkin, and K. Hemker. Multifunctional coating interlayers for thermal-barrier systems. *MRS Bulletin*, 37:923–931, 10 2012.

[64] A. Reddy, D. Hovis, A. Heuer, A. Paulikas, and B. Veal. In situ study of oxidation-induced growth strains in a model NiCrAlY bond-coat alloy. *Oxidation of Metals*, 67(3-4):153–177, 2007.

[65] J. Rösler, M. Bäker, and K. Aufzug. A parametric study of the stress state of thermal barrier coatings: Part i: creep relaxation. *Acta Materialia*, 52(16):4809 – 4817, 2004.

[66] J. Rösler, M. Bäker, and M. Volgmann. Stress state and failure mechanisms of thermal barrier coatings: Role of creep in thermally grown oxide. *Acta Materialia*, 49:3659–3670, 2001.

[67] K. Schlichting, N. P. andE. H. Jordan, and M. Gell. Failure modes in plasma-sprayed thermal barrier coatings. *Materials Science and Engineering A*, 342:120–130, 2003.

[68] K. W. Schlichting, K. Vaidyanathan, Y. H. Sohn, E. H. Jordan, M. Gell, and N. P. Padture. Application of Cr^{3+} photoluminescence piezo-spectroscopy to plasma-sprayed thermal barrier coatings for residual stress measurement. *Materials Science and Engineering A*, 291(1-2):68 – 77, 2000.

[69] U. Schulz, C. Leyens, K. Fritscher, M. Peters, B. Saruhan-Brings, O. Lavigne, J.-M. Dorvaux, M. Poulain, R. Mvrel, and M. Caliez. Some recent trends in research and technology of advanced thermal barrier coatings. *Aerospace Science and Technology*, 7:73–80, 2003.

[70] J. Schwarzer, D. Löhe, and O. Vöhringer. Influence of the TGO creep behavior on delamination stress development in thermal barrier coating systems. *Materials Science and Engineering A*, 387-389:692–695, 2004.

[71] V. Sergo and D. R. Clarke. Observation of subcritical spall propagation of a thermal barrier coating. *Journal of the American Ceramic Society*, 81(12):3237–3242, 1998.

[72] S. D. Shastri, J. Almer, C. Ribbing, and B. Cederström. High-energy X-ray optics with silicon saw-tooth refractive lenses. *Journal of Synchrotron Radiation*, 14(2):204–211, Mar 2007.

[73] S. D. Shastri, R. J. Dejus, and D. R. Haeffner. Experimental Characterization of APS Undulator A at High Photon Energies (50–200 keV). *Journal of Synchrotron Radiation*, 5(2):67–71, Mar 1998.

[74] E. Shillington and D. Clarke. Spalling failure of a thermal barrier coating associated with aluminum depletion in the bond-coat. *Acta Materialia*, 47(4):1297 – 1305, 1999.

[75] S. F. Siddiqui, K. Knipe, A. Manero, C. Meid, J. Wischek, J. Okasinski, J. Almer, A. M. Karlsson, M. Bartsch, and S. Raghavan. Synchrotron x-ray measurement techniques for thermal barrier coated cylindrical samples under thermal gradients. *Review of Scientific Instruments*, 84(8):083904–083904, 2013.

[76] G. Simmons. Single crystal elastic constants and calculated aggregate properties. Technical report, DTIC Document, 1965.

[77] Y. Sohn, J. Kim, E. Jordan, and M. Gell. Thermal cycling of EB-PVD/MCrAlY thermal barrier coatings: I. Microstructural development and spallation mechanisms. *Surface and Coatings Technology*, 146147(0):70 – 78, 2001. Proceedings of the 28th International Conference on Metallurgic Coatings and Thin Films.

[78] I. Spitsberg, D. Mumm, and A. Evans. On the failure mechanisms of thermal barrier coatings with diffusion aluminide bond coatings. *Materials Science and Engineering: A*, 394(12):176 – 191, 2005.

[79] S. Sridharan, L. Xie, E. H. Jordan, and M. Gell. Stress variation with thermal cycling in the thermally grown oxide of an EB-PVD thermal barrier coating. *Surface Coatings and Technology*, 179:286–296, 2004.

[80] S. Stecura. Two layer thermal barrier coating for high temperature components. *American Ceramic Society Bulletin*, 56:1082–1085, 1977.

[81] S. Stecura. Effects of compositional changes on the performance of a thermal barrier coating system. *NASA Technical Memorandum*, NASA TM-78976, 1978.

[82] M. Stiger, N. Yanar, M. Topping, F. Pettit, and G. Meier. Thermal barrier coatings for the 21st century. *Zeitschrift fur Metallkunde*, 90(12):1069–1078, 1999.

[83] H. Suzuki, K. Akita, Y. Yoshioka, Y. Waku, and H. Misawa. Evaluation of phase stresses of Al_2O_3/YAG binary mgc by synchrotron radiation–residual stress states and stress behavior of YAG phase. *Journal of the Society of Materials Science, Japan*, 52(7):770–775, 2003.

[84] K. Suzuki and T. Shobu. Internal stress in EB-PVD thermal barrier coating under heat cycle. *Material Science Forums*, 638-642:906–911, 2010.

[85] J. Thompson, T. Tsui, R. Reed, and R.-R. plc. *Creep of Plasma Sprayed CoNi-CrAlY and NiCrAlY Bond Coats and Its Effects on Residual Stresses During Thermal Cycling of Thermal Barrier Coating Systems*. Rolls Royce reprint. Rolls-Royce plc, 1998.

[86] J. Thornton, S. Slater, and J. Almer. The measurement of residual strains within thermal barrier coatings using high-energy x-ray diffraction. *Journal of the American Ceramic Society*, 88:2817–2825, 2005.

[87] V. Tolpygo and D. Clarke. Wrinkling of α-Al_2O_3 films grown by thermal oxidation-I. quantitative studies on single crystals of Fe–Cr–Al alloy. *Acta materialia*, 46(14):5153–5166, 1998.

[88] V. Tolpygo, J. Dryden, and D. Clarke. Determination of the growth stress and strain in α-Al_2O_3 scales during the oxidation of Fe-22Cr-4.8 Al-0.3 Y alloy. *Acta Materialia*, 46(3):927–937, 1998.

[89] G. Totten. *Handbook of Residual Stress and Deformation of Steel*. ASM International, 2002.

[90] S. Tsipas, I. Golosnoy, T. Clyne, and R. Damani. The effect of a high thermal gradient on sintering and stiffening in the top coat of a thermal barrier coating system. *Journal of Thermal Spray Technology*, 13(3):370–376, 2004.

[91] E. Tzimas, H. Müllejans, S. Peteves, J. Bressers, and W. Stamm. Failure of thermal barrier coating systems under cyclic thermomechanical loading. *Acta materialia*, 48(18):4699–4707, 2000.

[92] K. Vaidyanathan, M. Gell, and E. Jordan. Mechanisms of spallation of electron beam physical vapor deposited thermal barrier coatings with and without platinum aluminide bond coat ridges. *Surface and Coatings Technology*, 133134(0):28 – 34, 2000.

[93] R. Vaßen, Y. Kagawa, R. Subramanian, P. Zombo, and D. Zhu. Testing and evaluation of thermal-barrier coatings. *MRS Bulletin*, 37:911–916, 10 2012.

[94] B. W. Veal, A. P. Paulikas, and P. Y. Hou. Tensile stress and creep in thermally grown oxide. *Nature Materials*, 5:349–351, May 2006.

[95] X. Wang, R. Wu, and A. Atkinson. Characterisation of residual stress and interface degradation in TBCs by photo-luminescence piezo-spectroscopy. *Surface and Coatings Technology*, 204(15):2472 – 2482, 2010.

[96] M. Wen, E. H. Jordan, and M. Gell. Analysis of localized damage in EB-PVD/(Ni, Pt) al thermal barrier coatings. *Surface and Coatings Technology*, 200(18):5193–5202, 2006.

[97] M. Wen, E. H. Jordan, and M. Gell. Effect of temperature on rumpling and thermally grown oxide stress in an EB-PVD thermal barrier coating. *Surface and Coatings Technology*, 201(6):3289 – 3298, 2006.

[98] P. K. Wright and A. G. Evans. Mechanisms governing the performance of thermal barrier coatings. *Current Opinion in Solid State and Materials Science*, 4:255–265, 1999.

[99] Y. Zhou and T. Hashida. Coupled effects of temperature gradient and oxidation on thermal stress in thermal barrier coating system. *International journal of solids and structures*, 38(24):4235–4264, 2001.

[100] D. Zhu and R. Miller. Thermal conductivity and elastic modulus evolution of thermal barrier coatings under high heat flux conditions. *Journal of Thermal Spray Technology*, 9(2):175–180, 2000.